

Transmission Electron Microscopy Study on Oxidation
and Microstructures of Single Crystal Silicon Carbide

Bralee Chayasombat

Contents

1. Introduction.....	1
1.1 Historical Aspect	
1.2 Characters and Properties of Silicon Carbide	
1.2.1 Structure of Silicon Carbide	
1.2.2 Crystal Growth of Silicon Carbide	
1.2.3 Electronic Properties of Silicon Carbide	
1.2.4 Defects in Silicon Carbide	
1.2.5 Oxidation of Silicon Carbide	
1.3 Background and Objectives	
References	
2. Experimental Instruments and Procedures.....	17
2.1 Focused Ion Beam (FIB)	
2.1.1 Micro-sampling Technique	
2.1.2 FIB-SEM Dual System	
2.2 Transmission Electron Microscopy (TEM)	
2.2.1 Outline of TEM	
2.2.2 Contrast Experiment	
References	
3. Oxidation Kinetics of Silicon Carbide.....	30
3.1 Introduction	
3.2 Previous Studies on Oxidation Kinetics of Silicon Carbide	
3.3 Background and Objective	
3.4 Experimental Procedures	
3.5 Results and Discussion	

3.5.1 Model for Oxidation Kinetics	
3.5.2 Oxidation Rates of the Si-face and the C-face	
3.5.3 Oxidation Activation Energies of the Si-face and the C-face	
3.6 Summary	
References	

4. Microstructures of Oxide Scales on Silicon Carbide.....50

4.1 Introduction	
4.2 Previous Studies on Microstructures of Oxide Scales on Silicon Carbide	
4.3 Background and Objective	
4.4 Experimental Procedures	
4.5 Results	
4.5.1 Oxidation in Dry Oxygen	
4.5.2 Oxidation of Samples with High Surface Roughness	
4.5.3 Oxidation in Air	
4.6 Discussion	
4.7 Summary	
References	

5. Microstructures and Defects in Cubic Silicon Carbide.....78

5.1 Introduction	
5.2 Background and Objective	
5.3 Experimental Procedures	
5.3.1 3C-SiC Sample: CVD method and SBE method	
5.3.2 TEM Specimen Preparation by FIB Microsampling	
5.4 Results and Discussion	
5.4.1 Defects in CVD 3C-SiC	
5.4.2 Defects in SBE 3C-SiC	

5.4.3 Ion Implantation in SBE 3C-SiC

5.5 Summary

References

6. Summary.....	96
Acknowledgement.....	100
List of Publications.....	101

Chapter 1: Introduction

1.1 Historical Aspect

Silicon carbide (SiC) was first recognized by Berzelius in 1824¹. Natural SiC is extremely rare on earth but quite common in space in form of stardust. Most existing SiC found on earth is in the form of synthesis SiC. The first systematic synthesis method for SiC was developed by Acheson around 1892². The Acheson process used silica or quartz sand and carbon material as substrate materials which were then reacted at high temperature (approximately 2000K- 2800K) to form coarse crystalline SiC. Most of the product formed by the Acheson process is α -SiC. Later in 1955, Lely improved the synthesis process for producing SiC called Lely process³. The crystalline quality of SiC produced by the Lely process is quite high. However, it has no polytypic control, and the SiC produced by Lely process has irregular sizes and the process has very low yield. Approximately 20 years later, Tairov and Tsvetkov developed a process called the modified Lely process⁴. This process produces a considerable lower crystalline quality compared to the Lely process. However, it had overcome the problems with low yield and irregular sizes, and with the temperature control and orientation of the seed crystal, different polytypic can be produced.

At first, SiC was mainly used as abrasive material for cutting and polishing because of its extremely hard characteristic which was recognized soon after it was discovered (about 9.5 on the Mohs scale). Later on, it was also used as high temperature ceramics because of its high thermal stability (up to about 2300K) and as electrical device material in the 20th century. Nowadays, many researches are being conducted on SiC to be used as a power device material, in hope for replacing the currently commonly used silicon base device material. The change of the device material for electrical appliances from silicon to SiC, i.e. the change into higher power system, is hoped to lead to cheaper, higher efficiency and better electronics system.

1.2 Characters and Properties of Silicon Carbide

1.2.1 Structure of Silicon Carbide

SiC have various polymorphs. At least 70 crystalline forms of SiC are proven to be existed⁵. These various forms of SiC originated from one type of primitive unit cell. The primitive unit cell of SiC is a tetrahedral made from a carbon atom with the 4 nearest silicon atoms, as shown in Fig.1-1. For all polymorphs, the distance between neighbor silicon or carbon atom is approximately 0.308 nm, and the distance between the nearest neighbor of silicon and carbon atom is approximately 0.189 nm. These primitive unit cells are grouped together forming hexagonal frames. These frames will form closely packed silicon-carbon bi-layers. Fig.1-2 shows top view of 3 types of hexagonal close-packed sites. If the first double layer is positioned at A, the next layer that can be placed at B or C according to a closed packed structure. The differences between the polymorphs came from the different stacking order, A, B and C, between succeeding double layers of carbon and silicon atoms of these hexagonal frames.

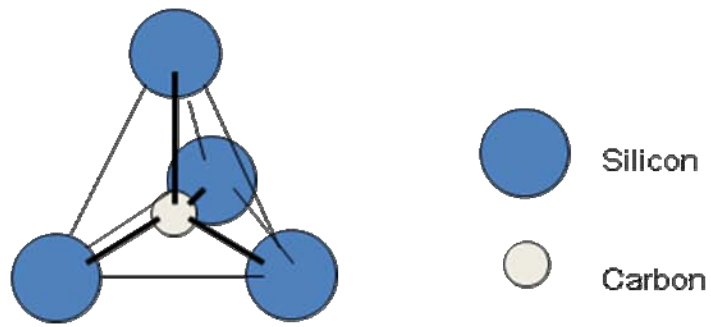


Figure 1-1 : The tetrahedral primitive unit cell of silicon carbide

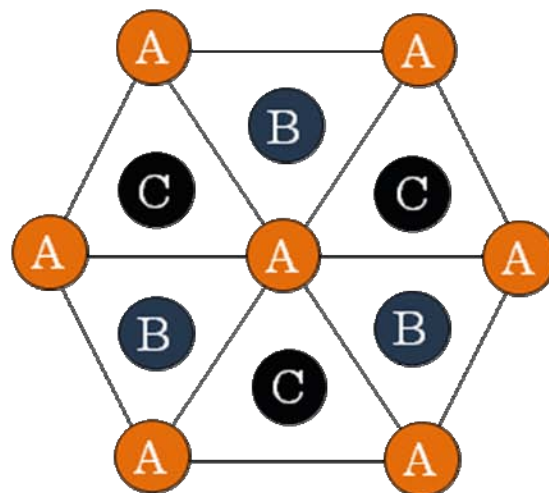


Figure 1-2 : Top view of 3 types of hexagonal close-packed sites.

The polymorphs of SiC are marked according to Ramsdell notation. The alphabets represent the resulting structures of the crystal; H is for hexagonal, R is for rhombohedral and C is for cubic. The numbers represent periodic of the stacking sequences. For example, 4H-SiC has a hexagonal structure and its stacking sequence is ABACABAC... While the structure of 3C-SiC is cubic, with stacking sequence of ABCABC... Fig.1-3 shows schematics of the atomic structure of 3C, 4H, and 6H-SiC. These differences in stacking sequences, in other words, different polymorphs, would differ all physical, electronic and optical properties of the SiC. Table 1-1 shows comparison of properties between 4H, 6H and 3C-SiC^{6, 7, 8, 9, 10}. It can be seen from the Table 1-1 that, the properties of each polymorph are different, especially in the electrical properties.

Moreover, resulting from the arrangement of the primitive tetrahedral unit cells, as mentioned earlier, it will form closely packed silicon-carbon bi-layer. This means that, in case of single crystal, along the [0001] axis in case of hexagonal SiC and [111] axis in case of cubic SiC, one side of the crystal is composed of only silicon atoms, and the other side of the crystal of only carbon atoms. The former is called Si-terminated face and the latter is called C-terminated face. The physical and electric properties of the crystal also differ between the Si-terminated face and the C-terminated face.

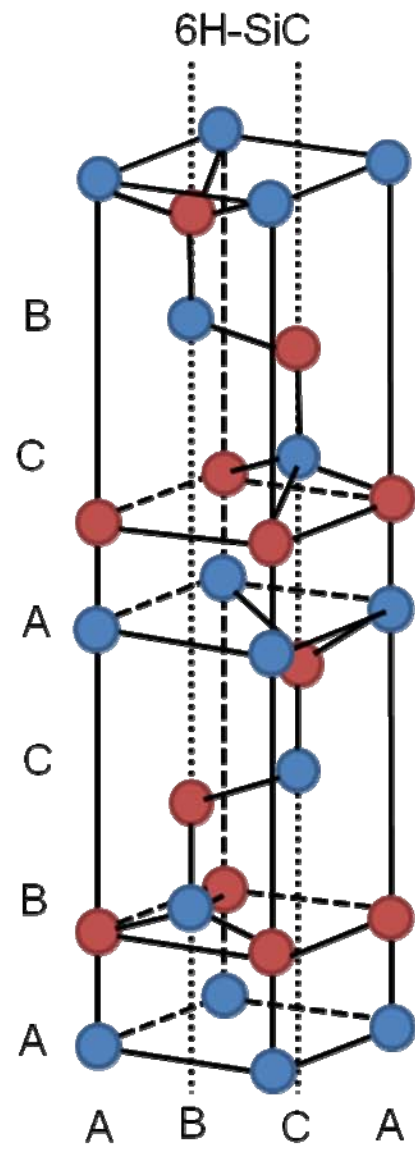
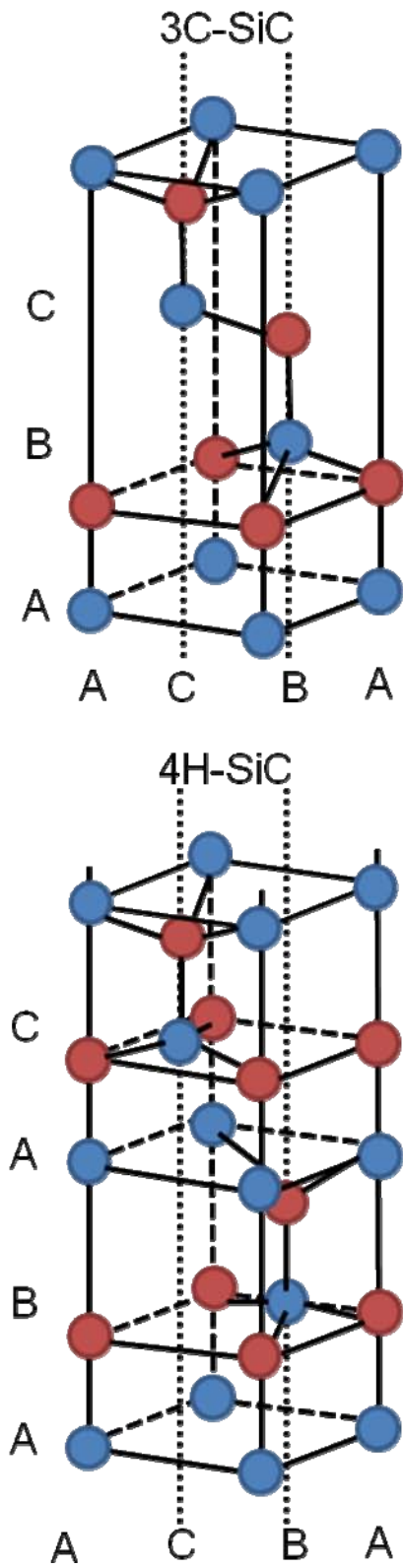


Figure 1-3 : Schematics of atomic structures of 3C-SiC, 4H-SiC and 6H-SiC.

Table 1-1 : Comparison of properties on each polytypes of SiC.

	3C-SiC	4H-SiC	6H-SiC	Reference
Crystal structure	Zinc blende (cubic)	Wurtzite (Hexagonal)	Wurtzite (Hexagonal)	
Bulk modulus (at 300K)	$2.5 \times 10^{12} \text{dyncm}^{-2}$	$2.2 \times 10^{12} \text{dyncm}^{-2}$	$2.2 \times 10^{12} \text{dyncm}^{-2}$	[15]
Debye temperature	1200 K	1300 K	1200 K	[15]
Sublimation temperature	3103 +/- 40 K	3103 +/- 40 K	3103 +/- 40 K	[16], [17]
Density	3.21 g/cm ³	3.211 g/cm ³	3.21 g/cm ³	[18], [19]
Band gap	2.4 eV	3.26 eV	3.04 eV	
Breakdown voltage	600 V	1000 V	1000 V	[20]
Breakdown field strength	2 MV/cm	3 MV/cm	3 MV/cm	
Thermal conductivity	5 W/cm/K	5 W/cm/K	5 W/cm/K	
Electron mobility	800 cm ² /V/s	1000 cm ² /V/s	400 cm ² /V/s	
Saturated drift velocity	$2.20 \times 10^7 \text{ cm/s}$	$2.39 \times 10^7 \text{ cm/s}$	$2.31 \times 10^7 \text{ cm/s}$	

1.2.2 Crystal Growth of Silicon Carbide

Commonly, the used bulk growth processes of SiC are Acheson process, Lely process, the modified Lely process and epitaxial growth. As mention earlier, the Acheson process is the process that heats a mixture of silica (mostly in form of quartz sand), carbon material (in form of petroleum coke), sawdust and common salt. The saw dust was added in the mixture in order to make the mixture porous so that the carbon monoxide produced in the reaction can escape, and salt acted as purifier. All materials were heated up to approximately 3000K in an electric arc furnace¹¹. The SiC produced by this method is mostly in form of sintered small crystallites. The simplicity of the process makes it appropriate for production of huge quantities of SiC which is suitable for grinding and cutting purposes. However, the SiC produced by the Acheson process may not have proper quality for using as electronic devices.

As SiC getting more attention as electrical devices material, it is important that a large quantity of large single crystal SiC must be produced. The Lely process was developed in 1955 by Lely¹². This process uses physical vapor transport (PVT) technique for crystal growth. In this technique, a solid source of SiC is evaporated at about 2800K and the vapors would crystallize at the colder part of the furnace. As stated earlier, this process has some inferior points, such as low yield of the process or the irregular sizes. However, The SiC produced by the Lely process can have a very high crystal quality. The high quality of the Lely grown SiC makes it usable as substrates for an epitaxial growth.

The modified Lely process also uses PVT technique as a technique for crystal growth. It is a seeded sublimation growth process¹³. It solved low yield and irregular sizes problems occurred in the Lely process. Also, it was reported that different growth temperatures and the orientation of the seed crystal give rise to different polytypes¹⁴. This means that the polytypic formation can be controlled at some level, while the Lely process possesses no control over the polytypic formation at all. However, the quality of

crystalline is worse, compared to the crystal formed by the Lely process, by the formation of diameter approximately 0.1 - 5 μm holes of micro pipes. The cause of the formation of micro pipes was believed to be the grouping of several screw dislocations¹⁵. However there are arguments against this and currently is not fully understood. Another problem in crystalline grown by modified Lely process is the mosaic structure of the substrates¹⁶.

The epitaxial growth is a process that atoms are placed on top of a substrate orderly. The purpose of epitaxy is to create thin high quality layers of different composition. There are many techniques in epitaxial growth. The most widely and commonly used techniques is chemical vapor deposition (CVD). The principle of the CVD process is by using a carrier gas, reactive compounds are transported to a hot zone. At the hot zone, the reactive compounds will thermally decompose into atoms or radicals of two or more atoms which may diffuse down onto a substrate and produce an epitaxial film. In this technique, the polymorphs can be controlled by altering the temperatures and substrates on which the epitaxial layers were grown on. For example, the growth on silicon substrate, the epitaxy layers are always formed as 3C-SiC polymorph¹⁷.

1.2.3 Electronic Properties of Silicon Carbide

The comparison of physical and electronic properties of SiC and other semiconductor materials is shown in Table 1-2¹⁸. It can be seen from the table that, SiC's band gap is wider than that of silicon. In addition, compare to silicon, SiC has high thermal conductivity. Moreover, in the case of 6H-SiC, the breakdown electric field strength is one order of magnitude higher than Si and the saturated drift velocity of the electrons is even higher than that of GaAs. We can conclude that, comparing to others commonly known semiconductor materials, the electrical properties of SiC are only inferior to those of diamond. But in case of using diamond as semiconductor material, it is known that the level of the dopants is much deeper than SiC, thus the diamond devices are very inefficient when using at room temperature. And there is also problem in growing

diamond crystal. As long as there are no suitable substrates for epitaxial growth of diamond, SiC is expected to be the most suitable material for electronic devices.

The comparison of properties on each polymorphs of SiC is shown in Table 1-1. As shown in Table 1-1, the band gaps, the breakdown voltages and the electron mobility of hexagonal SiC, 4H and 6H, are higher than those of 3C-SiC. However, for SiC growth technique at present, micro pipes are known to be inevitable in the growth of hexagonal SiC crystal. These pipes are not found in cubic SiC.

Besides its outstanding electrical properties, as mention in above, SiC can be thermally oxidized to form the insulating and high quality oxide scales which can be efficiently used as a part or parts in the semiconductor devices. Hence, SiC has attracted a great deal of attention to replace silicon as a high frequency, high efficiency and high temperature semiconductor device material.

Table 1-2 : Comparison of properties on SiC (3C and 6H) and others semiconductors materials.

Property	Si	GaAs	GaN (Wurtzite)	GaP	3C-SiC [6H-SiC]	Diamond
Band Gap at 300K. (eV)	1.1	1.4	3.4	2.3	2.2 [2.9]	5.5
Maximum Operating Temperature. (°C)	300	460	400	925	873 [1240]	1100{?}
Melting Point. (°C)	1320	1238	2500	1470	Sublimes > 1800	Phase Change
Physical Stability	Good	Fair	Very Good	Fair	Excellent	Very Good
Electron Mobility at 300K. (cm ² /V-s)	1400	8500	440	350	1000 [600]	2200
Hole Mobility at 300K. (cm ² /V-s)	1.1	400	350	100	40	1500
Breakdown Field. (MV/cm)	0.3	0.4	5	-	4 [2.5]	10
Thermal Conductivity. (W/cm-°C)	1.5	0.5	1.3	0.8	5	20
Sat. Elec. Drift Velocity. (10 ⁷ cm/s)	1	2	0.88	-	2.5 [2.0]	2.7
Dielectric Constant. (K)	11.8	12.8	9.7	11.1	9.7	5.5
Relative Z _j	1	7	324	-	1100 [252]	2601

Z_j: Johnson Figure of Merit (transistor power and frequency performance)

1.2.4 Defects in Silicon Carbide

Defects in SiC need to be considered seriously especially when using SiC for electrical device materials. The defects affect the physical properties of SiC as well as electrical properties²⁰. SiC based power devices are reported to be degraded by existence of defects¹⁹. Defects can be appearing during the growth of SiC, or during process carried out later, such as annealing or thermal oxidation. Common defects often found in SiC can be categorized in 5 categories: point defects, linear defects, planar defects, volume defects and mixed defects²⁰.

Point defects such as vacancies or interstitials originated from silicon or carbon atoms, either in form of single atoms or small clusters, in the SiC lattice are misplaced. This could happen in bulk growth process. Or it can be induced by doping of the SiC with atoms such as nitrogen, phosphorus or aluminum for electrical purposes.

Linear defects or dislocations are a lattice imperfection that propagated only in one dimension. Most commonly found dislocations in SiC are threading screw dislocations, threading edge dislocations and basal plane dislocations. The first two dislocations, if parallel to the c-axis of the substrate, can penetrate through the whole wafer and epitaxial layers.

Planar defects found in SiC are, stacking faults, low angle boundaries, twins, and inversion domain boundaries. These defects mostly occurred during the crystal growth, either by PVT process or CVD process. Stacking faults formation is easily activated where basal plane dislocations are. However, it is believed that stacking faults can be reduced by appropriate surface preparation condition²¹.

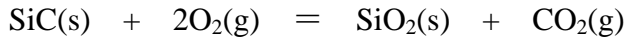
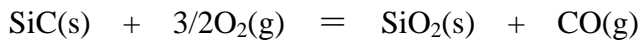
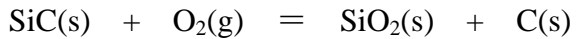
Volume defects or polytypic inclusions are originated from the phase transformation during the growth procedure due to growth condition.

Mixed defects or micropipes, the screw dislocations with hollow core, are one of the most commonly found defects in SiC. These screw dislocations only terminated at crystal surfaces and therefore reproduced during epitaxial growth of the SiC substrate. High density of micropipes will cause a loss of yield in the device manufacturing process.

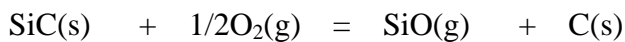
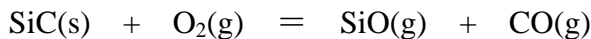
1.2.5 Oxidation of Silicon Carbide

SiC is a chemically stable substance, and has a very high oxidation resistance compared with that of silicon. The structures and crystallizations of product oxide scales depend highly on the oxidation temperatures.

In high oxygen partial pressure environment, the oxidation reactions occur as below²²



The oxide products are silica (SiO₂). These oxide scales are dense. They cover over the SiC surfaces and become oxidation-resistant films, so further oxidation is prevented. This is called passive oxidation. The passive oxidation will lead to weight gain in the samples after oxidation. On the other hand, in low oxygen partial pressure environment, different reaction occurs, as shown below.



The solid silica scales are not formed. Instead, the product oxide of this reaction is gaseous SiO which vaporized during the process of oxidation. Weight loss can be observed in this active oxidation. Formations of graphite or Carbon nanotubes caused by decomposition of SiC are also found in low oxygen partial pressure environment²³.

This is called active oxidation.

Products of the passive oxidation of SiC are insulator thin films. SiC is the only compound semiconductor that can be thermally oxidized to form high quality SiO₂²⁴. The high-temperature oxidation membrane of SiC can be used as a protective film, a mask during gas etching²⁵, or directly as the gate in Metal Oxide Semiconductor (MOS) structure. The thermal oxide scales of SiC have been reported as amorphous and many types of crystalline silica on different samples in different oxidize conditions^{26, 27, 28, 29, 30, 31}. However, research on oxidation processes such as the formation reaction mechanism of the oxide film, structure of the oxide film, or defects still not fully understood.

1.3 Background and Objectives

In this study, two important topics on SiC; the oxidation and the microstructures of defects in SiC bulk, were chosen for study using electron microscopy and other complementary techniques. These two topics are greatly important topic in the light of using SiC as an electrical device material.

For the study on the oxidation of SiC, we had studied oxide scales formed at 1273 K in air on Si-terminated and C-terminated faces, using transmission electron microscopy (TEM)³² to analyze differences in their oxidation mechanisms. Fig. 1-4(a) shows a cross-sectional electron micrograph of a Si-terminated face, and (b) is that of a C-terminated face after oxidized in air for 100 h at 1273 K. The oxide scales were not uniformly formed. Contrast of crystalline structures in the oxide scale was observed. As mentioned earlier, the thermal oxide scales formed on single crystal SiC can be used directly as gate in MOS structure. The un-uniform oxide scales, as well as the inhomogeneous in the polymorph of oxide scales will cause problems when using as the devices. On the other hand, the information on formations of crystalline silica scales,

characterizations of the formed scales and thicknesses of oxide scales which depend on surface, etc. are necessary on resolving the oxidation mechanism of SiC.

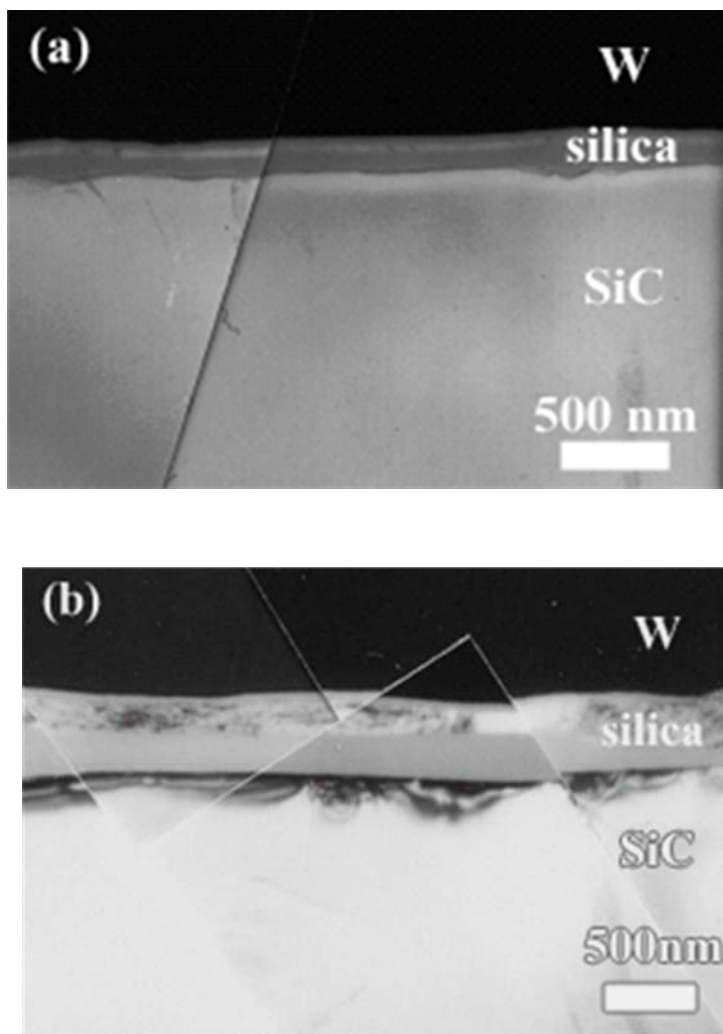


Figure 1-4 : Cross-sectional TEM images of silica scales on specimens without surface pretreatment. (a) Si-face and (b) C-face of specimens oxidized at 1273 K for 100 hours.

Accordingly, it is important to study on the microstructures of the oxide scales form on SiC. Moreover, the inhomogeneous in the thermally formed oxide scales also raised an issue on the study on oxidation kinetics of SiC. So in this study, as well as the microstructures of the oxide scales, a study on oxidation kinetics of SiC, with consideration on the microstructures of the formed oxide scales was also conducted.

For the study on the microstructure of defects in SiC, which is one of the most important issues in development of the SiC devices, the characterization of microstructures of defects will help understanding the mechanisms of the formation of defects. This understanding may lead to reduction of the defect both occur during the crystal growth and during each fabrication processes.

In this study, the cubic SiC (3C-SiC) was chosen as substrate for the study on defects because it is the polymorph that the bulk growth condition is still under development. The growth condition of 3C-SiC has not been optimized, 3C-SiC wafers still have high density of defects at the moment. Besides the characterization of the defects formed during the crystal growth, defects which are induced into the SiC later during each device fabrication process, i.e. ion implantation is also subjected to study in this study.

References

- ¹ J.J. Berzelius, *Ann. Phys., Lpz.*, 1, (1824), 169.
- ² A.G. Acheson, *Engl. Pat.* 17911, (1892)
- ³ J.A. Lely, *Berichte der Deutschen Keramischen Gesellschaft e.V*, 32, 229, (1955)
- ⁴ Y.M. Tairov and V.F. Tsvetkov, *J. Cryst. Growth*, 43, 209, (1978).
- ⁵ P.T.B. Shaffer, *Acta Cryst.*, B25, (1969), 477.
- ⁶ Y. Goldberg, M.E. Levinshtein, S.L. Rumyantsev, *Properties of Advanced Semiconductor Materials*, (2001), 93-148.
- ⁷ R.I. Scace, G.A. Slack, *J. Chem. Phys.* 42 (1965) 805
- ⁸ Y.M. Tairov and V.F. Tsvetkov, *Handbook on Electrotechnical Materials*, (1988), 446-471.
- ⁹ G.L. Harris, *Properties of Silicon Carbide*, INSPEC, Institution of Electrical Engineers, 1995.
- ¹⁰ A.H. Gomes de Mesquita, *Acta Crystallogr.* 23 (1967) 610.
- ¹¹ W.F. Knippenberg, *Philips Research Reports*, 18, No. 3, (1963), 161-274.
- ¹² J.A. Lely, *Berichte der Deutschen Keramischen Gesellschaft e.V*, 32, (1955), 229.
- ¹³ Yu.M. Tairov and V.F. Tsvetkov, *J. Cryst. Growth*, 43, (1978), 209.
- ¹⁴ R.A. Stein and P. Lanig, *J. Cryst. Growth*, 131, 71, (1993).
- ¹⁵ F.C. Frank, *Acta Cryst.*, 4, (1951), 497.
- ¹⁶ R.C. Glass, L.O. Kjellberg, V.F. Tsvetkov, J.E. Sundgren and E. Janzén, *Journ. Cryst. Growth*, 132, (1993), 504.
- ¹⁷ J.A. Powell, J.B. Petit, J.H. Edgar, I.G. Jenkins, L.G. Matus, J.W. Yang, P. Pirouz, W.J. Choyke, L. Clemen and M. Yoganathan, *Appl. Phys. Lett.* 59, (1991), 333.
- ¹⁸ <http://electro.physics.auburn.edu/~bozack/SiCElectronics.html>, (2010)
- ¹⁹ H. Lendermann, F. Dahlquist, J.P. Bergman, H. Bleichner and C. Hallin, *Mater. Sci. Forum*, 389 (2002) 1259.
- ²⁰ G. Manolis, *Physics of Advanced Materials Winter School 2008*
- ²¹ M. Katsuno, M. Nakabayashi, T. Fujimoto, N. Ohtani, H. Yashiro, H. Tsuge, T. Aigo, T. Hoshino and K. Tatsumi, *Mat. Sci. Forum*, 600-603 (2009) 341.
- ²² C.E. Ramberg, G. Cruciani, K.E. Spear and R.E. Tressler, *J. Am. Ceram. Soc.*, 79 (1996) 2897-2911
- ²³ M. Kusunoki, T. Suzuki, K. Kaneko and M. Ito, *Philos. Mag. Lett.* 79 (1999), 153-161
- ²⁴ C. Radtkea, R. V. Brandão, R. P. Pezzia, J. Moraisa, I. J. R. Baumvola and F. C. Stedile, *Nuclear Instruments and Methods in Physics Research Section B: Beam Interactions with Materials and Atoms*, 190 (2002) 579-582.
- ²⁵ W.V. Munch and I. Pfaffeneder, *Solid-State Electron.* 21 (1978) 479.
- ²⁶ L.U.J.T. Ogbuji and M. Singh, *J. Mater. Res.*, 10 (1995) 3232.
- ²⁷ G.H. Schiroky, *Adv. Ceram. Mater.*, 2 (1987) 137.
- ²⁸ J.A. Costello and R.E. Tressler, *J. Am. Ceram. Soc.*, 64 (1981) 327.
- ²⁹ P.F. Tortorelli and K.L. More, *J. Am. Ceram. Soc.*, 86 (2003) 1249.
- ³⁰ J.A. Costello and R.E. Tressler, *J. Am. Ceram. Soc.*, 69 (1986) 674.
- ³¹ J.F. Guinel and M.G. Norton, *J. Mater. Res.*, 21 (2006) 2550.
- ³² N. Tarumi, B. Chayasombat, T. Matsuoka, K. Sasaki and K. Kuroda, *Japan Institute of Metals, 2006 Fall Annual Meeting*.

Chapter 2: Experimental Instruments and Procedures

2.1 Focused Ion Beam: FIB

Recently, researches of materials, especially in development of producing new functions from materials, are highly attracting attention and rapidly progressing. In order to understand more thoroughly on how and why the materials function and have characteristic as they do, transmission electron microscopy (TEM) nano-structure analysis is competently used. And generally, the TEM observation of interfaces between different phases gives important information which can be used to analyze the characteristic of materials. However, due to the different in hardness and chemical properties of each phase, thinning of TEM specimens which focusing on the specific interface area is difficult. Chemically polish electro polishing or argon ion milling has traditionally been used mainly for metals, but these methods can only apply to certain types of materials. Also, it is very complex and difficult to mill focusing on the particular location.

In recent years, the Focused Ion Beam (FIB) method is applied in many fields especially TEM analyses. The applications are such as fabrications of semiconductor devices or failure analysis using TEM. This method was originally used to repair the wiring in semiconductor device technology¹. The characteristic of this method is the good precision machining position. As the scales of many industrial process and product are expanding from micro- level into nano- level, the refined precision is very significant and absolutely necessary application. This makes FIB a very capable method for modern age technologies.

The basic structure of FIB system is shown in Fig. 2-1. Liquid metal ions are emitted from the tip of the emitter at the extraction voltage (approximately 8 eV). Emitted ions are accelerated to 1-40 keV voltage, and the focused ion beam diameter is controlled by aperture under condenser lens.

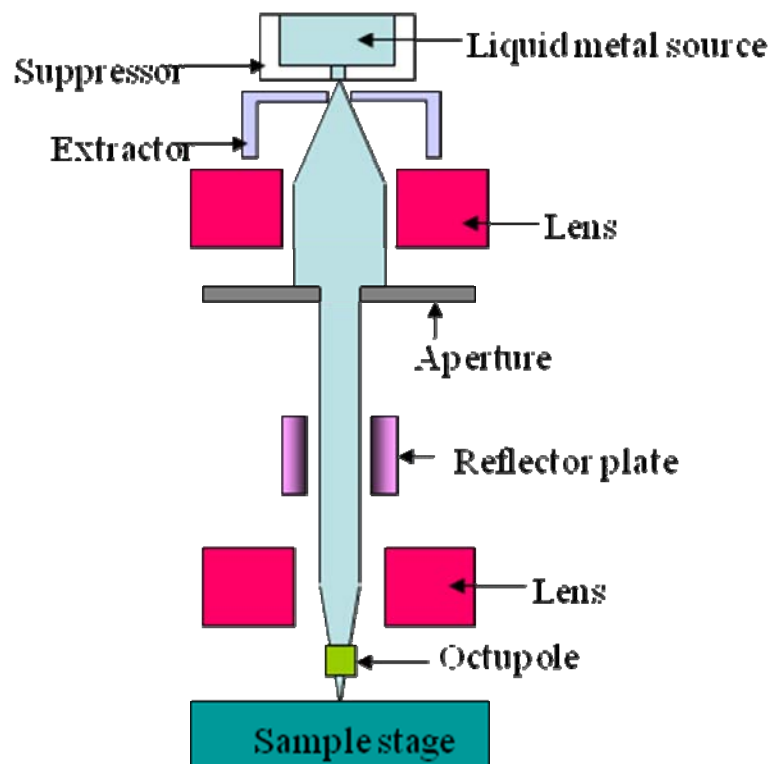


Figure 2-1 : Basic structure of FIB.



Figure 2-2 : Hitachi NB- 5000 FIB- SEM dual system.

The beam position on the specimen is controlled by beam deflector placed at the middle of the column. Mentioned is the basic structure of FIB, but for practical use, aligner and stigmator must be set up under the condenser lens. The aligner is placed in order to adjust the axis of ion beam which incident through the objective lens and stigmator is placed for the correction of the beam shape distortion. Moreover, the beam current monitor is equipped so that the ion beam current can be measured while processing.

In the specimen chamber, secondary electron detector is being equipped for Scanning Ion Microscope (SIM) image of specimen surface which is used for setting the processing region on the specimen and for observing the change of shape continuously during the process. Generally FIB is high-vacuum device, the vacuum near the ion source is 10^{-6} Pa order, and the vacuum in the specimen chamber is of 10^{-5} Pa order. Fig. 2-2 shows FIB system used in this study (Hitachi NB-5000 FIB –SEM dual system).

2.1.1 Micro-sampling Technique

FIB micro-sampling technique² is used for all the thinning of TEM specimens in this research. FIB micro-sampling technique allows us to cut out small areas of samples ($20\mu\text{m} \times 30\mu\text{m} \times 2\mu\text{m}$) directly from bulk samples in a FIB system. The schematics of FIB micro-sampling-argon milling technique^{3,4} are shown in Fig.2-3.

First, molybdenum mesh was cut to the shape as shown in Fig. 2-3(a). Then thin aluminum foil (approximately $2\mu\text{m}$ thick) was attached to the mesh (Fig. 2-3(b)) to be used as a metallic carrier. The advantage of using thin foil as carrier is that, after milled by FIB, further argon milling can be effectively applied in order to remove damage layers induced by gallium ion beam. Next, the area of interest protected by vapor-deposited tungsten carbonyl ($\text{W}(\text{CO})_6$), which has low sputtering rate, in order to protect the specimen surface from gallium ion sputtering during the FIB milling. After tungsten vapor-deposited, the bulk specimen is dug out around the area of interest, and then the area of interest is picked up by tungsten probe (Fig. 2-3(c)). The picked up

micro-sample is then deposited on a metallic carrier as shown in Fig.2-3(d). The deposited specimens are further milled until becoming electron transparent thin foil specimen (approximately about 100 nano-meters in thickness) (Fig.2-3(e)). Clear high-resolution images can be observed using this method of FIB-Ar ion milling to prepare the specimens^{3,4}.

The advantages of FIB micro-sampling techniques are;

- 1) The areas of interest are determined simply by SIM images. The TEM specimen fabrication on precise area of interest is then can be easily picked up.
- 2) The TEM specimens can be lifted up directly from bulk samples without mechanical polishing. The mechanical polishing can cause strains in the samples and the risk of destruction due to mechanical polishing is high in brittle materials. Therefore micro-sampling technique can be applied to most of materials.
- 3) Comparing to conventional argon ion milling method, the FIB micro-sampling technique consumes less time.

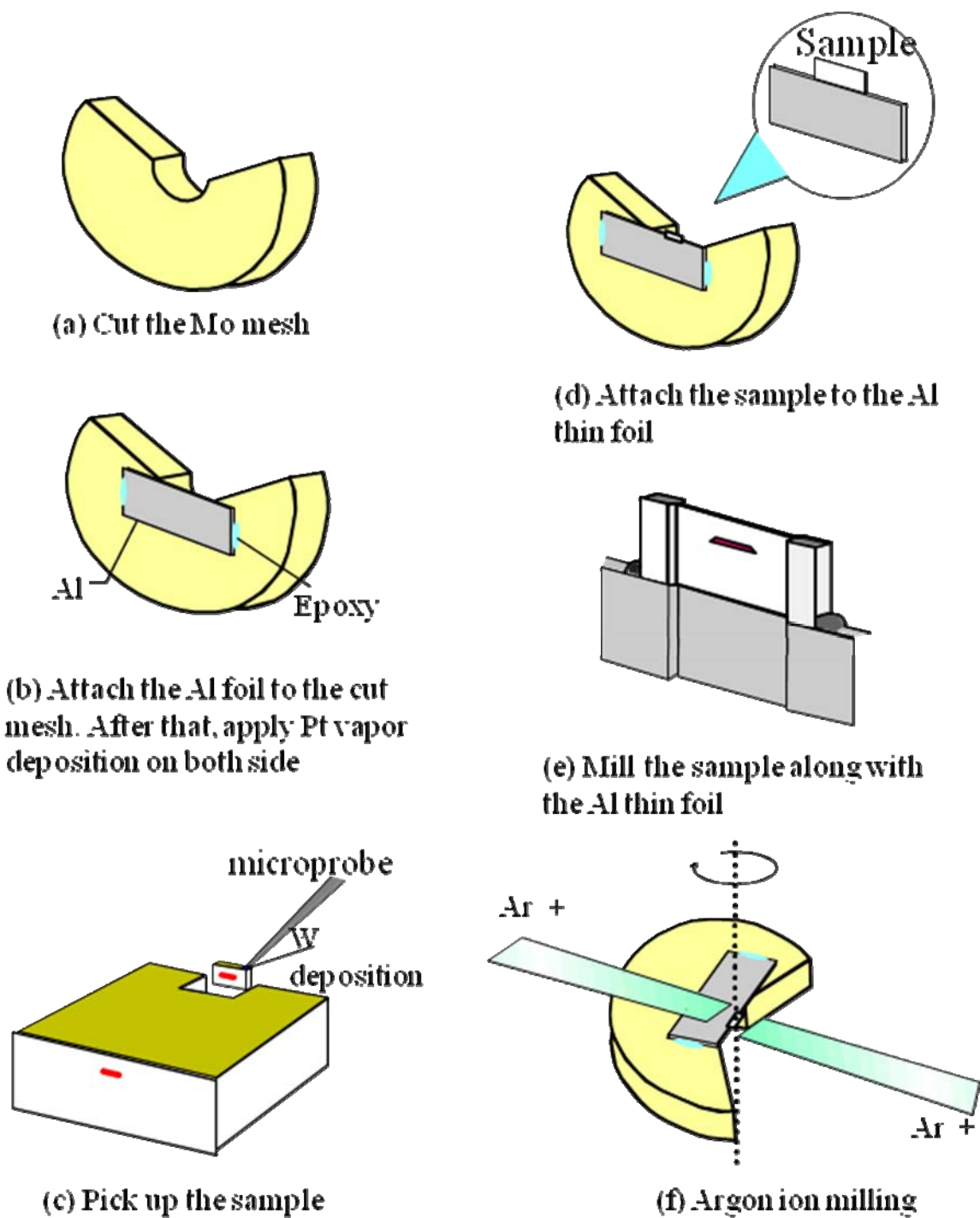


Figure 2-3 : Schematics of FIB micro-sampling – argon milling technique.

2.1.2 FIB-SEM Dual System

FIB-SEM dual system is a system where FIB and SEM system is set up so that both systems can operate on the specimen at the same time. In HITACHI NB-5000 system, the SEM system was set to 58 degrees from tilted FIB system, as shown in a schematic in Fig. 2-4. In this way, the specimen fabrication can be conducted by Ga ion from FIB system, and observation can be made by SEM system from 58 degrees angle. FIB system can produce SIM image, which can be used for pinpointing the location of TEM specimen preparation. However, visualization by Ga ion will induce damages to the surface of the sample. Accordingly, in order to minimize the damages to the surface of the specimen, the visualization of the surface of the sample by SEM system is preferred compared to FIB system. Moreover, the angled set up of the FIB and SEM columns enable fabrication and observation of the cross-sectional structure at the same time. By using this feature, it is possible to reconstruct three dimensional structure of the samples by repeating fabrication and cross-sectional observation on the same sample and combining the image using 3D software.

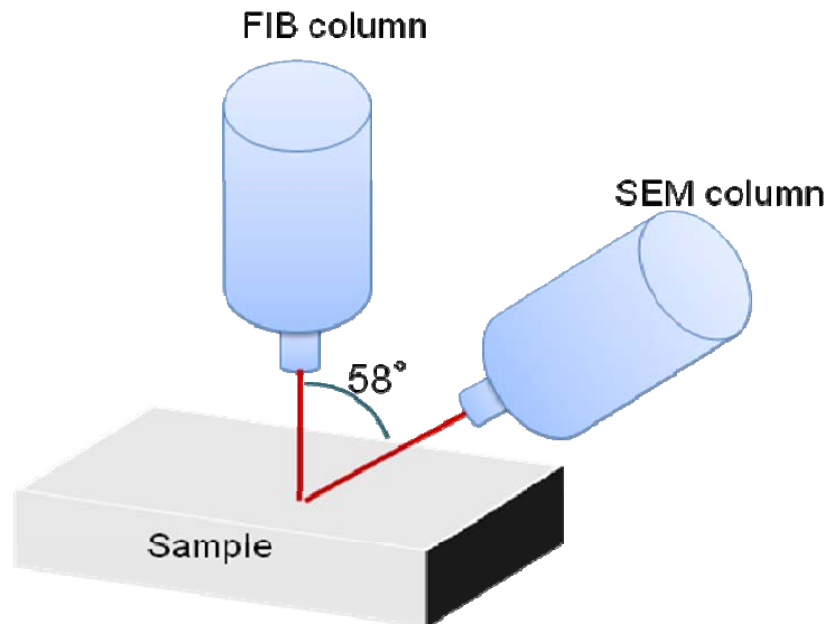


Figure 2-4 : Basic structure of FIB-SEM dual beam system (Hitachi NB-5000).

2.2 Transmission Electron microscopy: TEM

2.2.1 The Outline of TEM

TEM is a technique which irradiates the electron beam to a relatively wide range of thin, electron transparent, specimen. The transmitted electron beam is then expanded and the images are gained. Accordingly, the images gained contain of the internal structure information on the local area of the specimen which the electron beam has been transmitted. The analysis of atomic arrangement of crystalline materials, in other words structural analysis, has been performed by using the conventional X-ray or neutron beam diffraction techniques. These techniques, the structural analysis is accurate for the average structure of the crystalline. However, practically, the crystal lattice contains defects of various sizes, vacancy, dislocation, stacking faults, grain boundary, interface, etc. These kinds of focal structural information cannot be obtained by the X-ray and neutron diffraction techniques. Hence, transmission electron microscopy technique which is appropriate for observing the mentioned micro-structures is absolutely necessary for material development. Transmission electron microscopy makes immeasurable contribution to materials engineering field these days. The basic structure of TEM is shown in Fig. 2-5. Fig. 2-6 shows TEM used in oxidation studies, the JEM 2010 DM made by JEOL.

The materials researches using TEM have a series of processes as followed; "TEM specimen preparation", "observation" and "data analysis". Among these processes the nature of TEM specimen has a great effect on subsequent processes so the nature of specimens is particularly important. Generally, the good TEM specimens are; electron transmitted, thin, have flat surfaces, no damages to the specimen, have no contaminations and any bending, etc.

In order to meet with these conditions, the milling technique and the milling condition must be selected appropriating to the observation materials and the purpose of

observation.

The TEM imaging techniques used in this study TEM are bright-field and dark-field imaging, high-resolution electron microscopy (HREM), and selected area diffraction pattern (SADP)

In crystalline specimen, the electron beam that transmitted through the specimen is divided into a transmitted wave and diffracted wave. By selecting proper beams for imaging, a meaningful contrast with the image can be obtained. The contrast which reflected in specimen diffraction conditions is called diffraction contrast. The objective aperture is placed on the focal plane in TEM. The objective aperture is a thin metal plate which has little holes in different sizes. The observers can move this aperture freely on the focal plane in order to select the transmitted wave or the diffracted wave (in some cases, both are selected) which will be used for imaging.

Bright-field imaging uses only transmitted wave, and dark-field imaging uses only one diffracted wave to obtain the images. SADP is the diffraction pattern that gain from area selected by putting selected area aperture on desired area of the specimen. The electron diffraction pattern contains a lot of information, such as the specimen structure, Bragg condition and the existence of defects. The structural analysis of the focal area on the specimen can be performed based on this information acquired from each imaging techniques.

As shown in Fig. 2.7(a), the background of zirconium oxide-alumina powder sample is brightly imaged in the bright-field image. If the image is formed without fully applying the objective aperture, the majority of the diffracted beam will contribute to the imaging which will result in weak contrast of the image. That is an example that the objective aperture can enhance the contrast of the formed image.

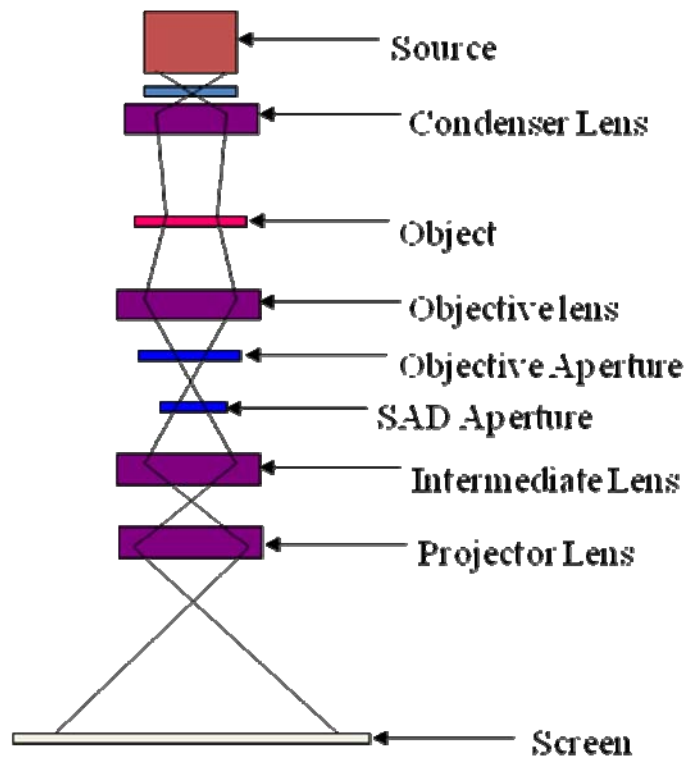


Figure 2-5 : Basic structure of TEM.



Figure 2-6 : JEM 2010 DM made by JEOL.

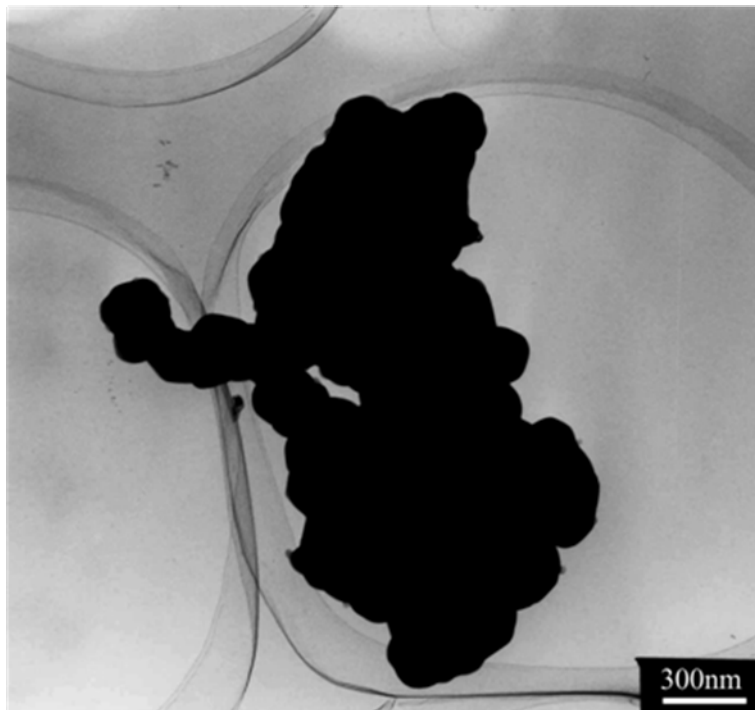


Figure 2-7 : (a) Bright-field image of zirconium oxide and alumina powder.

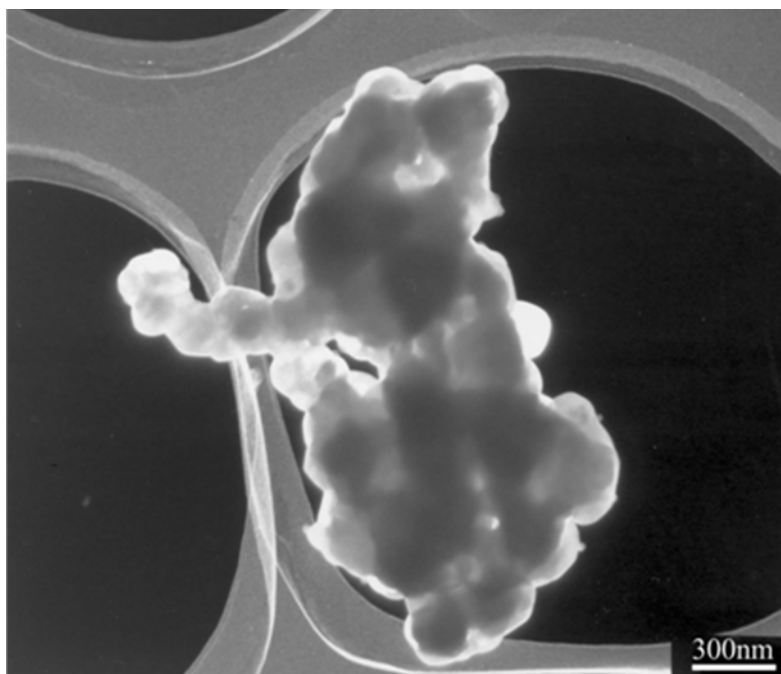


Figure 2-7 : (b) Dark-field image of zirconium oxide and alumina powder.

Meanwhile, the dark-field image is formed from a diffracted beam; accordingly the image will contain the certain information of its originated diffraction beam. In this case, unlike the bright-field image, the background of the sample which has no diffracted beam is dimmed.

In the actual TEM observation, the image quality will significantly improve if the imaging beam agrees well with the optical axis. Conversely if the dark-field image is formed by the beam which the inserted objective aperture is shifted from the accelerating voltage center, the electron beam below the objective aperture is out of alignment from the electron optical axis and the influence from the spherical aberration is remarkable, and the image will become defocused. In order to avoid this problem, the direction of the incident electron beam which irradiated on the specimen beam is tilted so that the aimed diffracted wave is located on accelerating voltage center (the position which the transmitted wave is usually located). Fig. 2.7 (b) is the image imaged by tilting the incident beam. A sharp dark-field image is gained.

2.2.2 Contrast Experiment

Burgers vector, **b**, represents magnitude and direction of the dislocation in crystal structure. The magnitude of Burgers vector is determined by the lattice parameter. Normally, the magnitude is equal to distance between atoms in the close-packed direction. On the other hand, the direction of Burgers vector is determined by the direction of close-packing. In the case where the dislocation is located in simple lattice face, the dislocation vector **R** can be shown as;

$$\mathbf{R} = a\mathbf{b}$$

where *a* is a constant and **R** is the displacement vector.

In this study, the characterizations of microstructure of defects were conducted using TEM contrast experiment, or Burgers vector analysis. Contrast of TEM image come from the strains field that existed in the crystal lattice. This contrast is determined by

phase factor which can be defined as;

$$\alpha = 2\pi \mathbf{g} \cdot \mathbf{R}$$

where α is phase factor, \mathbf{g} is the reciprocal lattice vector (or diffraction vector). When the direction of reciprocal vector is perpendicular to the direction of the Burgers vector, $\mathbf{g} \cdot \mathbf{b} = 0$, so $\alpha = 0$, so that the contrast of dislocation disappear. From this principle, the direction of Burgers vector can be determined by imaging the same dislocation with different diffraction vectors and observing the contrast. When at least 2 conditions of cases where dislocation contrast disappear were found, the direction of the displacement vector or Burgers vector can be concluded.

References

- ¹ E.C.G Kirk, J.R.A. Cleaver, H. Ahmed, *Inst. Phys. Conf. Ser.*, 84(1987) 691
- ² T. Onishi, H. Koike, T. Ishitani, S. Tomimatsu, K. Umemura and T. Kamino, *Proc. 25th Int. Symp. For Test. And Fail. Anal.*, (1999), 449-453.
- ³ T. Matsuda, *Materia Japan*, 42 (2003) 916.
- ⁴ H. Sasaki, T. Matsuda, T. Kato, T. Muroga, Y. Iijima, T. Saitoh, F. Iwase, Y. Yamada, T. Izumi, Y. Shiohara and T. Hirayama, *J. Electron Microsc.* 53 (2004) 497-500.

Chapter 3: Oxidation Kinetics of Silicon Carbide

3.1 Introduction

At high temperature, in sufficient oxygen partial pressure environment, protective silica oxide scales are known to form on SiC. These oxide scales can be used as protective film in various processes. Many studies have been conducted on the passive oxidation of SiC over years^{1, 2, 3, 4, 5, 6}. Despite the numerous studies conducted on oxidation kinetics, the oxidation mechanisms still cannot be concluded. One of the main reasons for the indetermination was the extremely wide variation of the reported data, the oxidation rates and the oxidation activation energies. These variations are presumably originated from the differences in samples used, experimental condition, experimental procedures conducted, or methods for oxidation rate evaluation. This then leads to differences in oxidation rates reported, and as consequences, lead to different activation energies calculated and reported.

3.2 Previous Studies on Oxidation Kinetics of SiC

Studies on oxidation kinetics for SiC have been conducted for at least in the past 5 decades. So far, the SiC samples used in each study were varied from sintered SiC to high quality single crystal SiC. Early studies on oxidation rates of SiC used thermo-gravimetric analysis (TGA) as a method for measurement of the thermally formed oxide scales^{3, 4, 7}. The TGA method uses the conversion of mass gain due to oxidation reaction into the oxide scale thickness (cf. oxidation reactions in chapter 1, section 1.5). The accuracy of the calculated oxide scales depends highly on the formula used for conversion, as well as corrections for variations. Because the oxide scale grows inward into the SiC substrate, so the surface area where the reactions occur, would be less as the growth of the oxide scales continued. And this surface reaction area is used in the conversion to calculate mass gain into the thickness so the conversion from mass gain into oxide scale thickness can be complicated. Moreover, if the formed silica

scales are porous, inhomogeneously formed, losing mass due to the spallations, or crystallization of the oxide scales occurs, the conversion of mass gain would yield further inaccuracy in thickness. In addition, for the sintered SiC, the reaction between contaminations, i.e. sintering aid, and the oxidants must also be considered. Besides these limitations, it had been reported in many studies that the oxidation rate on different crystal face is different in SiC, therefore, one of the most important restrictions for TGA is that it cannot distinguish between the thickness of the formed oxide scale on each crystal face. However, despite these restrictions, TGA is still considered a powerful and convenient method for studies of oxidation of polycrystalline SiC.

For the studies on oxidation of SiC where the oxidation rates of each crystal face needed to be distinguished, ellipsometry is the most commonly used method for measurement of the thickness of the formed oxide scales⁸. The measurement from ellipsometry can be very accurate (in nm orders) in cases where oxide scales are homogeneously formed and appropriate model for oxide scales thickness calculation is chosen.

The oxidation kinetics of SiC is mostly described by a model developed by Deal and Grove in 1965⁹. This model was originally developed for the oxidation of silicon, but it also can be applied extremely well with the oxidation of SiC. The model derived a general linear – parabolic relationship between the thickness of the formed oxide scale and the oxidation time as described in equation (1);

$$X^2+AX=B(t+\tau) \quad (1)$$

Where, X is the thickness of the oxide scale, t is oxidation time and τ is constant related to initial thickness of oxide scale prior to the oxidation. B/A and B is called linear rate constant and parabolic rate constant, respectively. In the case where the oxide scale is sufficiently thick, the linear term can be neglected and the parabolic rate will become dominant.

It was stated in the study of Deal and Grove that, in case of a relatively long reaction time, the Deal-Grove general relation would reduce to simple parabolic law. The studies of Costello (1986)⁶ and Zheng (1990)⁸ who reported oxidation kinetics of the Si-face and the C-face of SiC, use the reduced parabolic model in their studies, while the studies of Harris (1975)¹², Ramberg (1996)⁴, Vickridge (2007) and Song (2004)¹³ used the linear-parabolic model for the fitting of their experimental data. Table 3-1 shows experimental settings of some previous studies. It can be seen from the table that, obvious specific oxidation time or specific oxide scale thickness that determine where linear rate constant can be neglected and reduced parabolic model is applicable, cannot be determined from these studies.

3.3 Background and Objective

Previously, we characterized the microstructures of the oxide scales formed on the sample oxidized at 1473K for 16 hours¹⁰. Fig. 3-1 shows optical microscope (OM) image of the Si-face of the sample after oxidation. Glossy patterns, that were not existed before the thermal oxidation, were observed to be randomly distributed on the surface of the sample after oxidation. Fig. 3-2 (a) shows OM image of the sample after oxidation at 1473K for 16h, (b) and (c) show cross-sectional TEM images of the specimens took from region A, the region without the patterns, and region B, the region with the glossy pattern. The thickness of the oxide scales from region B is not even. The oxide scale thickness of this region varied from 15 to 30 percents thicker than the oxide scale from region A. As shown by Chayasombat et al.⁷, the thickness of oxide scales where crystalline phase silica existed can be varied from a few to more than 100 percents thicker than the region where the oxide scale composed of only amorphous silica. It can be concluded from these observations that the oxide scale in the region with glossy patterns is not uniform and composed of both crystalline and amorphous silica.

Table 3-1 : Experimental settings of some of previous studies.

Reference	Model	Temperature range	Oxidation time	Method
Costello (1986)	parabolic	1473-1773K	up to 24h	ellipsometry
Zheng (1990)	parabolic	1473-1773K	up to 8h	ellipsometry
Harris (1975)	linear-parabolic	1243-1518K	0.5-340h	interferometer
Ramberg (1996)	linear-parabolic	1073-1373K	up to 150h	ellipsometry
Vickridge (2007)	linear-parabolic	1373K	up to 50h	ellipsometry
Song (2004)	linear-parabolic	1223-1373K	up to 6h	ellipsometry

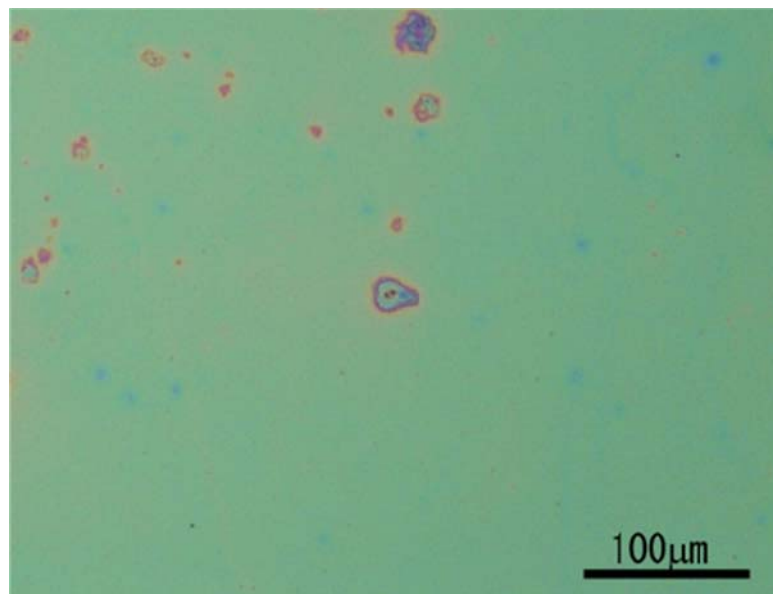


Figure 3-1 : OM image of the Si-face of sample after oxidation at 1473 K for 16 hours.

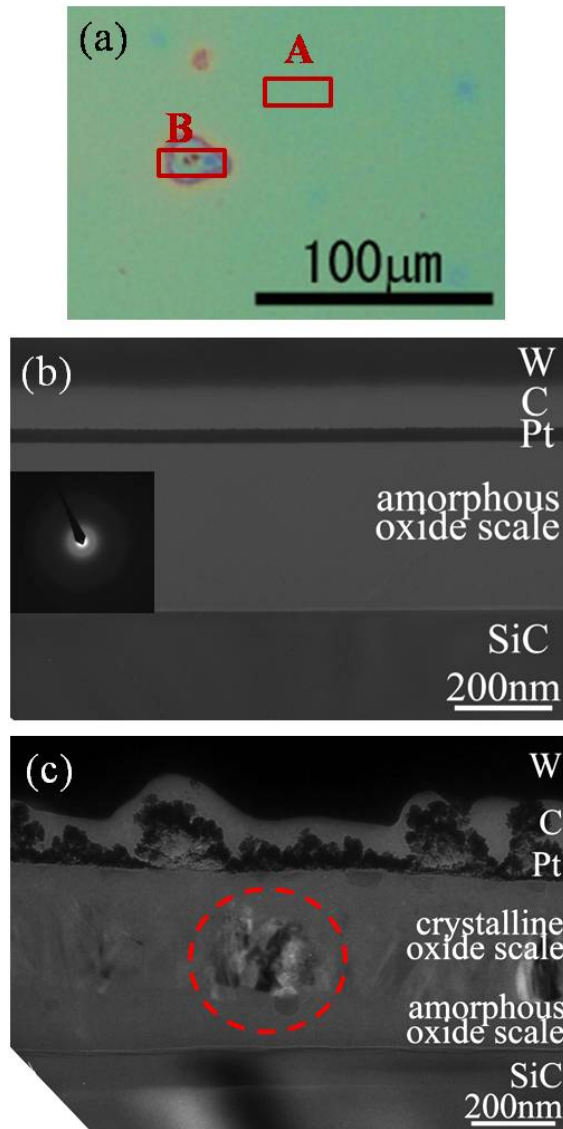


Figure 3-2 : (a) OM image of the sample oxidized for 16h (b) cross-sectional TEM image of region A, and (c) cross-sectional TEM image of region B.

As stated earlier, in previous studies on oxidation kinetics of SiC by other investigators, the most frequently used methods for oxide scale thickness measurement were gravimetry or ellipsometry. These methods measured the thickness of the formed oxide scales from unspecified and relatively wide region of the samples (mm order in case of ellipsometry and from mm to cm order in case of gravimetry), and it may lead to errors in thickness measurements. For the gravimetry, the most problematic point is that the oxide scale thickness of the Si-face and the C-face cannot be distinguished. And for the ellipsometry, the method that depend highly on the model chosen for calculations, the random distribution of these crystalline oxide scales, which has different refractive index than the amorphous oxide scale, as well as random variation in thickness of the oxide scales in the regions where crystalline phase silica exist, will lead to an inaccuracy in thickness measurement. Accordingly, it is crucial to specify the regions in which the thickness of the oxide scales will be measured in order to get accurate thickness measurements of the formed oxide scales.

In this study, hexagonal 6H-SiC was chosen as experimental substrate because of its low density of defect and high crystal quality. Oxidation rates of the Si-face and the C-face of the single crystal SiC were measured by direct measurement of the thickness of the oxide scale specifically from the regions composed of only amorphous phase silica using electron microscopy to ensure the accurate thickness measurement. And in order to minimize the effect of other parameters on oxidation kinetics, the high quality single crystal 6H-SiC samples were oxidized in pure dry oxygen in the environment where the contamination level was minimized.

3.4 Experimental Procedures

A single crystal 6H-SiC wafer obtained from Cree Inc. was used in this study. The obtained wafer was n-type, and it was polished on both the Si-face and the C-face. The wafer was cut into $10 \times 10 \text{ mm}^2$ size and rinsed successively in high purity acetone and ethanol. The samples were then loaded onto a quartz sample holder and put into the

quartz tube furnace. The quartz sample holder and the quartz furnace tube were cleaned in HF prior to the oxidation experiments. The use of quartz sample holder and furnace tube was to minimize the effects on oxidation from contaminations as reported in the case of alumina furnace tube¹¹. Flowing 99.999 percents dry oxygen was run for 2 hours prior to the oxidation to ensure pure oxygen environment. The furnace system was then heated up with temperature gradient of 10 degrees/min. The oxidation condition was 1273 K – 1473 K from 1 to 25 h in flowing oxygen at 1 atm. Fig. 3-3 shows schematic of the experimental setup of the furnace and Fig. 3-4 shows temperature as function of time for the oxidation experiments.

The oxidized samples were then observed using OM to identify the regions where the oxide scales composed of only the uniformly formed amorphous silica. Then, platinum was deposited on the surface of the samples to prevent electrical charging. After carbon and tungsten deposition for protecting the surface of specimens, cross-sectional SEM or TEM specimens were prepared from the regions where oxide scales composed of only uniform amorphous silica by FIB micro-sampling technique using a HITACHI NB-5000 FIB-SEM system. Schematic of the FIB-SEM system is shown in Fig. 3-5 Thicknesses of the thermally formed oxide scales were measured using SEM at an accelerating voltage of 5 kV. An example of measurement by SEM is shown in Fig. 3-6. The thickness measure from SEM was 340 nm, and the thickness measure directly from TEM was 350nm. Therefore, accurate thickness measurement using SEM was ensured. However, in the cases where the formed oxide scales were thinner than 100 nm, the measurements were conducted directly using TEM, a JEM-2010 at an accelerating voltage of 200 kV.

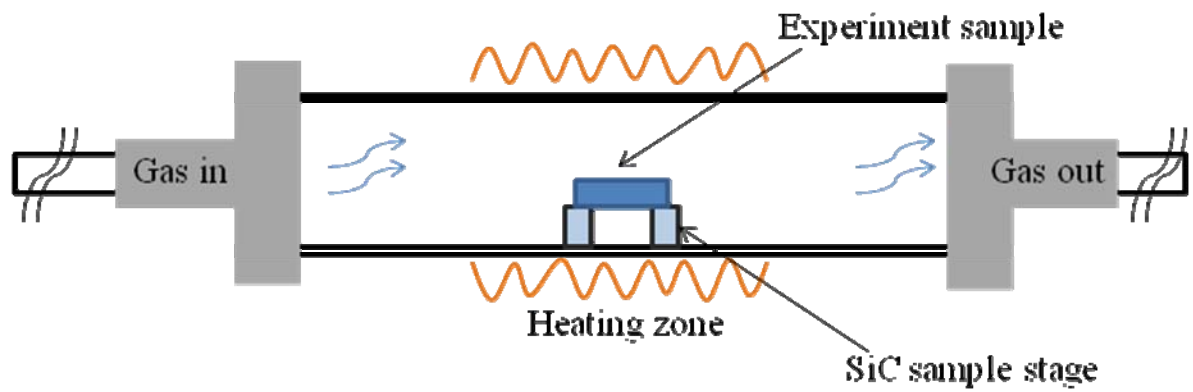


Figure 3-3 : Schematic of furnace setup.

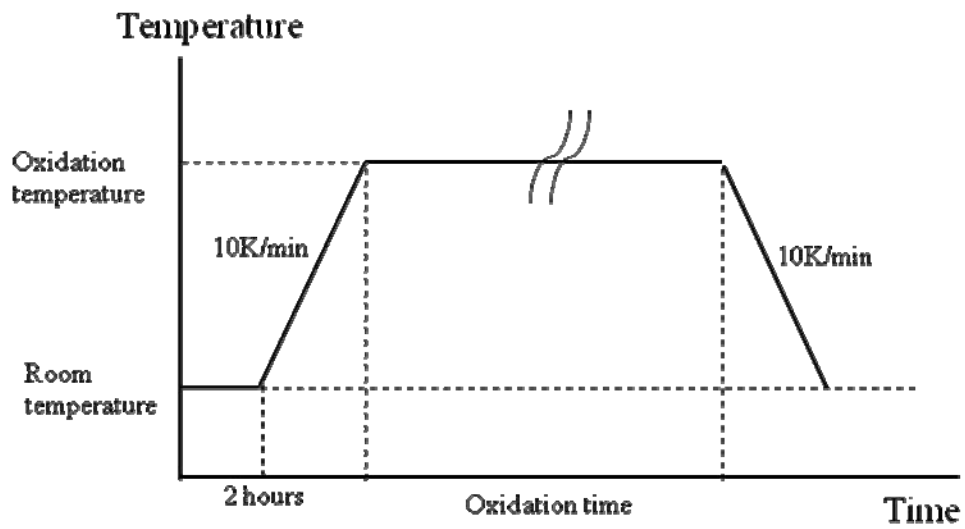


Figure 3-4 : Temperature of the experimental samples as a function of time.

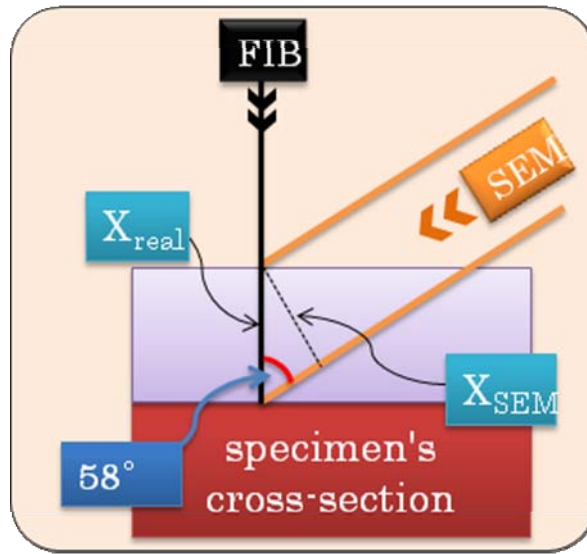


Figure 3-5 : Schematic of FIB-SEM dual beam system.

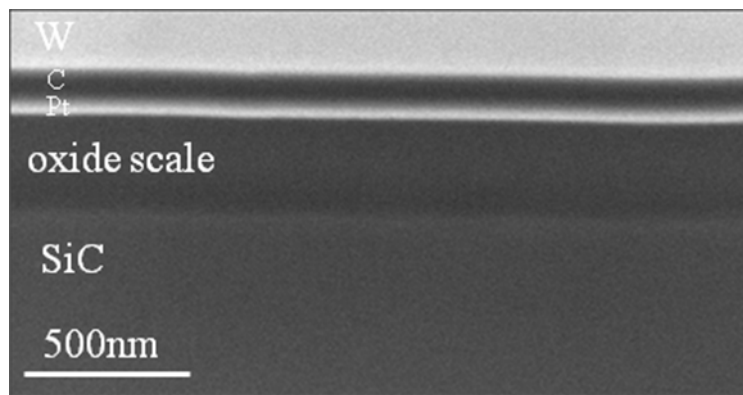


Figure 3-6 : SEM image of oxidized sample.

3.5 Results and Discussion

The thickness of oxide scales were measured from approximately 20 micrometers range of each sample (the width of the TEM specimens) and the average thickness of each sample from each oxidation condition were taken from 20 points of measurements. Figure 3-7 (a), (b) and (c) show cross-sectional TEM images of the Si-face of the samples oxidized at 1273 K, 1373 K and 1473 K for 1 h, respectively. The average thickness of each formed oxide scales were, 6 nm, 14 nm and 41 nm, respectively. Fig. 3-8 (a), (b) and (c) show cross-sectional TEM images of the C-face of the samples oxidized at 1273 K, 1373 K and 1473 K for 1 h, respectively. The average thickness of the oxide scales were, 38 nm, 81 nm and 151 nm, respectively. All TEM specimens were taken from the regions without glossy patterns. The oxide scales were uniformly formed and composed of only amorphous silica. For the same oxidation time and temperature, the oxide scale formed on the C-face was thicker than that of the Si-face. This agrees well with previous studies which reported that the C-face oxidizes 5-10 times faster than that of the Si-face^{1, 6, 12, 13}.

Fig. 3-9 (a) and (b) show oxide thickness as a function of time for each oxidation temperature for the Si-face and the C-face, respectively. The error spans of each thickness measurement are also shown.

3.5.1 Model for Oxidation Kinetics

As mention in section 3.2, the oxidation kinetics of SiC is mostly described by a model developed by Deal and Grove¹⁴. The model originally developed for the oxidation of silicon, but it also can be applied well with the oxidation of SiC. The model derived a general linear – parabolic relationship between the thickness of the formed oxide scale and the oxidation time as equation (1);

$$X^2+AX=B(t+\tau)$$

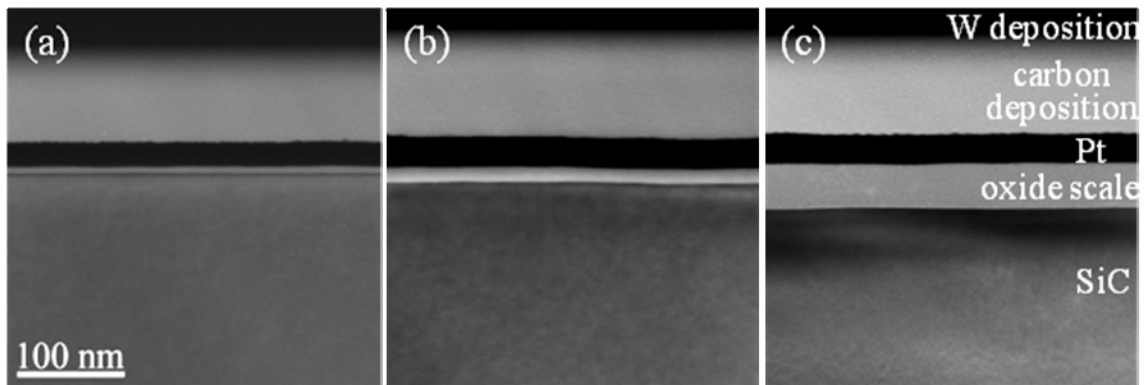


Figure 3-7 : Cross-sectional TEM images of the Si-face of the samples oxidized at 1273K, 1373K and 1473K for 1h, 9h and 16h, respectively.

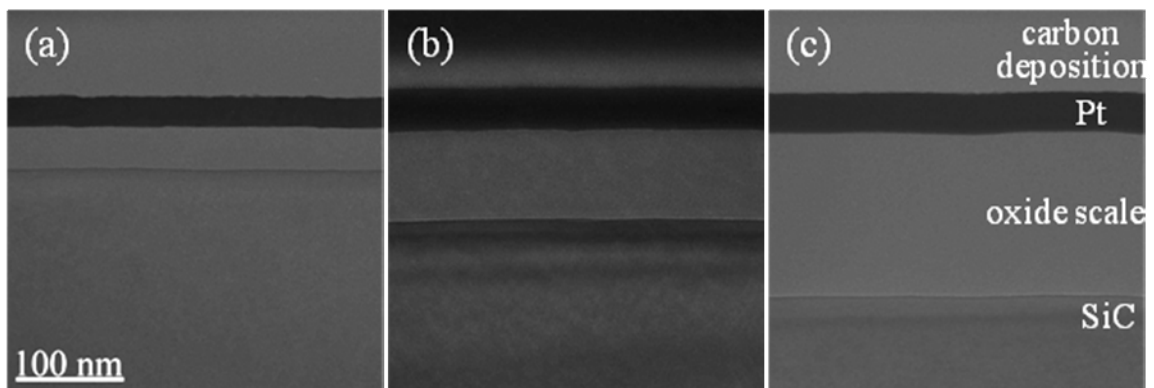
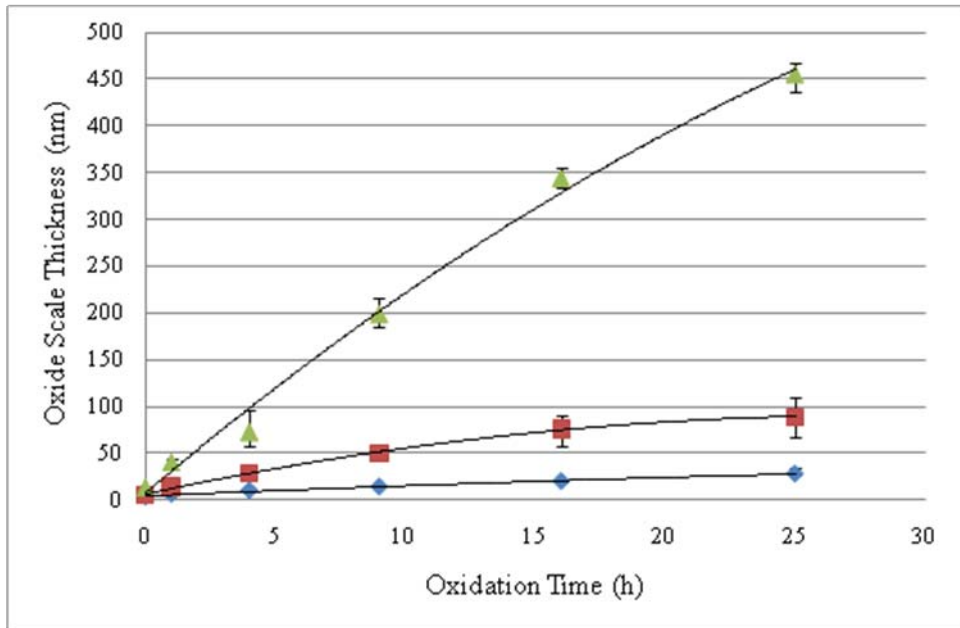


Figure 3-8 : Cross-sectional TEM images of the C-face of the samples oxidized at 1273K, 1373K and 1473K for 1h, 9h and 16h, respectively.

(a)



(b)

◆ 1273K ■ 1373K ▲ 1473K

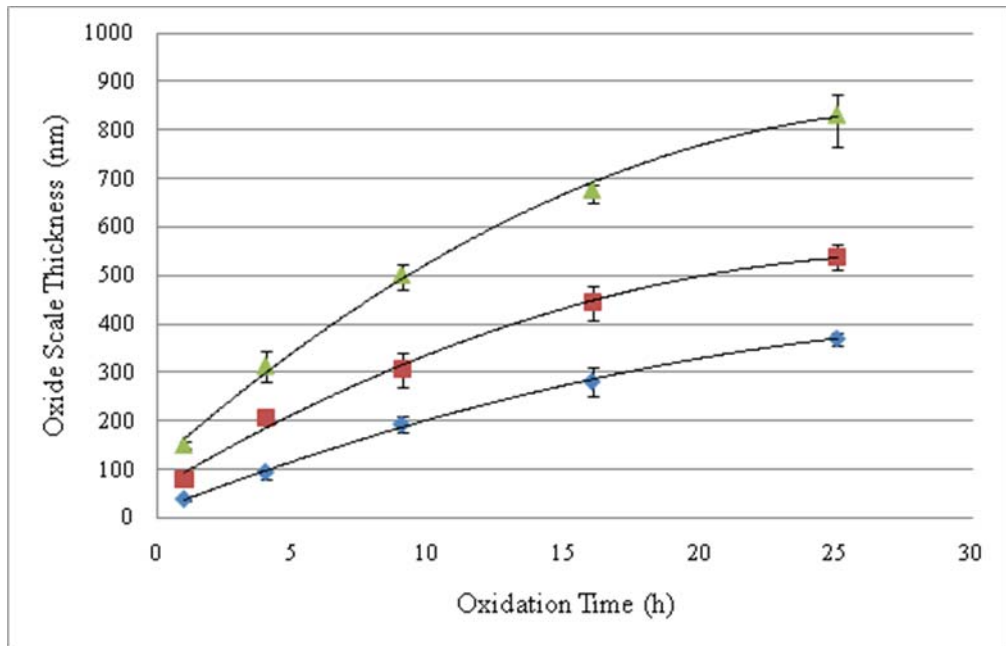


Figure 3-9 : (a) and (b) show oxide thickness as a function of time for each oxidation temperature for the Si-face and the C-face, respectively.

Where, X is the thickness of the oxide scale, t is oxidation time and τ is constant related to initial thickness of oxide scale prior to the oxidation. In this study, the Deal-Grove model is chosen for the fitting of measured data. Considering from the range of the oxidation temperatures which are relatively high and the oxidation times which are relatively long, as well as from the range of measured thickness (mostly from tens nm to hundreds nm order), the data analysis of the fitting was focus only on parabolic rate. Since the data points in the regions of initial oxidation were not frequently taken enough for the analysis of the initial oxidation, the linear term of the relationship is not considered in this study.

3.5.2 Oxidation Rates of the Si-face and the C-face

We fitted our experimental data with the Deal-Grove model to determine the rate constants for each oxidation temperature. The fittings of the Deal-Grove model are shown in solid lines in Fig. 3-9 (a) and (b). The parabolic rate constants B derived from the fittings and the correlation coefficient, R^2 , are shown in Table 3-2. The correlation coefficient is a measure of the interdependence of two random variables. The value of the correlation coefficient varies from 0 to 1. When correlation coefficient is 0, the relation between two variables is absent. It is indicated that two variables have perfect positive correlation when $R^2 = 1$. It will get close to 1 if the experimental data fitted well with the used model. From the R^2 value show in Table 3-2, it can be concluded that our experimental data fitted very well with the chosen Deal-Grove model.

3.5.3 Oxidation Activation Energies of the Si-face and the C-face

From the parabolic rate constants of our study, using the Arrhenius equation (Eq. (2)), we determined the oxidation activation energy of the Si-face and the C-face.

$$K = F \exp(-E_a/k_B T) \quad (2)$$

Where, K is temperature dependent time constant (in this case the parabolic rate constants), F is pre-exponential factor, Ea is the activation energy, k_B is the Boltzmann's constant and T is the oxidation temperature. Arrhenius plot of parabolic rate constants derived from thickness measurements of our study is shown in Fig. 3-10.

Table 3-2 : The parabolic rate constants B derived from the fittings and R^2 .

Temperature (K)	B (nm ² /h) Si-face	R ²	B (nm ² /h) C'-face	R ²
1273	188.7	0.998	8850	0.999
1373	357.1	0.985	11862	0.996
1473	20408	0.992	26596	0.999

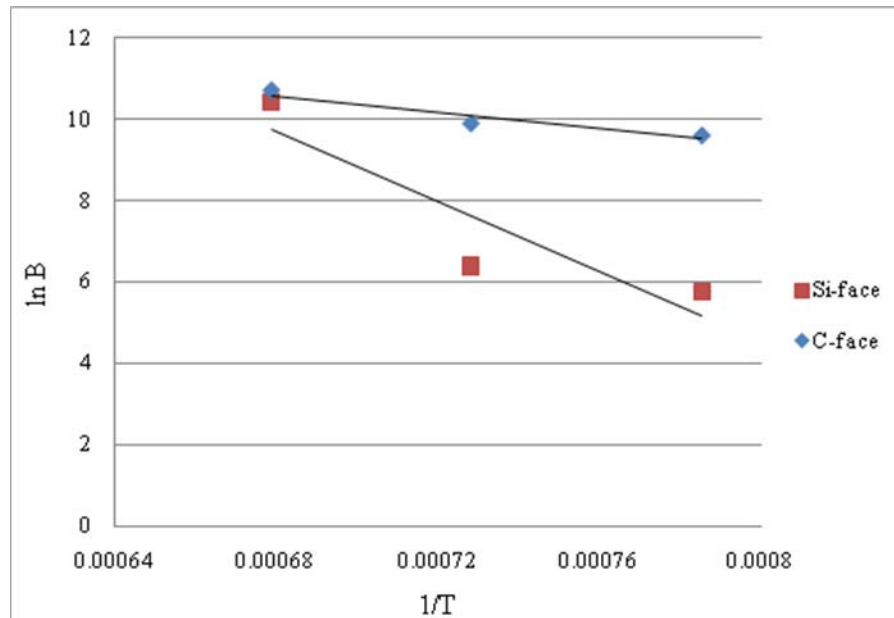


Figure 3-10 : Arrhenius plot of parabolic rate constants.

From the slopes of these plots, we determined the activation energies for oxidation of the Si-face to be 358 kJ/mol and the C-face to be 85 kJ/mol.

Many studies reported oxidation activation energies of SiC^{1, 3, 4, 6, 9, 10, 15, 16, 17, 18, 19, 20}. Among these studies, the samples used were varied from powdered SiC, CVD SiC and hexagonal SiC both single crystal and polycrystalline. As mention in the introduction, the most used methods for oxide scales thickness measurement was the thermo-gravimetric analysis (TGA), and the ellipsometry. In the case of TGA, the oxidation rate between the Si-face and the C-face could not be distinguished. So the oxidation rate and the activation energies derived from this method would lie in the intermediate between those of the Si-face and the C-face.

Table 3-3 shows oxidation activation energies from previous studies compared with results from our study. Because the polytypic and the anisotropy of SiC has an effect on the oxidation rate and consequently on the oxidation activation energy, we chose only the studies where hexagonal single crystal SiC was used as experimental sample, and the thickness of the formed oxide scale was measured by ellipsometry (studies that distinguished between that on the Si-face and the C-face) for comparison.

It can be seen that the activation energy of the Si-face from our study agrees well with those of the previous studies. However, the result of the C-face is lower, compared to most of that of the previous studies. One of possible origins for these differences in activation energy is the morphology of the oxide scales. When conduct oxidation experiment at high temperature (i.e. above 1473 K) with sufficiently long oxidation time, the devitrification (crystallization) of the oxide scales will occur. The ratio of the crystalline oxide scales increases with the oxidation time and temperature. The devitrification will affect the results of thickness measurement by ellipsometry because of the change in the microstructures of the formed oxide scales. And the roughness of the crystalline oxide scale (as seen in Fig.3-2 (c)) will yield more error from measurement of the ellipsometry.

Table 3-3 : Oxidation activation energies of the Si-face and the C-face.

Reference	Si-face (kJ/mol)	C'-face (kJ/mol)	Temperature Range (°C)
12	356	197	970-1245
6	372	134-197	1200-1500
3	292	99.3	800-1100
16	298	144-308	1200-1500
13	300.9	191.9	950-1150
this study	358	85	1000-1200

For the studies on oxidation of SiC conducted using ellipsometry, generally two layers or three layers model would be applied to the measured data²¹. In two layers model, the oxide scale was thought to simply form on the SiC substrate. And in three layers model, a interface layer, which is believed to have mixed refractive index between the refractive index of SiC and that of amorphous SiO₂²². These models may yield accurate results if the oxide scales have homogeneous disposition, i.e. compose of only amorphous silica or only one phase of crystalline silica. In case where the oxide scale composed of both amorphous and crystalline silica, the ratio of each phase must be known in order to correctly interpret the ellipsometric data. And in some regions where the crystalline phase silica exist, the oxide scales divided into two layers, the upper layer composed of crystalline and the lower layer composed of amorphous scales, (these results will be shown in Chapter 4). In these cases, the simple two layers will yield only the thickness of the upper layer (the crystalline scale), so the estimated thickness would be less than the actual thickness.

For example, the interpretation of ellipsometric data, in case of simple 2 layers model. The thickness of thin film formed on the substrate can be describe using equation of phase thickness, β . The phase thickness is described as following;

$$\beta = 2 \pi d N_1 \cos \theta_1 / \lambda \quad (3)$$

d is the thickness of thin film, N_1 is the refractive index of the thin film, θ_1 is the reflected angle and λ is the wavelength of the optical beam used. From this equation, it can be seen that if the refractive index changed, the same measurement can yield different thickness of thin film. In particular, the refractive index of amorphous SiO₂ is equal to 1.46, while that of crystal SiO₂ (quartz) is equal to 1.54²³. Considering only the case of pure amorphous silica and pure quartz structure, by roughly estimating from the refractive indexes with the equation (3), the thickness calculated can be approximately 5% different.

The ratio of the regions where crystallization occurred in this study is quite low, due to the high purity of samples and oxidation environment used. However, in many other studies, contamination was not as strictly controlled. For example, many studies used alumina tube furnaces which would act as the source of contaminations. So the ratios of the crystallized regions of these studies are thought to be relatively high, compared to this study. Accordingly, it is thought to be important that the existence of the crystalline phase silica should be addressed in the analyses of ellipsometric data.

Besides the complication of measurement using ellipsometry when devitrification is involved, even in the case where ellipsometric data was interpreted precisely with consideration of the crystalline scales, the diffusion of oxidant in amorphous silica and in crystalline silica must also be considered. The diffusion rate of oxygen in cristobalite was reported lower than in amorphous silica⁴. This could be the explanation for lower oxidation activation energy found in our study which obtained from measuring the thickness of oxide scales from the regions composed of only amorphous silica, comparing to other studies which did not specify the regions where oxide scale thickness measurement would be conducted. Moreover, if this is the case, the lack of differences in the activation energy of the Si-face may imply that the devitrification rate of the oxide scale on the C-face is more progressed than on the Si-face.

3.6 Summary

The thermally formed oxide scales on single crystal hexagonal silicon carbide were investigated using OM, SEM and TEM. Crystalline oxide scales were found randomly distributed on both the Si-face and the C-face of the oxidized samples. FIB micro-sampling technique was applied to prepare samples for thickness measurement of the thermally formed oxide scales from the amorphous silica regions for accurate thicknesses. The thickness of the oxide scales were measured directly using SEM and

TEM. The oxidation activation energy of the oxidation of the amorphous silica was found to be 358 kJ/mol for the Si-face and 85 kJ/mol for the C-face.

Reference

- ¹ P. F. Tortorelli and K. L. More, *J. Am. Ceram. Soc.*, 86 (2003) 1249.
- ² E. A. Ray, J. Rozen, S. Dhar, L. C. Feldman and J. R. Williams, *J. Appl. Phys.*, 103 (2008) 023522
- ³ L. U. J. T. Ogbuji and M. Singh, *J. Mater. Res.*, 10 (1995) 3232.
- ⁴ C. E. Ramberg and W. L. Worrell, *J. Am. Ceram. Soc.*, 84 (2001) 2607.
- ⁵ L. Muehlhoff, M. J. Bozack, W. J. Choyke and J. T. Yates, Jr., *J. Appl. Phys.*, 60 (1986) 2558.
- ⁶ J. A. Costello and R.E. Tressler, *J. Am. Ceram. Soc.*, 69 (1986) 674.
- ⁷ P. J. Jorgensen, M. E. Wadsworth and I. B. Cutler, *J. Am. Ceram. Soc.*, 42 (1959) 613.
- ⁸ Z. Zheng, R. E. Tressler and K. E. Spear, *J. Electrochem. Soc.*, 137 (1990) 854.
- ⁹ B. E. Deal and A. S. Grove, *J. App. Phys.*, 36 (1965) 3770.
- ¹⁰ B. Chayasombat, T. Kato, T. Hirayama, T. Tokunaga, K. Sasaki and K. Kuroda, *J. Elec. Micros.* (2010) doi:10.1093/jmicro/dfq039.
- ¹¹ E. Opila, *J. Am. Ceram. Soc.*, 78 (1995) 1107.
- ¹² R. C. A. Harris, *J. Am. Ceram. Soc.*, 58 (1975) 7.
- ¹³ Y. Song, S. Dhar and L. C. Feldman, *J. App. Phys.*, 95 (2004) 4953.
- ¹⁴ B. E. Deal and A. S. Grove, *J. App. Phys.*, 36 (1965) 3770.
- ¹⁵ P. J. Jorgensen, M. E. Wadsworth and I. B. Cutler, *J. Am. Ceram. Soc.*, 42 (1959) 613.
- ¹⁶ J. Li, P. Eveno, A. M. Huntz, *Werkstoffe und Korrosion*, 41 (1990) 716.
- ¹⁷ J. Rodriguez-Viejo, F. Sibieude and M. T. Clavaguera- Mora, *J. Euro. Ceram. Soc.* 19 (1994) 167.
- ¹⁸ D. Das, J. Farjas and P. Roura, *J. Am. Ceram. Soc.*, 87 (2004) 1301.
- ¹⁹ Z. Zheng, R. E. Tressler and K. E. Spear, *J. Electrochem. Soc.*, 137 (1990) 854.
- ²⁰ T. Narushima, T. Goto and T. Hirai, *J. Am. Ceram. Soc.*, 72 (1989) 1386.
- ²¹ T. Yamamoto, Y. Hijikata, H. Yaguchi and S. Yoshida, *Jpn. J. App. Phys.*, 47 (2008) 7803.
- ²² K. Kakubari, R. Kuboki, Y. Hijikata, H. Yaguchi and S. Yoshida, *Mater. Sci. Forum*, 527-529 (2006) 1031.
- ²³ *Handbook of Optics*, 3rd edition, Vol. 4. McGraw-Hill 2009

Chapter 4: Microstructures of Oxide Scales on Silicon Carbide

4.1 Introduction

Protective silica oxide scales are known to form on SiC at high temperature in an environment with sufficient oxygen partial pressure¹. The formed oxide scales were reported as amorphous silica and various forms of crystalline silica. The formation of crystalline silica is not desired in most of usages of SiC. In case of using SiC as high temperature structural material, the formation of crystalline silica will induce cracks to the protective oxide scales and these cracks will act like shortcuts for oxygen transportation. So that the cracks will induce further oxidation comparing to the region where the surface of SiC is protected by the densely formed oxide scales. And in the case where SiC is used as electrical devices, the crystalline oxide scales will have affect on the electrical properties of insulate oxide layer. This will have a major effect on the performance of the device. As seen in Chapter 3, the crystalline phase of oxide scales were found in various samples. The formation of the crystalline phase is random in sizes and location. Moreover obvious relationship between oxidation time and temperature with the crystalline phase formation was not observed in Chapter 3 of this study.

Therefore, it is important to understand factors that have influence on the crystallization of the silica oxide scales. Also, a close study on the microstructures of oxide scales will lead to a deeper understanding of crystallization processes. This understanding of the process may lead to the control and restriction over the crystallization of the silica scales.

4.2 Previous Studies on Microstructures of Oxide Scales on Silicon Carbide

Many studies had reported the finding of crystalline oxide scale in case of the oxidation at relatively high temperature (above 1473 K) and sufficiently long oxidation

time^{2, 3, 4, 5, 6, 7}. The most reported crystalline phase silica was alpha and beta phase of cristobalite. Some studies also reported the finding of small amount of tridymite^{4, 6}. Table 4-1 shows summary of studies reported the finding of phases of crystalline silica scales, with methods used to characterize and the range of the oxidation temperature. The often reported cristobalite was mostly found as a thin disk-shaped in the amorphous silica matrix⁷. These disk-shaped is referred to in many studies as spherulitic or rosettes cristobalite. As the oxidation advanced, fall-offs of these spherulitic crystals were reported⁵. These fall-offs will lead to the exposure of new un-oxidized surfaces of SiC, then the oxidation of SiC in that region will be accelerated and oxidized further compared to the surrounding regions. Therefore, in the case where SiC is used in high temperature environment with repeated heating, annealing and cooling processes, the formation of these spherulitic crystalline oxide scales must seriously be considered.

4.3 Background and Objective

Previously, we attempted to characterize the crystalline oxide scales by using X-ray diffraction (XRD). XRD had been used in many studies as a tool for characterizing the morphology of crystalline silica. Figure 4-1 (a) and (b) show XRD θ - 2θ scans of single crystal 6H-SiC samples before and after oxidation at 1473 K for 25 hours, respectively. Due to very high intensities of peaks of (006) and (0012) of 6H-SiC, the figures are captured from low intensity regions; full intensities of (006) and (0012) are not shown. The XRD result of the sample before oxidation shows peaks that are identical to the peaks of the sample after oxidation. Peaks from substrate can be indicated as shown in (a). The positions of the peaks from 6H-SiC substrate, shown in Fig.4-1 (a) are overlapping with the peaks of (110) [$2\theta=17.6^\circ$], (311) [$2\theta=41.8^\circ$], (411) [$2\theta=54.6^\circ$], and (511) [$2\theta=68.16^\circ$] of cubic cristobalite and (201) [$2\theta=11.72^\circ$], (402) [$2\theta=23.52^\circ$], (-604) [$2\theta=29.54^\circ$] and (136) [$2\theta=61.26^\circ$] of monoclinic tridymite. Both cristobalite and tridymite are often reported crystalline silica polymorphs found in oxidation of SiC^{8, 9}. The overlapping positions of the peaks make identifying the crystalline oxide scale formed on single crystal 6H-SiC using XRD θ - 2θ scan nearly impossible. Moreover, the

peaks of (101), (102) and (201) [$\theta = 21.95^\circ$, 31.37° and 38.38° , respectively] which were identified later from TEM observation are not presented in (b). Furthermore, existence of cubic cristobalite align in (110) and (311) are also confirmed by SADP, but the position of peaks are overlapping with peaks from the 6H-SiC substrates.

As observed in XRD results, the characterization of crystalline oxide scales using XRD was not possible in the case of this study. Accordingly, in order to accurately characterize the crystalline silica scales in the case of this study, the characterization has to be done by TEM. In this study, we use OM, SEM, and TEM together with X-ray energy dispersive spectroscopy (XEDS) installed in TEM, to characterize the microstructures of the thermally formed crystalline oxide scale on single crystal SiC. Also, the application of FIB microsampling enabled the TEM specimen preparation of the specified crystallized regions. The objective of this study is to understand more on the microstructures of the crystalline oxide scales. A model for crystallization process of the oxide scale were built base on TEM observations of the crystalline oxide scales in various stages.

Table 4-1 : Studies on crystallization of oxide scales on SiC.

Reference	Oxidation Temperature	Type of SiC	Method	Phase
Ogbuji (1995)	1373-1673K	Reaction formed SiC	XRD	α -cristobalite, tridymite
Fox (1998)	1473-1873K	CVD beta-SiC	XRD	cristobalite and tridymite
Ogbuji (1997)	1573K	CVD SiC	XRD	cristobalite
Li (1990)	1323-1673K	Single crystal and polycrystalline SiC	XRD	cristobalite
Costello (1981)	1473-1773K	Sintered SiC	XRD	cristobalite
Heuer (1980)	1673K	Single crystal SiC	XRD	cristobalite

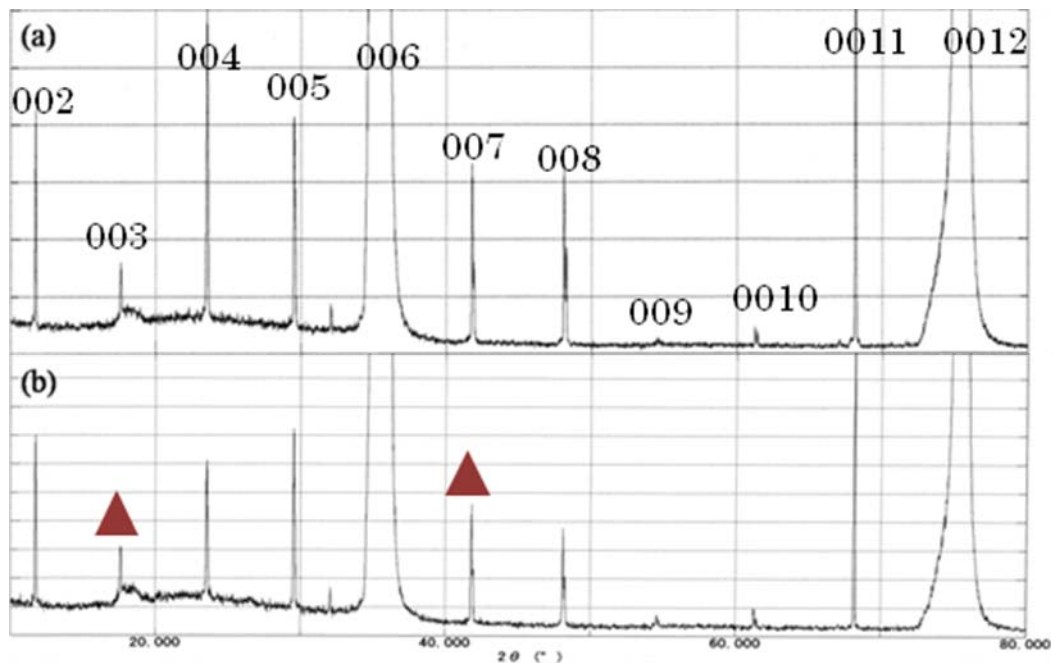


Figure 4-1 : XRD results of (a) 6H-SiC substrate before oxidation and (b) the Si-face of 6H-SiC after oxidized at 1473K for 25h in dry oxygen.

4.4 Experimental Procedures

Single crystal 6H-SiC wafers (n-type) provided by Cree Inc. was used. The wafer was cut into 10x10 mm² size. The samples were rinsed in acetone and then successively cleaned ultrasonically in ethanol. The cleaned samples were then loaded onto a quartz sample holder and put into the furnace. Two types of electrical furnace were used in this study, a quartz tube furnace (for oxidation in dry oxygen with high purity environment) which is the same furnace that used in Chapter 3, and a Super Burn electrical furnace made by Motoyama Company (for oxidation in air with relatively higher contamination density compared to the quartz tube furnace) for comparative reason.

The usage of a quartz tube furnace in case of dry oxidation was because of effects of contaminations from alumina furnace tube on the oxidation of silicon carbide which was reported by E. Opila¹⁰. Accordingly, the level of contaminations in experimental settings had been carefully controlled in this case. The SiC sample used in dry oxidation study was high purity single crystal 6H-SiC wafer and the tube of the furnace used for oxidation experiment was high quality quartz tube with quartz sample holder.

Comparative experiments of oxidation were conducted in air at ambient pressure. Heating and cooling rates was 5 K/min. For the dry oxidation experiments, pure dry oxygen was flown at flowing rate of approximate 100cc/min for 2 h prior to the oxidation to ensure pure dry oxygen environment. The furnace system was then heated up with temperature gradient of 10 degrees/min. The oxidation condition was 1473K with oxidation time from 9 to 25 h in flowing dry oxygen at 1 atm. Moreover, comparative experiments of the oxidation of samples with have larger surface roughness were conducted. The samples with large surface roughness were prepared by polishing both the Si-face and the C-face of the 6H-SiC successively with 9 micrometers and 4 micrometers diameter diamond powder.

The oxidized samples were then observed using OM. The regions with glossy color patterns, which were observed randomly scattered on the surface of the samples after thermal oxidation, were identified and marked using silver paste, and then platinum was deposited on the surfaces of the samples to prevent electrical charging during TEM specimen preparation. TEM specimens were prepared by focused ion beam (FIB) micro-sampling technique using a HITACHI NB-5000 FIB-SEM system at an accelerate voltage 5-40 kV. Carbon and tungsten were deposited on the surfaces of the samples in the FIB system prior to the TEM specimen preparation in order to protect the surfaces of the specimens of the damage by FIB fabrication. The cross-sectional TEM specimens were observed in a JEM-2010 at an accelerating voltage of 200 kV. The crystalline phase of the oxide scale was highly sensitive to the electron beam irradiation. Accordingly TEM low dose observation must be applied. The low dose observation technique is an observation technique where only approximate 5% of dose of electron beam is used for observation, compared to the normal observation. XEDS spectrums and mapping was measured in a Topcon-002B at an accelerating voltage of 200 kV.

4.5 Results

4.5.1 Oxidation in Dry Oxygen

Figure 4-2 shows OM image of the Si-face of the samples after oxidation at 1473 K for (a) 9 h (b) 16 h and (c) 25 h, respectively. Fig. 4-2 also shows OM images of the C-face of the samples after oxidation at 1473K for (d) 9 h, (e) 16 h and (f) 25 h, respectively. The differences in color of the oxidized samples with different oxidation time were due to the differences of the thickness of the formed oxide scale. Patterns with different color from the majority of the oxide scales are observed randomly scattered on the surface of the formed oxide scales of the samples of all oxidation time. The shape of the formed patterns was mostly round with rough edges. These spherical patterns are also

random in size for each oxidation times. The sizes of the formed spherical patterns varied from a few micrometers to over a hundred micrometers in diameter. Differences between the formation of the patterns of the Si-face and the C-face were not observed. For the sample oxidized for 25 h (Fig.4-2 (c)), a scratch which existed on the surface of the sample prior to the thermal oxidation, was observed. However, the spherical patterns formed in the vicinity of the scratch were not selectively formed over the scratch.

Figure 4-3 (a) shows a high magnification OM image of one of the patterns formed on the sample oxidized for 9 h. The diameter of the pattern is approximately 50 micrometer in size. Fig. 4-3 (b) shows cross-sectional TEM image of the TEM specimen took from region A indicated in Fig. 4-3 (a). In this region, the oxide scale was composed of both crystalline and amorphous silica scales. The thickness of the oxide scale in this region is not uniform. The cross-sectional TEM image of the specimen from region B, the region close to the edge of the spherical pattern, is shown in Fig. 4-3 (c). In this region, the oxide scale composed of only amorphous silica. The thickness of the oxide scale is also not uniform in this region. Round-shape amorphous with darker contrast were observed in the amorphous oxide layer. From the results of XEDS elemental mapping, as shown in Fig. 4-3 (d)-(i), traces of calcium were existed in these round-shaped amorphous.

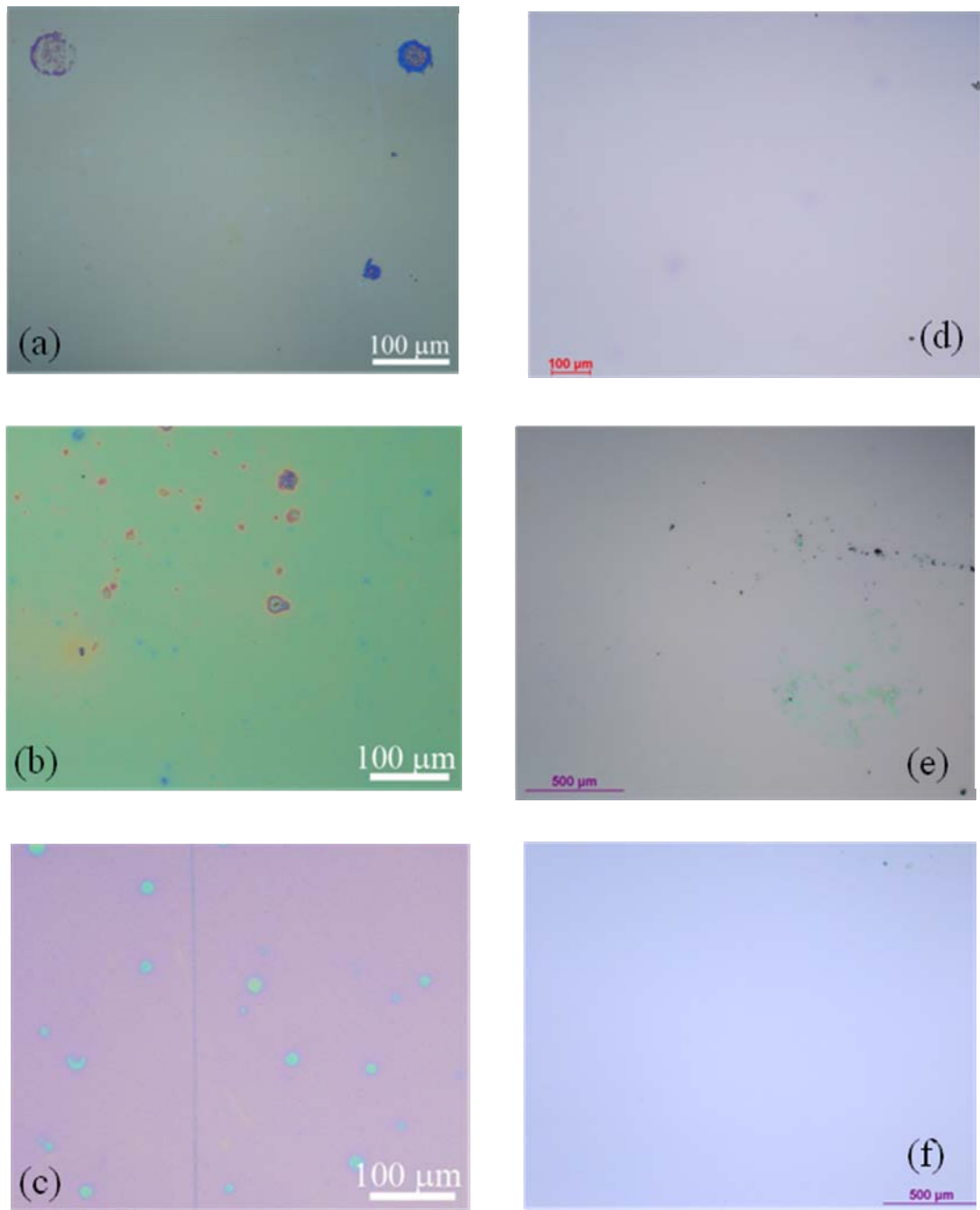


Figure 4-2 : OM image of the Si-face of samples oxidized at 1473K for (a) 9h, (b) 16h and (c) 25h and the C-face of samples oxidized at 1473K for (d) 9h, (e) 16h and (f) 25h, respectively.

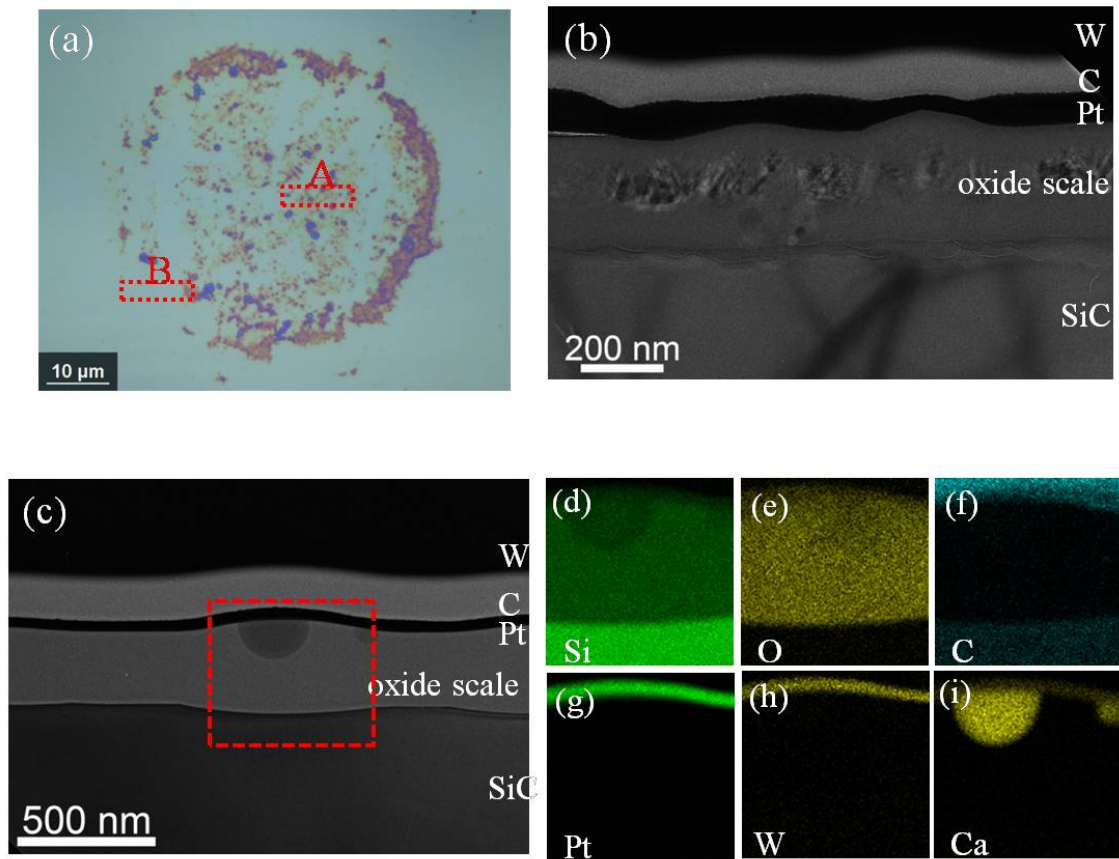


Figure 4-3 : (a) OM image of the sample oxidized for 9h (b) cross-sectional TEM image of region A and (c) cross-sectional TEM image of region B. (d)-(i) EDS elemental mapping of the region indicated by a broken-line square in (c).

Figure 4-4 (a) shows OM image of the patterns formed on the sample oxidized for 16 h. The diameter of the pattern is approximately 20 micrometers in size. Fig. 4-4 (b) shows cross-sectional TEM image of the TEM specimen taken from the pattern region, the region A indicated in Fig. 4-4 (a). The oxide scale was composed of both amorphous and crystalline silica. Fig. 4-4 (c) show a SADP taken from the region indicated by a broken-line circle in Fig. 4-4 (b). From the SADP, the crystalline oxide scale was identified as polycrystalline tetragonal cristobalite (alpha cristobalite). Fig. 4-4 (d) shows cross-sectional TEM image from the surrounding region of the pattern. In this surrounding region, the oxide scale is uniformly formed and composed of only amorphous silica.

Figure 4-5 (a) shows OM image of the sample oxidized for 25 h. The pattern formed on the surface of the sample was approximately 70 micrometers in size. Fig.4-5 (b) shows cross-sectional TEM image from the specimen taken from the center of the pattern, as indicated by an arrow in Fig. 4-5 (a). The oxide scale in this region was very roughly formed. The thickest part of the scale was about twice as thick compared to the surroundings, shown in the right side of the image. Voids were observed in the crystalline scale close to the surface of the cross-sectional TEM specimen. Fig. 4-5 (c) shows schematic of the formed oxide scale. The oxide scale was crystalline phase from the surface to the interface between oxide scale/SiC in some regions. However, in some regions, the oxide scale was divided into two layers with crystalline phase on the upper and amorphous phase on the lower layer. This crystalline phase oxide scale was surrounded by relatively thin and uniform amorphous phase oxide scale. Fig.4-6 and 4-7 (a)-(f) show result of XEDS elemental mapping from the regions indicated by each broken line squares in Fig. 4-5 (b). Traces of calcium were found in the crystalline phase silica. In the regions where XEDS results show traces of calcium, it can be roughly estimate that, in those regions, approximately 0.1% of calcium existed. Because the amount of element detected, depends on various conditions, such as thickness of the TEM specimen, time and dose of electron beam used, or type of the samples. Therefore, the precise amount of calcium cannot be concluded base on existing data.

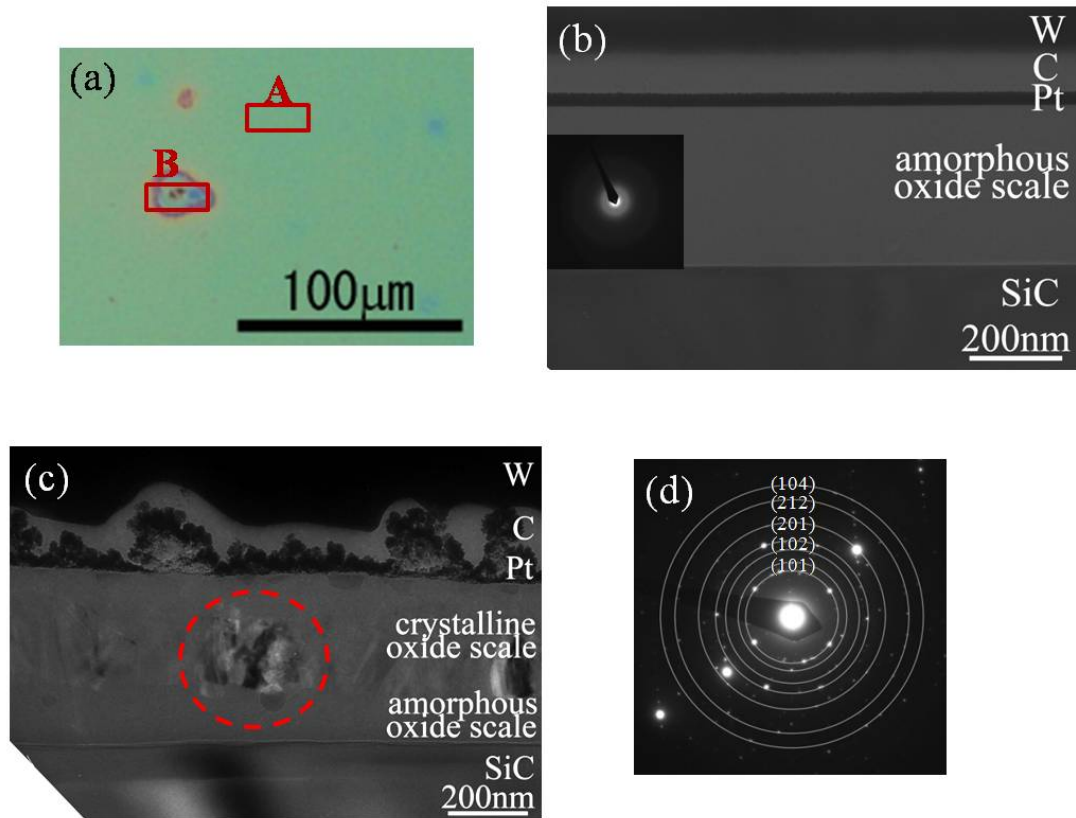


Figure 4-4 : (a) OM image of the sample oxidized for 16h, (b) cross-sectional TEM image of region A, (c) cross-sectional TEM image of region B and (d) SADP of the circled region in (c).

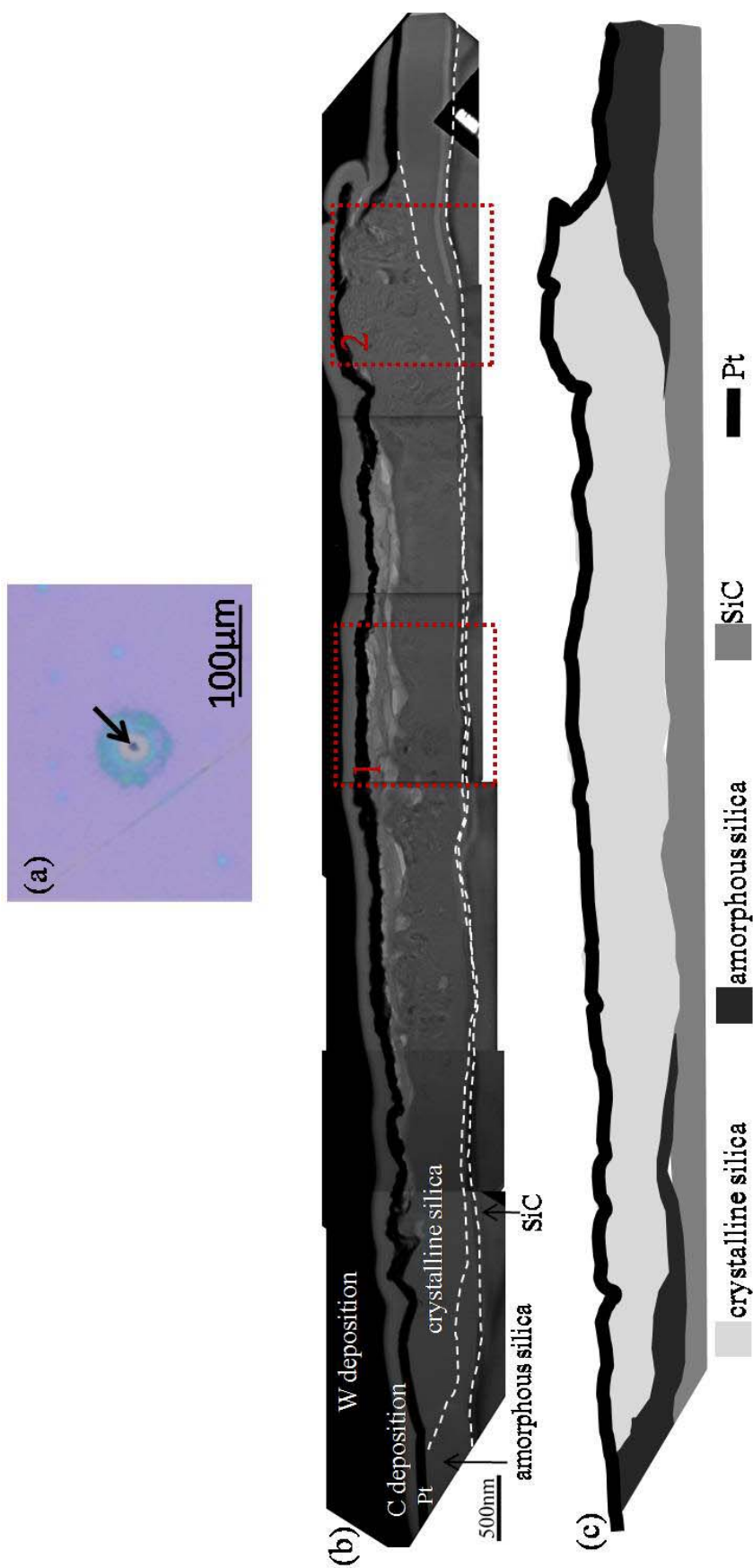


Figure 4-5 : (a) OM image of the sample oxidized for 25h (b) cross-sectional TEM image of the center of the pattern indicated in (a) and (c) schematic of (b)

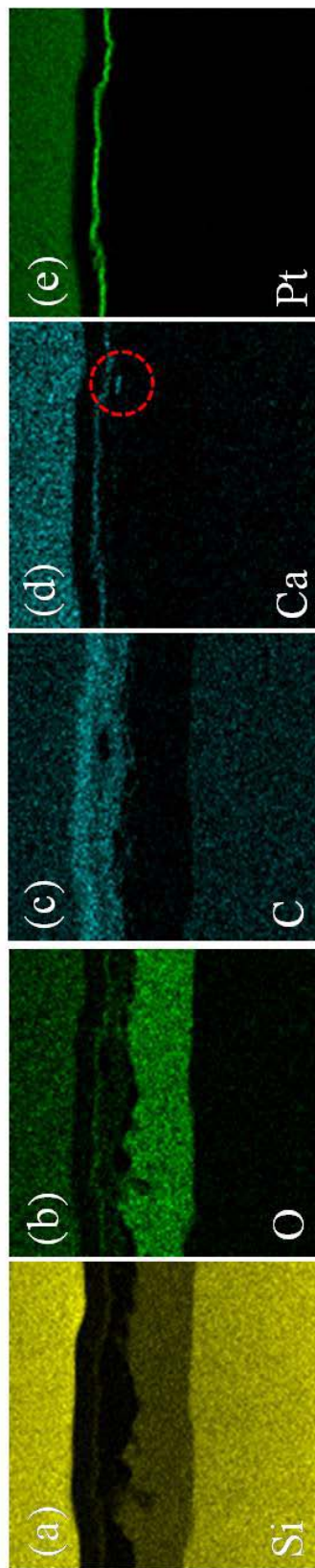


Figure 4-6 : (a)-(e) EDS elemental mapping from region 1 indicated in Fig. 4-5 (b) of Si, O, C, Ca and Pt, respectively.

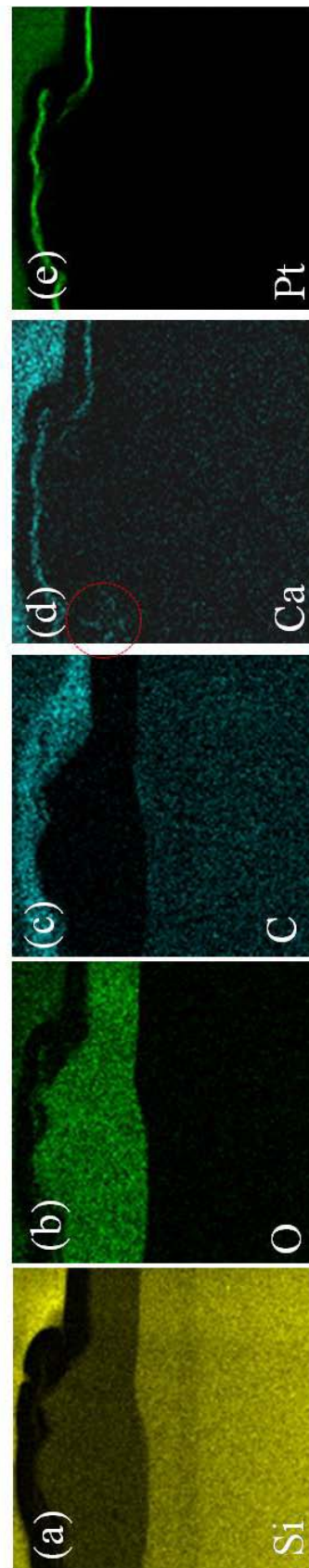


Figure 4-7 : (a)-(e) EDS elemental mapping from region 2 indicated in Fig. 4-5 (b) of Si, O, C, Ca and Pt, respectively.

4.5.2 Oxidation of Samples with High Surface Roughness

Figure 4-8 shows OM images of the Si-face and the C-face of the samples with company-finished surfaces and surfaces after polished with diamond powder, both before and after oxidation. The surfaces of the samples after polished by diamond powder were extremely rough. Scratches can be observed distributed all over the surfaces. After oxidation, glossy color patterns and spherical patterns were formed over sample surfaces. The density of the patterns formed was significantly higher in the sample with higher surface roughness compared to company-finished surface samples. Fig. 4-9 shows low magnification OM image of the C-face of the sample polished with diamond powder after oxidation at 1473K for 20h. Spherical patterns were observed distributed all over the surface of the sample. However, some part of the patterns are observed distributed along the polishing flaw as observed as a curved line in Fig.4-9.

Figure 4-10 show (a) OM image of the Si-face of sample oxidized for 20h with region of TEM specimen indicated by a broken-line square, (b) cross-section TEM observation, and (c)-(e) SADP correspond to each circled regions indicated in Fig. 4-10(b). The oxide scale in this region clearly divided into two layers. The upper layer is polycrystalline, the lower layer composed of amorphous phase silica. From SADP characterization in Fig. 4-10(c), the crystalline phase oxide scale is identified as tetragonal cristobalite with [011] align along the oxide scale growth direction. The surface of the crystalline phase silica is observed to be rough, while the interface between the crystalline phase and amorphous phase silica is relatively flat.

Figure 4-11 show (a) OM image of the C-face of sample oxidized for 20h with region of TEM specimen indicated by broken-line squares, (b) cross-section TEM observation of the region A with SADP inset, and (c) cross-section TEM observation of the region B with SADP from circled region. The spherical patterns of this sample are about 15 micrometers in diameter. From the cross-sectional TEM observation of region A, the oxide scale from the region without patterns is composed of only amorphous silica.

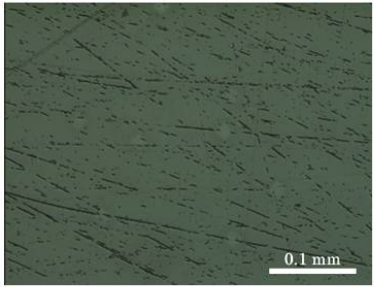
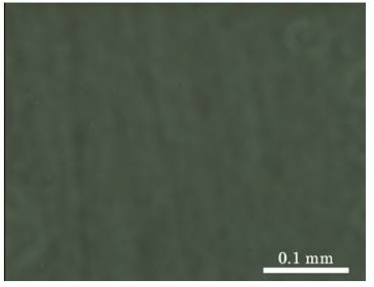
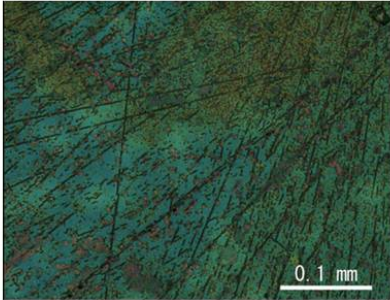
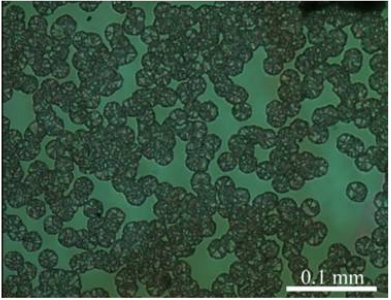


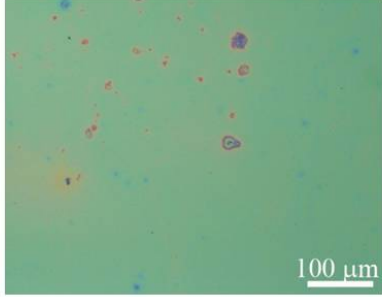
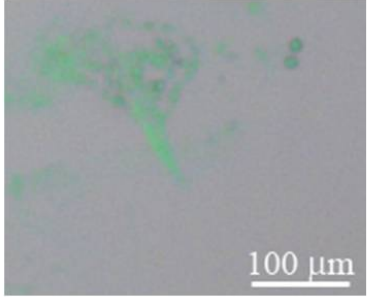
	Si-terminated face	C-terminated face
Diamond powder polishing (before oxidation)		
Diamond powder polishing (1473K, 20h in dry oxygen)		
Company finished surface (before oxidation)		
Company finished surface (1473K, 16h in dry oxygen)		

Figure 4-8 : OM images of Si-face and C-face of samples with polished by diamond powder and company- finished before and after oxidation.

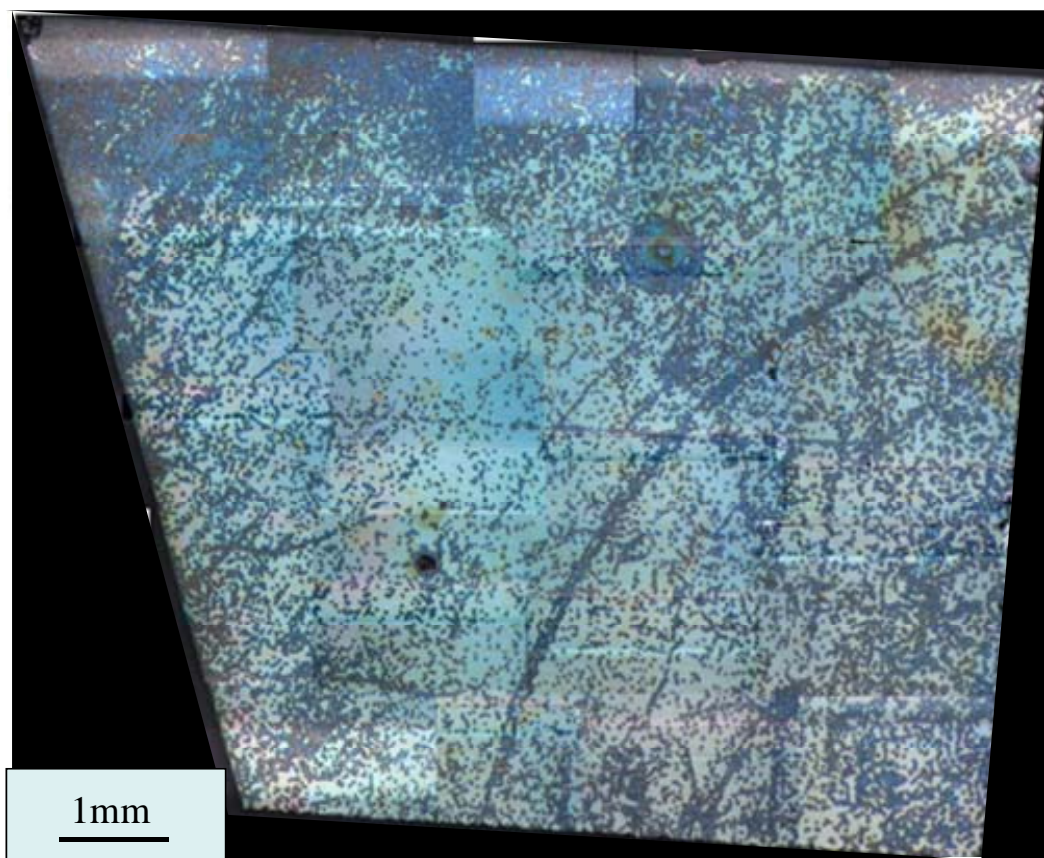


Figure 4-9 : OM images of C-face of sample polished with diamond powder after oxidation in dry oxygen for 20h.

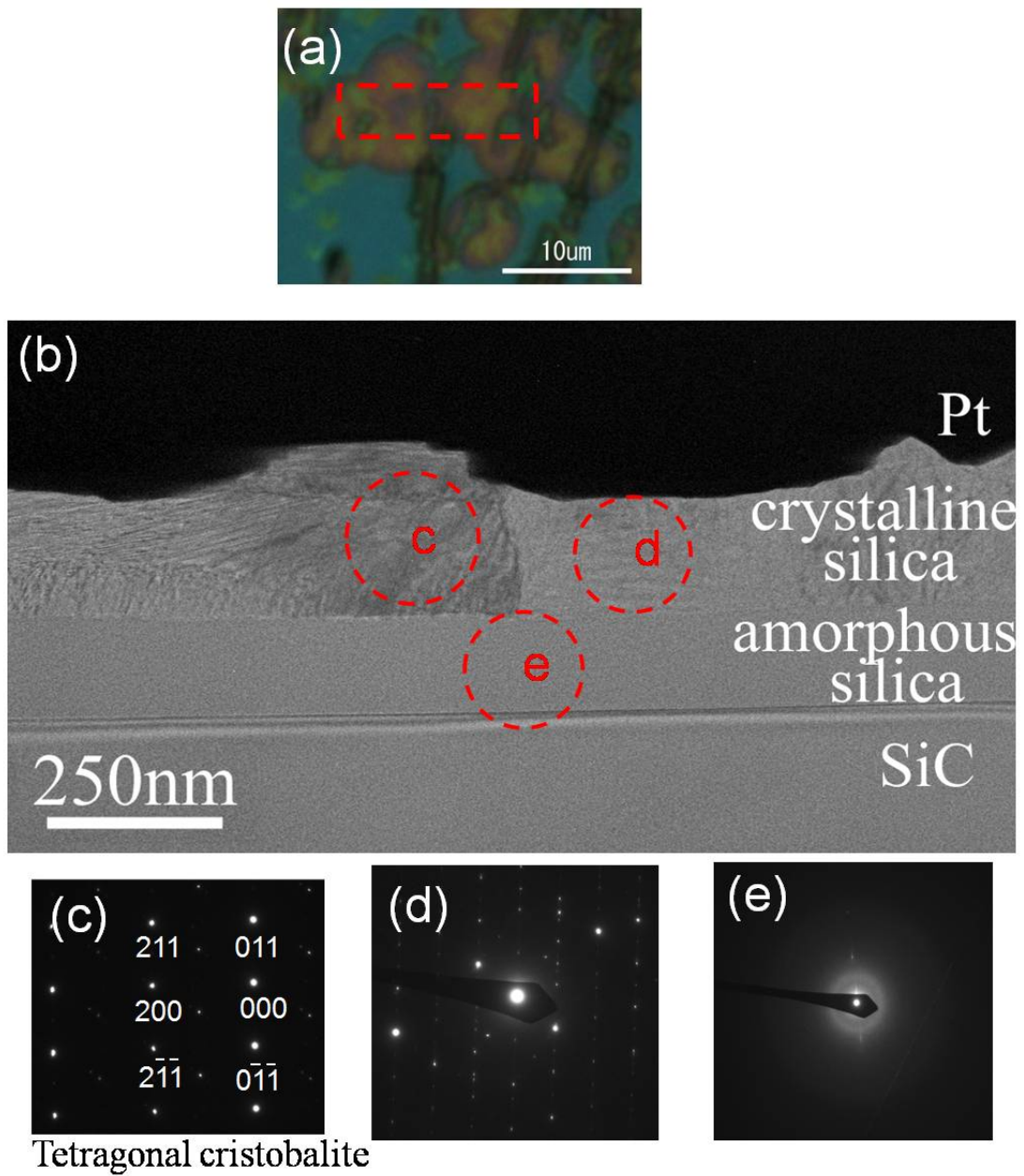


Figure 4-10 : (a) OM image of the Si-face of the sample oxidized for 20h (b) cross-sectional TEM image of region indicated in (a), (c)-(e) SADP of each region indicated by broken line circles in (b).

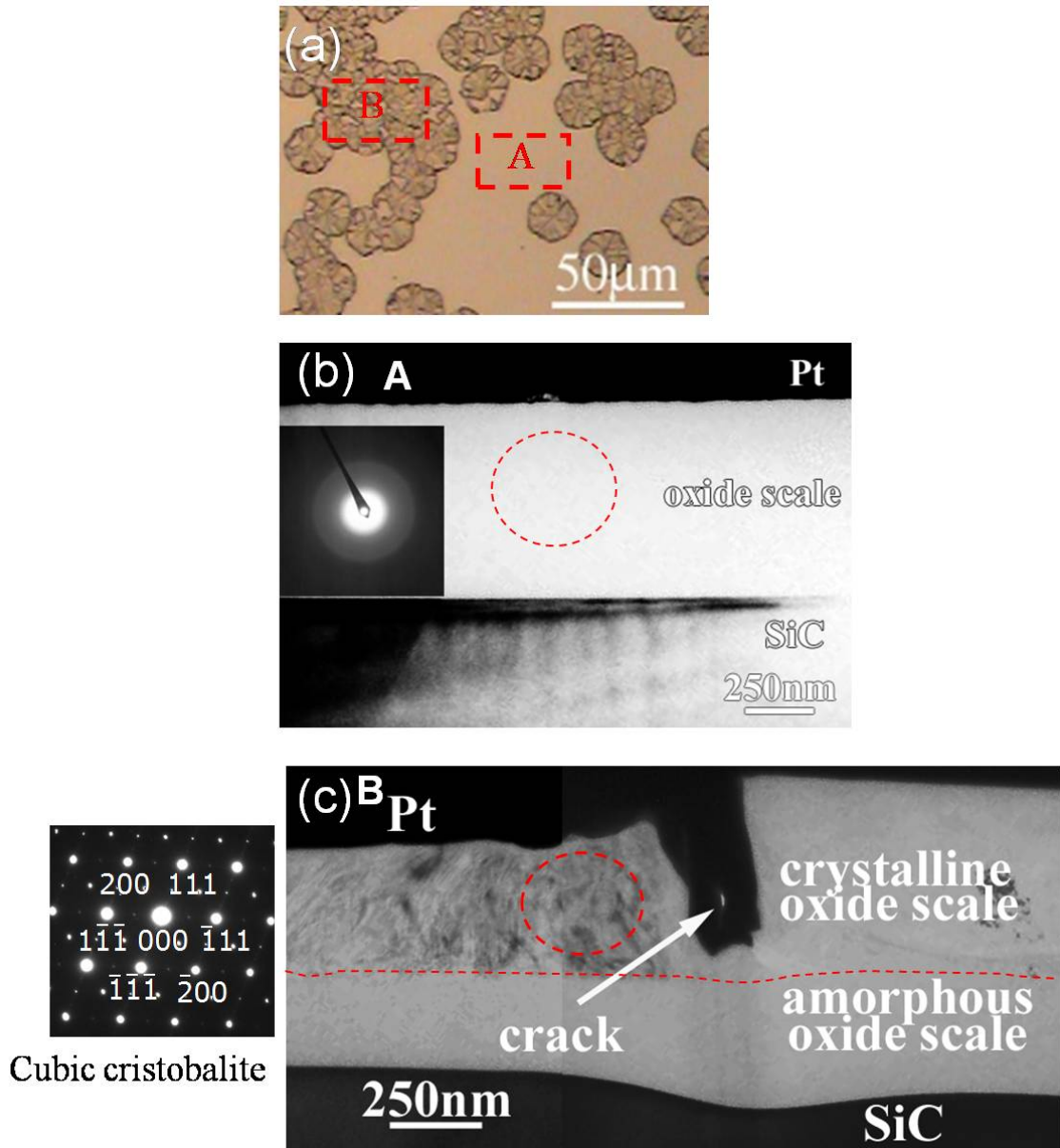


Figure 4-11 : (a) OM image of the C-face of the sample oxidized for 20h (b) cross-sectional TEM image of region A indicated in (a), (c) cross-sectional TEM image of region B.

The amorphous silica is uniformly formed. From Fig. 4-11 (c), the oxide scales in this region divided into two layers with crystalline phase on the upper layer and amorphous phase on the lower layer. The SADP characterization identified the crystalline phase oxide scale as cubic cristobalite with [311] align along the growth direction of the oxide scale. A crack in the formed oxide scale is observed in Fig. 4-11 (c). The oxidation is observed to progress further, compared to the surrounding region, underneath the crack. Fig. 4-12 and 4-13 also show cross-sectional TEM images from spherical pattern region from the C-face of the sample oxidized for 20 h. In both Fig. 4-12 and 4-13, the oxide scale is not divided into two layers, but composed of only crystalline silica. The oxide scales from both regions were identified by SADP as cubic cristobalite. Twinning of the crystalline oxide scale is observed in Fig.4-13.

4.5.3 Oxidation in Air

Oxidation experiment of the sample with company finished surface was conducted for comparison with the oxidation in pure dry oxygen. Fig. 4-14 shows OM images of (a) the Si-face and (b) the C-face of the oxidized sample. The oxidation condition was 16h at 1473K in still air. The formation of the spherical patterns was not observed to be significantly different from the oxidation in dry oxygen. Fig. 4-15 shows (a) OM image of one of the patterns formed on the Si-face of the sample, (b)-(d) cross-sectional TEM image corresponded to region A, B and C in Fig. 4-15(a), respectively. The oxide scale in the center of the pattern (region A) was composed of crystalline phase silica, while the surrounding regions (region B and C) were composed of amorphous phase silica. The surrounding amorphous phase oxide scales are roughly formed with non-uniformed thickness.

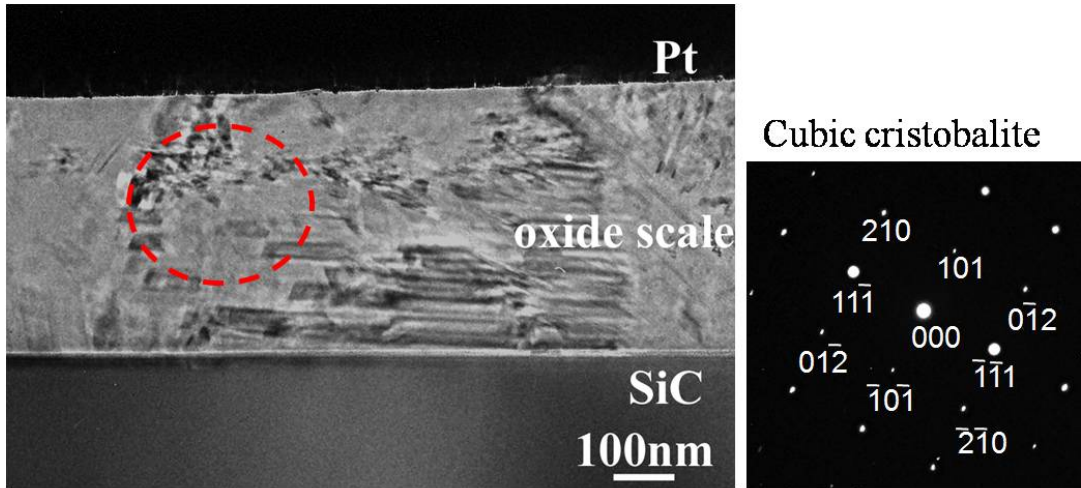


Figure 4-12 : Cross-sectional TEM image of the C-face of the sample oxidized for 20h with SADP corresponded to circled region.

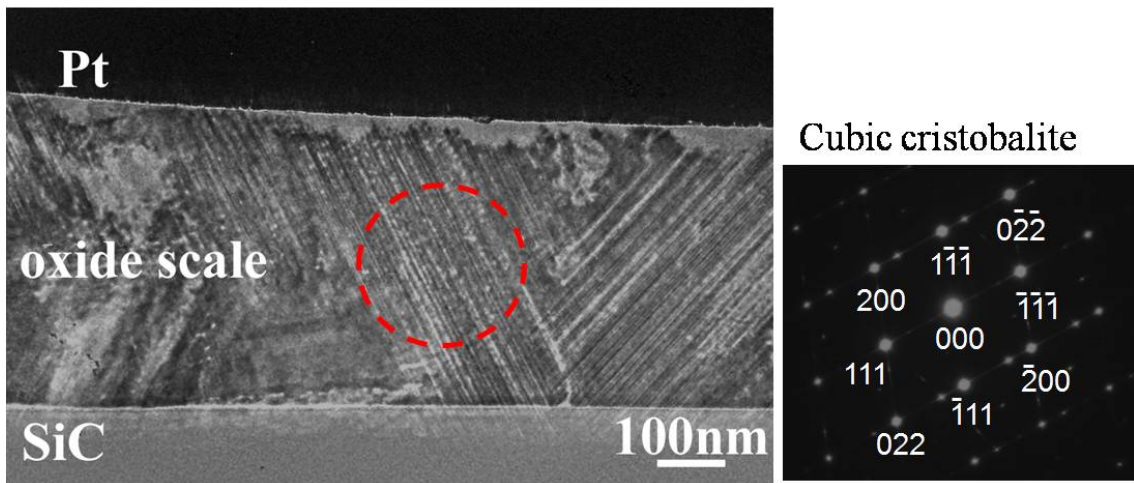


Figure 4-13 : Cross-sectional TEM image of the C-face of the sample oxidized for 20h with SADP corresponded to circled region.

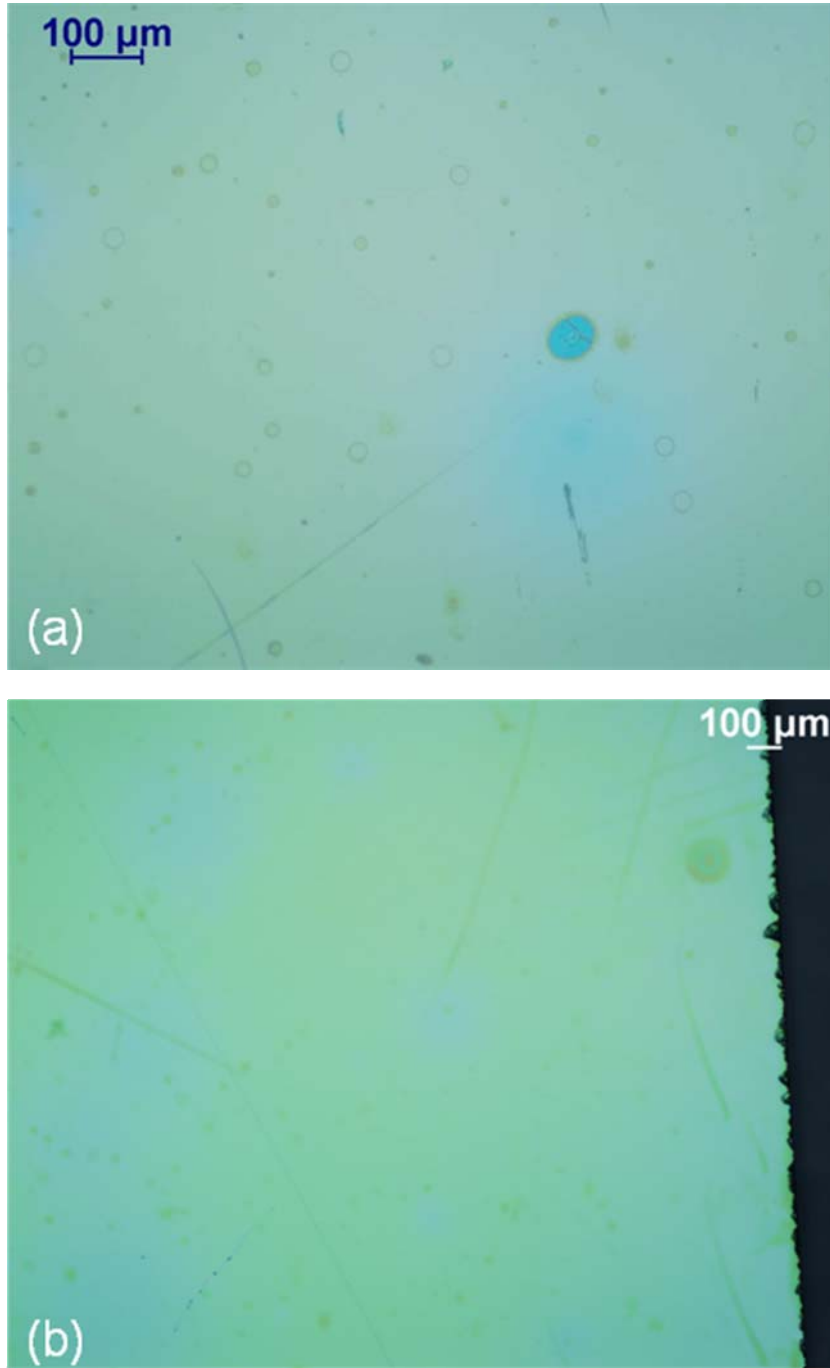


Figure 4-14 : OM images of (a) Si-face and (b) C-face of the sample oxidized at 1473K in air for 20h.

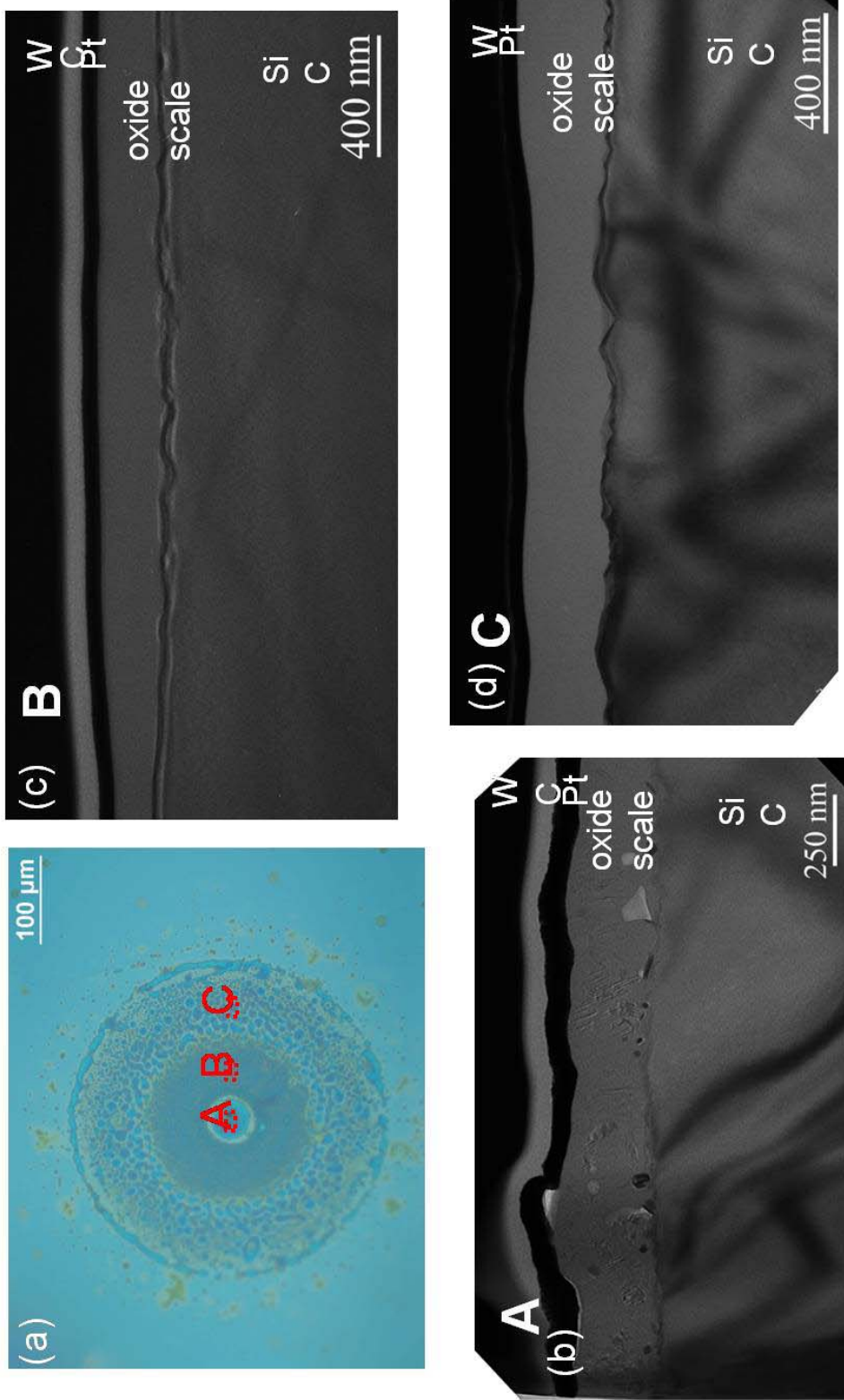


Figure 4-15 : (a) OM image of the sample oxidized for 16h in air (b)-(d) cross-sectional TEM image of region A, B and C, respectively.

4.6 Discussion

Many studies have reported the morphology of the formed crystalline oxide scales as radialite, a disk-shaped crystalline with characteristic dendritic cracks^{3, 11}. These cracks which formed in the radialites were said to be caused by the volume contraction due to the transformation from beta-cristobalite to alpha-cristobalite, the transformation from cubical to tetragonal structure which occurs at relatively low temperature, during the cooling process¹². In our study, from the result of the SADP identification as shown in Fig. 4-4 (d) confirmed the existence of alpha phase cristobalite, so the crystalline phase silica was believed to have undergone the phase transformation from beta phase to alpha phase in this region. However, the said characteristic cracks were not found in the morphology of the crystalline oxide scales found in this sample.

As the condition of experiments in this study conducted in the relatively low temperature (1473 K) for crystallization of silica and relatively for short oxidation time (less than 25 h), so the crystallization of the oxide scales in this study was believed to be at the early stage. The lack of the characteristic cracks, as mentioned earlier, may be due to the initial stage of the crystallization of this study. Pressure et al. reported that at initial stage of crystallization, the characteristic hexagonal shape crystalline silica was found in the experiment conducted at high temperature (1673 K) and longer oxidation time (28 h)⁹. However, despite the early stage of the crystallization of this study, the formed crystalline oxide scales were not observed as hexagonal shaped, but rather round shaped with rough edges, as shown in Fig. 1 (a)-(c). It has been discussed in many studies that, the nucleation of the crystalline silica is likely to form at the inhomogeneous of the surface of sample, such as over the surface scratches or around the edges of the sample^{9, 13}. But our results show that the crystallization occurred randomly, and did not selectively concentrate around the edges of the samples, and as shown in Fig. 1 (c) where there was a scratch existed prior to the oxidation, however, the crystallization did not centered over the scratch.

The oxidation temperature, oxidation time, additives (especially in case of sintered silicon carbide), impurities and surface morphology are believed to be the influencing factors for the crystallization of the amorphous silica¹¹. As from our results, the crystallization was not formed over the scratch, however, traces of calcium were found in the crystalline oxide scale. Therefore, it is believed that impurities, calcium in this case, have stronger influence on the nucleation of the crystallization than the surface morphology. A study by Frischat reported that the diffusion of calcium in silica glass is higher than the diffusion of oxygen at the same temperature¹⁴. In this study, it was found that the calcium contamination was locally concentrated in regions where crystalline oxide scales existed. Considering the concentration of calcium and the diffusion rate reported for calcium in silica glass, it is thought that the calcium contamination was in the SiC sample as aggregations or highly concentrated on the surface of the sample prior to the thermal oxidation, possibly as a form of contaminations. This agrees well with a study made by Bruckner which stated that the concentration of the contamination must be sufficient in order for it to become the crystallization center of the vitreous silica¹⁵. However, the origin of the calcium contamination found in our study still remains unclear at this point.

From comparative studies of oxidation in air and oxidation of samples with high surface roughness, it was found that the change of oxidation environment have significantly lower influence on the crystallization of the oxide scales than the surface of the sample before oxidation. The surface with higher roughness, likely with more contamination on the surface, was observed to crystallize significantly more. Moreover, it was observed that the grain size of the crystalline phase silica is greater in the sample with higher surface roughness. From the observation of where crystalline phase oxide scales divided into two layers, it could be interpreted that the crystalline scale grows much faster laterally than into the bulk. The lateral growth rate can be roughly estimated to be at least 30 times faster than the growth rate into the bulk. The characteristic dendritic crack was observed in the sample with high surface roughness. So it is believed that the crystallization progress further more in this case. Accordingly, from the

experimental results, it shows that the surface roughness and/or the contamination level of the sample before oxidation greatly affect the crystallization of the oxide scales. The result in this study agrees well with the study of Opila in 1999¹⁶ who observed that the effect of impurities is much stronger than water vapor in oxidation atmosphere.

From the observation results of various stages of crystallization, the crystallization process was modeled as shown in schematics in Fig. 4-16. The crystallization was believed to occur followed the following steps; the firstly formed oxide scale was amorphous phase silica. It covered densely all over the surfaces of SiC and the thickness of the formed oxide scale at this stage is uniformed. Regions with high density of contamination (calcium in case of this study) existed in the amorphous oxide scale (or possibly over the surface). The nucleation of the crystallization starts at the region with high density of contamination, because the impurity is believed to decrease of average chain length and disruption of rings of the vitreous silica so crystallization easily occurs in the regions where the density of contaminations is high enough¹⁷. The volume reduction due to the crystallization of the silica induced strains to the surrounding regions of the formed crystalline. The crystalline phase continued to grow. However, these crystalline layers might contain some voids which thought to occur due to the structure modification of the crystallization. At the vicinity of the center of the crystalline scale, the crystalline phase may reach to the silica/SiC interface but overall, the lateral growth will be much faster than the bulk growth. For the surrounding regions, the crystalline phase oxide layer would remain as the upper layer over the amorphous oxide layer. The strains accumulated due to the crystallization might induce the roughening of the crystalline oxide scale and the surrounded amorphous oxide scale.

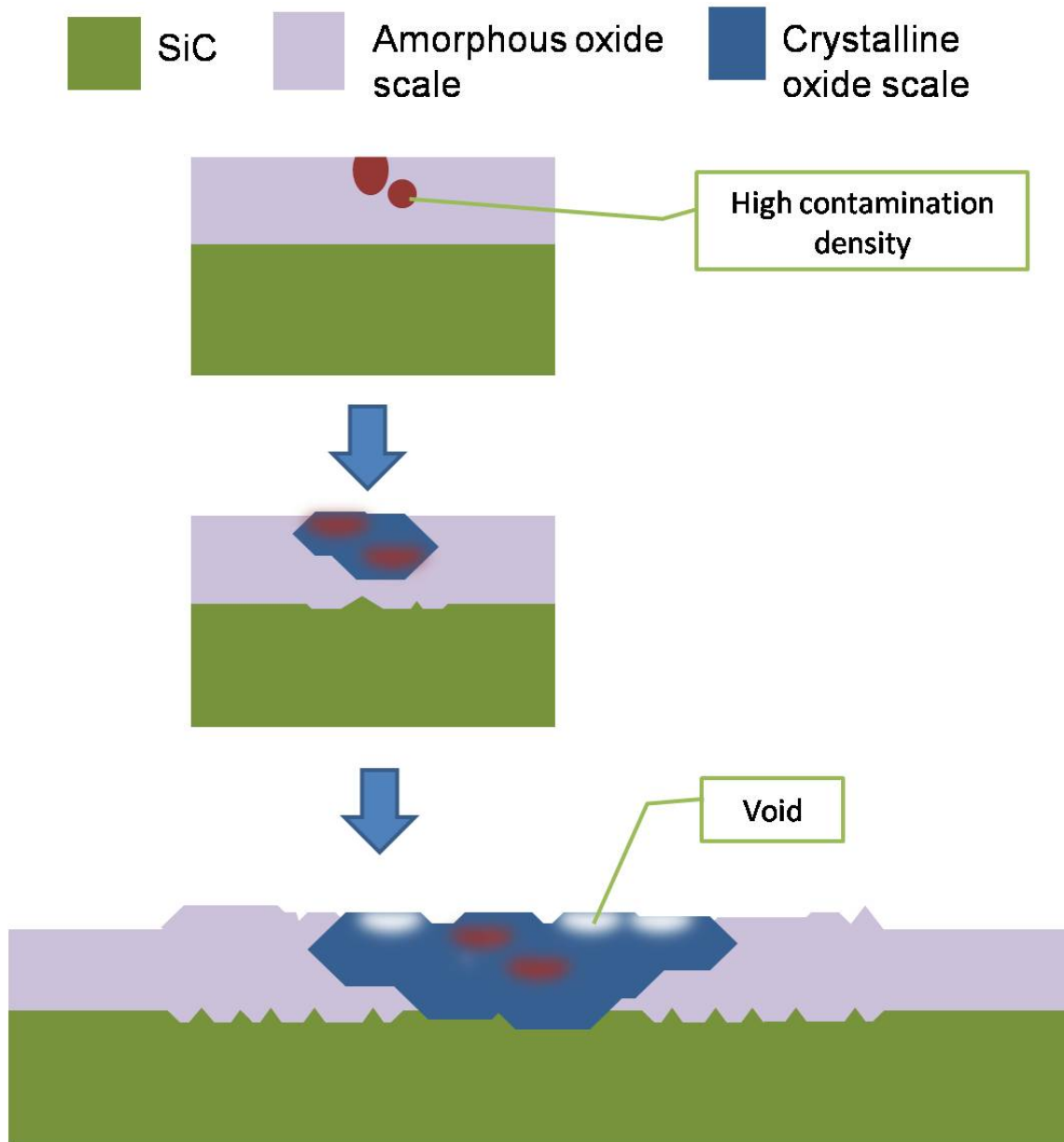


Figure 4-16 : Schematics of crystallization progress.

4.7 Summary

The single crystal silicon carbide was oxidized in pure dry oxygen at 1473 K for 9-25 h. The thermally formed oxide scales were composed mostly of amorphous silica with some crystalline phase oxide scales randomly distributed on the formed oxide scale. The characterization of the microstructures of the thermally formed oxide scales was conducted using optical microscopy together with transmission electron microscopy and X-ray energy dispersive spectroscopy. The crystalline oxide scale was identified by selected area diffraction pattern as alpha cristobalite and beta cristobalite. Traces of calcium were found where the crystalline phase oxide scale existed. The oxidation atmosphere was found to have significantly lower effect on the crystallization than the surface preparation of the sample before oxidation.

References

- ¹ W. L. Vaughn and H.G. Maahs, *J. Am. Ceram. Soc.*, 73 (1990) 1540.
- ² A. H. Heuer, L. U. Ogbuji and T. E. Mitchell, *J. Am. Ceram. Soc.*, 63 (1980) 5.
- ³ T. Narushima, T. Goto and T. Hirai, *J. Am. Ceram. Soc.*, 72 (1989) 1386.
- ⁴ L. U. J. T. Ogbuji and M. Singh, *J. Mater. Res.*, 10 (1995) 3232.
- ⁵ L. U. J. T. Ogbuji, *J. Am. Ceram. Soc.*, 80 (1997) 1544.
- ⁶ D. S. Fox, *J. Am. Ceram. Soc.*, 81 (1998) 945.]
- ⁷ M. J-F. Guinel and M. G. Norton, *J. Mater. Res.*, 21 (2006) 2550.
- ⁸ G.H. Schiroky, *Adv. Ceram. Mater.*, 2 (1987) 137.
- ⁹ D.S. Fox, *J. Am. Ceram. Soc.*, 81 (1998) 945.
- ¹⁰ E. Opila, *J. Am. Ceram. Soc.*, 78 (1995) 1107.
- ¹¹ V. Pressure, A. Loges, Y. Hemberger and K. G. Nickel, *J. Am. Ceram. Soc.*, 92 (2009) 724.
- ¹² W. D. Kingery, *Introduction to Ceramics*, Wiley (1960).
- ¹³ V. Pressure and K. G. Nickel, *Crit. Rev. in Solid State and Mater. Sci.*, 33 (2008) 1.
- ¹⁴ G. H. Frischat, *J. Am. Ceram. Soc.*, 52 (1969) 625.
- ¹⁵ R. Bruckner, *J. Non-Crys. Sol.*, 5 (1970) 123.
- ¹⁶ E. J. Opila, *J. Am. Ceram Soc.*, 82 (1999) 625-36.
- ¹⁷ P.W. McMillan, *J. Non-Crys. Sol.*, 52 (1982) 67

Chapter 5: Microstructures and Defects in Cubic Silicon Carbide

5.1 Introduction

Cubic SiC (3C-SiC) gains attraction in recent years because of its unique cubic structure and its superior electrical properties. 3C-SiC has the highest electron mobility compared to other polytypes of SiC ($1000 \text{ cm}^2/\text{Vs}$ for 3C-SiC and $600 \text{ cm}^2/\text{Vs}$ for 6H-SiC¹). Moreover, 3C-SiC also has lower density of interface states between SiC and SiO₂ than hexagonal SiC². Because of its lowest band gap among SiC polytypes, 3C-SiC is believed to have lowest interface-state traps. These properties make 3C-SiC attractive as a more suitable material for metal-oxide semiconductor field-effect transistors (MOSFETs), compared to the hexagonal 4H-SiC or 6H-SiC. However, during the crystal growth of 3C-SiC, defects such as stacking faults are easily induced in 3C-SiC. The planar defects generated at the 3C-SiC/Si can be categorized in two groups, anti-phase boundaries (APB) and stacking faults. An APB is an interface between two domains of 3C-SiC where Si and C atoms are interchanged³. These defects strongly restrict the development of 3C-SiC as a device material. The fabrication of low defect density substrate is still remained as the main issue in research of 3C-SiC until these days.

A novel method for growing bulk 3C-SiC has been developed by HOYA Inc. The CVD method for growing bulk single crystal cubic SiC was firstly reported in 1980⁴. In this method, the cubic SiC was grown on Si substrate using SiH₄-C₃H₈-H₂ gas system. The resulting SiC was 4 micrometers thick bulk single crystal cubic SiC. Later on, this method was furthermore developed by several research groups, 3C-SiC was grown on silicon substrate by low pressure CVD process⁵. The low pressure CVD allowed low growth temperature compared to the normal CVD, which its temperature is too high for device material (approximate 1623K). The growth temperature of low pressure method ranged from 1023K- 1323K. In this method, acetylene (C₂H₂) and dichlorosilane

(SiH₂Cl₂) were used as the C and the Si sources, respectively. H₂ was used as carrier gas. The 3C-SiC was grown on the silicon substrate. With suitable temperature adjustment, single crystal 3C-SiC could be growth on the (111) face of silicon. In 2002, further technique was developed in order to reduce APB. This technique is to grow 3C-SiC on undulant silicon (001) substrate⁶.

However, the 3C-SiC grown on undulant silicon substrate still has the major problem of extremely high density of defects. These defects could greatly affect performances of devices of 3C-SiC. For 3C-SiC based devices to be actualization, techniques for fabrication of 3C-SiC substrate with lower defects is still needed to be developed.

5.2 Background and Objective

3C-SiC samples produced by CVD method, obtained from HOYA Inc. were characterized using TEM by Kodama et al^{7, 8}. The sample of the CVD method was 3C-SiC grown on undulant and carbonized silicon substrate. The carbonization of silicon substrate leaded to high quality of 3C-SiC grown, compared to the normal undulant silicon substrate. They observed 3 types of stacking faults in the 3C-SiC substrate. The (111) stacking fault with displacement vector \mathbf{R}_F of $1/6[\bar{1}\bar{1}2]$, the $(\bar{1}\bar{1}\bar{1})$ stacking fault with \mathbf{R}_F of $1/6[12\bar{1}]$, and the $(\bar{1}\bar{1}\bar{1})$ stacking fault with \mathbf{R}_F of $1/6[\bar{2}\bar{1}1]$. The (111) and $(\bar{1}\bar{1}\bar{1})$ stacking faults were observed to be decreasing along the growth direction. The origin of dislocations was believed to be from the difference in lattice parameter between silicon and SiC which was about 20% of difference.

In 2006, Yagi et al. reported a new novel technique for growing bulk 3C-SiC with lower defects comparing to the previous CVD method⁹. This technique is called Switch-Back Epitaxy (SBE). It was reported in this study that SBE method reduced defects to one-seventh compared to the CVD method grown on undulant silicon. It also reported to have better electrical properties. The objective in this study is to compare and characterize the defects in 3C-SiC fabricated by CVD method and SBE method.

Moreover, in the process of device fabrication, ion implantation is one of the important processes required. For example, in order to obtain a p-type semiconductor, aluminum is implanted to the SiC. Accordingly, in order to understand more on the effect of device fabrication to the microstructures of the SiC, ion implantation was chosen as an example of the device fabrication process to study the effect on the microstructure. The microstructure characterization of implanted 3C-SiC was conducted on Al ion implanted 3C-SiC using TEM.

5.3 Experimental Procedures

5.3.1 3C-SiC Sample: CVD method and SBE method

Two types of 3C-SiC wafers were provided by HOYA Inc., the CVD 3C-SiC and the SBE 3C-SiC. Fig. 5-1 shows schematics of the method for growing CVD 3C-SiC on undulant silicon substrate. Fig. 5-2 shows schematics of the SBE method. Details for the growth method can be found in reference 4, 5 and 8. The CVD 3C-SiC used in this study is still attached to the silicon substrate.

In the case of the study of the effect of ion implantation, the SBE 3C-SiC was used as substrate. The Al ion implantation was carried out on an area of approximately 0.3 mm × 0.1 mm to obtain p-type 3C-SiC. Implantation was carried out in 6 steps at room temperature with implantation energies of 700, 470, 280, 130, 60, and 25 keV and implanted doses of 4×10^{13} , 2×10^{13} , 2×10^{13} , 1.2×10^{13} , 5×10^{12} and 3×10^{12} atom/cm², respectively. The implanted sample was annealed at 1873 K for 10 minutes.

5.3.2 TEM Specimen Preparation by FIB Microsampling

These specimens were thinned by focused ion beam (FIB), which allows accurate TEM specimen preparation of the interested area. The SBE 3C-SiC samples have a low

defect density, accordingly, the surface of the samples were etched in KOH to visualize the location of defects. In the case of specimens used for high- resolution observation, further argon milling was carried out to remove the FIB damaged layers formed on the thinned specimens. Clear high-resolution images can be observed by using a combination of FIB-Ar ion milling method^{10, 11}. The TEM specimens were examined in a JEOL 200CX and JEM 2010 at an accelerating voltage of 200 kV.

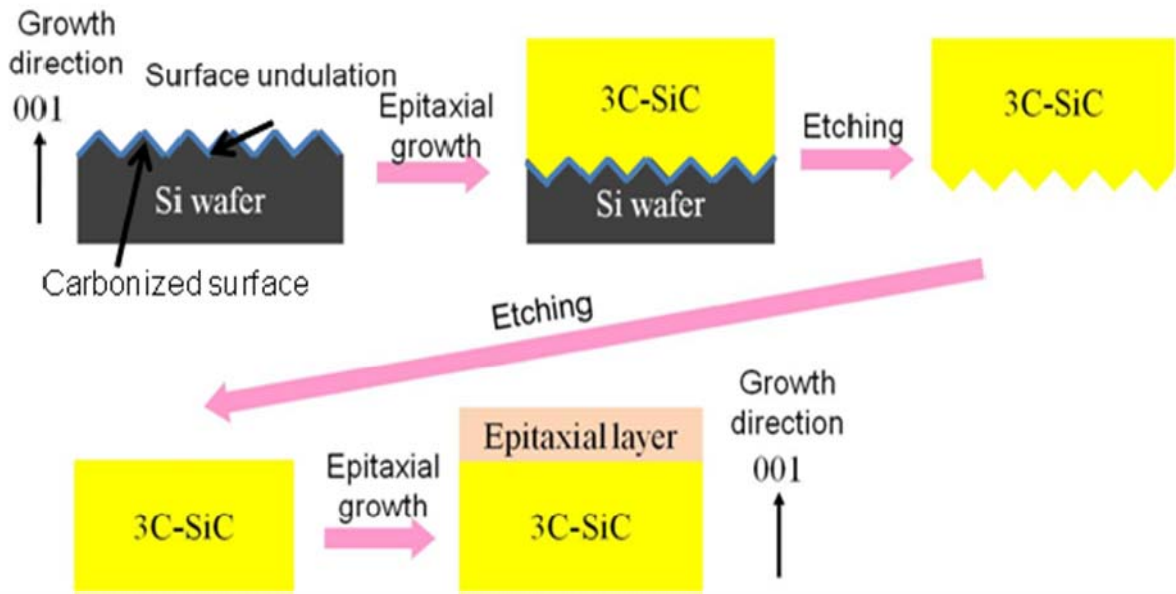


Figure 5-1 : Schematics show process of CVD method.

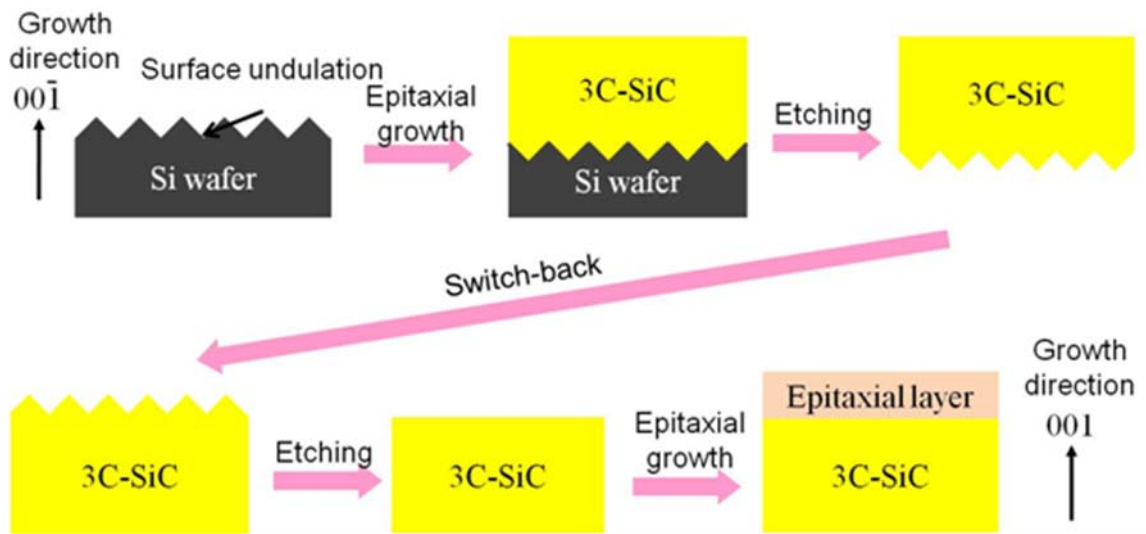


Figure 5-2 : Schematics show process of SBE method.

5.4 Results and Discussion

5.4.1 Defects in CVD 3C-SiC

In zinc blend structures like silicon or cubic SiC, stacking faults can exist in 4 kinds of crystal face, (111), ($\bar{1}\bar{1}\bar{1}$), ($\bar{1}\bar{1}1$) and ($1\bar{1}\bar{1}$). Schematics of these stacking faults are shown in Fig. 5-3.

Figure 5-4 shows cross-sectional TEM image of CVD 3C-SiC near the Si/SiC interface. The observation was made along [110] direction. At the interface, dislocations with very high density are observed. These dislocations are observed to be originated from the interface. Three kinds of stacking faults can be observed in this figure as indicated in the figure. Fig. 5-5 shows counts of stacking fault 1 and 2, which is equivalent to (111) and ($\bar{1}\bar{1}\bar{1}$) stacking fault, versus distance from the Si/SiC interface. It can be seen that, both types of stacking fault are decreasing along the growth direction. The stacking fault 3, the stacking fault in ($\bar{1}\bar{1}1$), was found not to decrease along the growth direction.

Figure 5-6 (a)-(f) show HRTEM images of collision sites of stacking faults taken with $\bar{1}\bar{1}0$ zone axis. From these images, the collision can be categorized into four kinds. Fig. 5-6 (a) shows the site where after collision occurred, both stacking faults disappeared. Fig. 5-6 (b) shows the sites where after collision, the crystal structure of 3C-SiC was collapsed. Fig. 5-6 (c) and (d) show the collision sites where after collided into each other, one of the stacking faults disappeared. And Fig. 5-6 (e) and (f) show that after collision of stacking fault (A) and (B), a new type of stacking fault (C) appeared.

The reduction of (111) and ($\bar{1}\bar{1}\bar{1}$) stacking fault was believed to occur due to the growth on the undulant silicon substrate. The (100) silicon substrate was undulated in $[0\bar{1}1]$ direction. So the SiC is believed not to grow along [100] direction, but rather along [111] or [$\bar{1}\bar{1}\bar{1}$] direction at the initial stage of the growth. At this stage, due to the difference in lattice parameter of silicon and SiC, all 4 types of {111} stacking faults

would form. As the growth continues, (111) and (1 $\bar{1}\bar{1}$) stacking fault would collide into each other and disappear. On the contrary, the ($\bar{1}\bar{1}1$) and ($\bar{1}1\bar{1}$) stacking faults are not parallel to the growth direction, so they will not disappear.

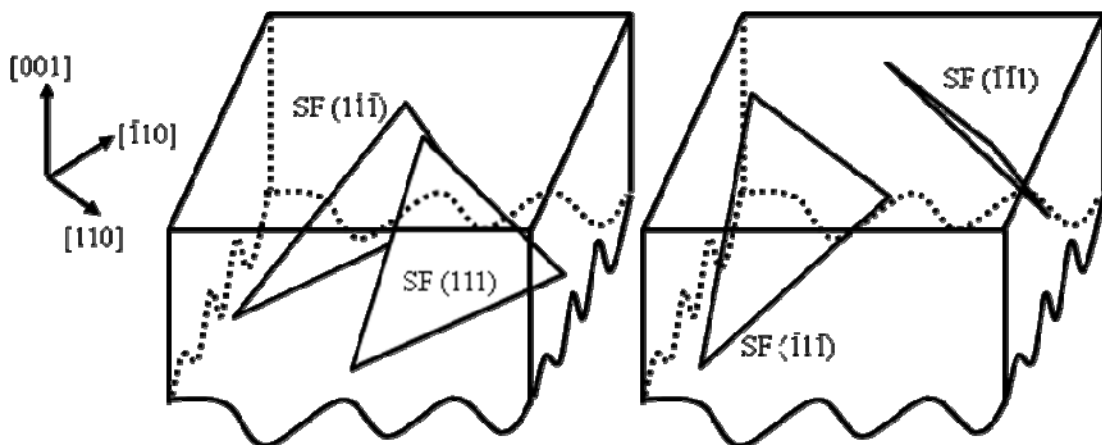


Figure 5-3 : Schematics of defects in cubic SiC.

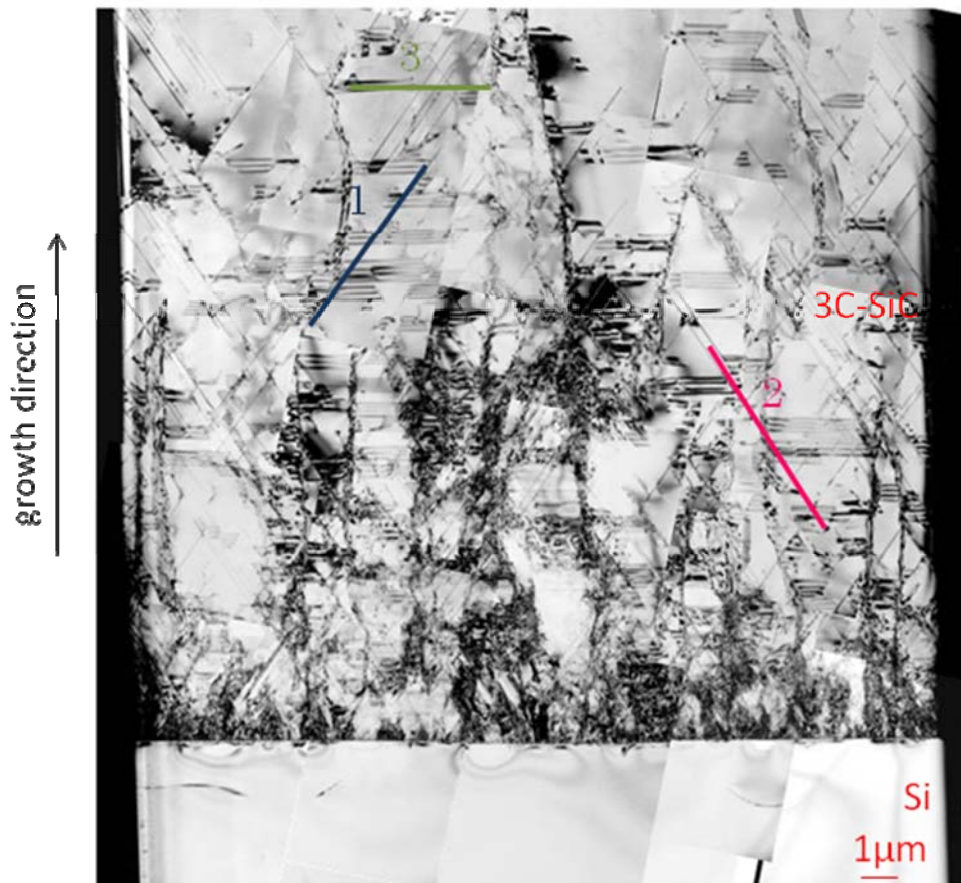


Figure 5-4 : Cross-sectional TEM image of CVD-SiC near Si/SiC interface.

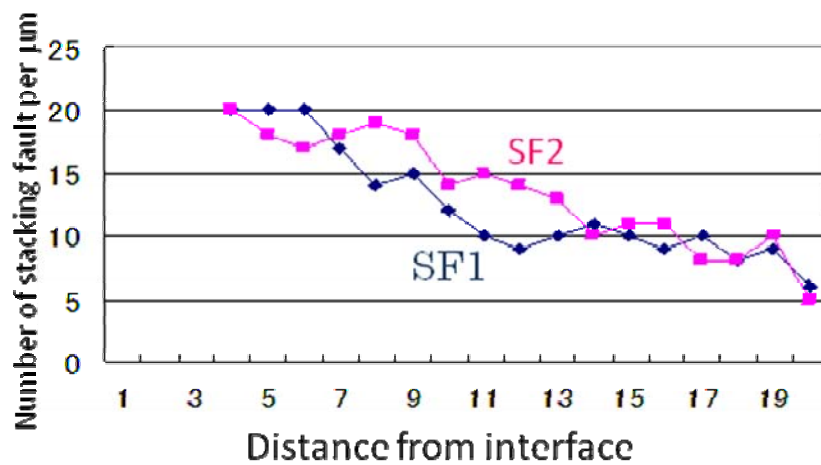


Figure 5-5 : Number of stacking fault vs. distance from the interface.

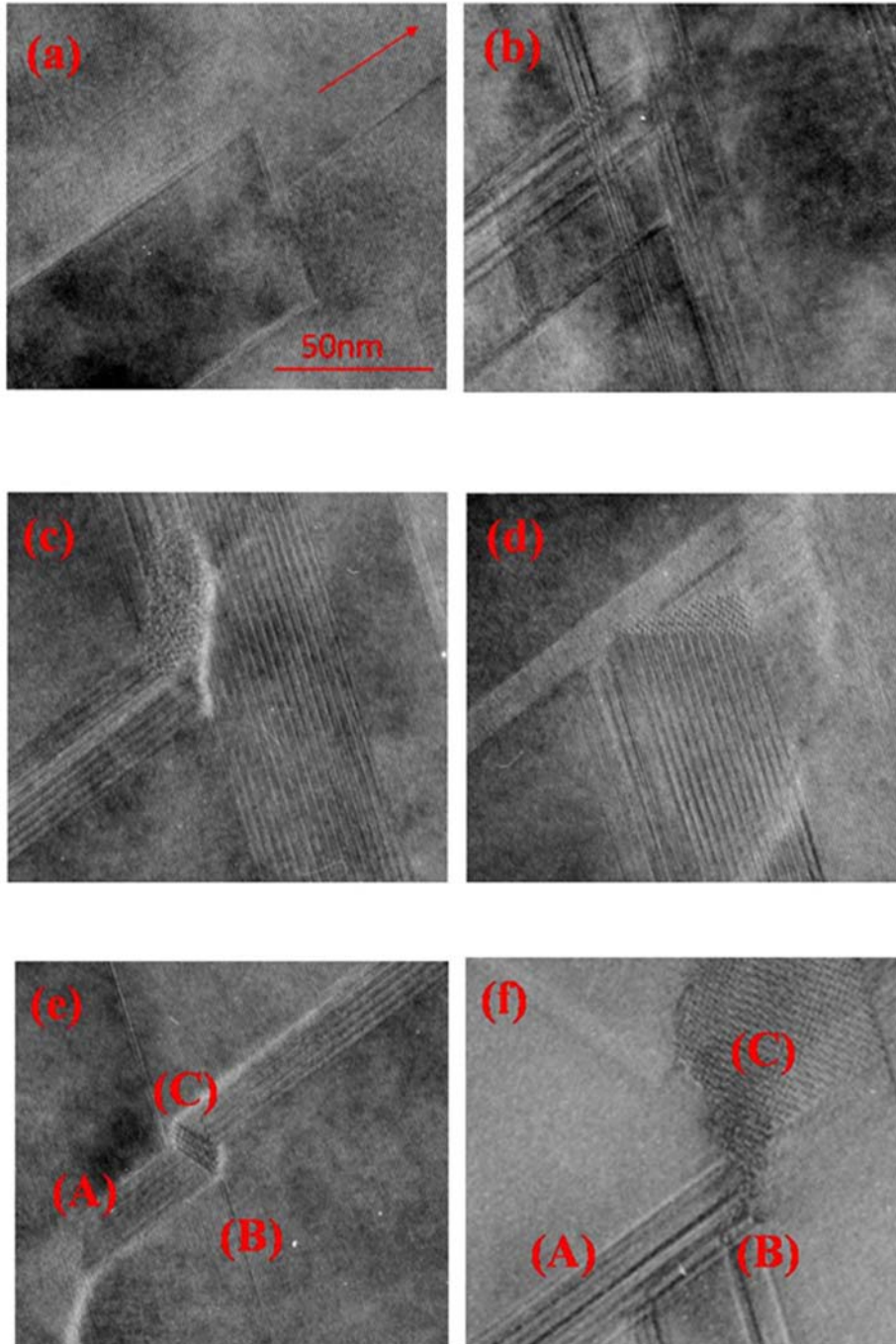


Figure 5-6 : (a)-(f) High resolution TEM images of collision sites of stacking faults.

5.4.2 Defects in SBE 3C-SiC

Figure 5-7 (a) shows X-ray topograph of the CVD 3C-SiC wafer, and (b) shows that of the SBE 3C-SiC wafer. Dark contrast of the topograph shows the regions where defect existed. From Fig. 5-7 (a), it can be seen that the CVD wafer has an extremely high density of defect distributed over the whole sample. While Fig. 5-7(b) shows that the SBE wafer has much lower defect density. It can be seen that, the defects in SBE sample distributed only in some regions of the sample, and some regions have extremely low defect density. Because the low concentration of the defects in SBE 3C-SiC, in order to prepare TEM specimens for the study of defects, samples must be etched in KOH so that the etch pitches would be formed where the defects existed. By this etching, the locations of the defects can be visualized and the TEM specimens can be prepare by using FIB micro-sampling technique.

Figure 5-8 shows (a) SIM image of the surface of SBE 3C-SiC after etching, (b) cross-sectional bright field TEM image and (c) cross-sectional dark field TEM image corresponding to the region indicated by the broken-line square in (a). The TEM observation direction was $[110]$. Figure 5-9 shows (a) SIM image of the surface of 3C-SiC after etching, (b) cross-sectional bright field TEM image and (c) cross-sectional dark field TEM image corresponding to the region indicated by the broken-line square in (a). The TEM observation direction was $[\bar{1}10]$. Rhombic etch pits are observed on the surfaces of the sample. The TEM images were taken under the diffraction condition $\mathbf{g} = \bar{1}\bar{1}\bar{1}$. Stacking faults in the epitaxial layer were observed. From these two perpendicular directions of observation, the relationship between the figure of the etch pitch and the alignment of the stacking fault can be shown as Fig. 5-10.

For comparison, two types of SBE 3C-SiC was etched, the 3C-SiC with 14 micrometers of epitaxial layer and 28 micrometers. Figure 5-11 (a) shows SIM image of the surface of SBE 3C-SiC after etching with 14 micrometers epitaxial layer and (b) shows that of 3C-SiC with 28 micrometers of epitaxial layer.

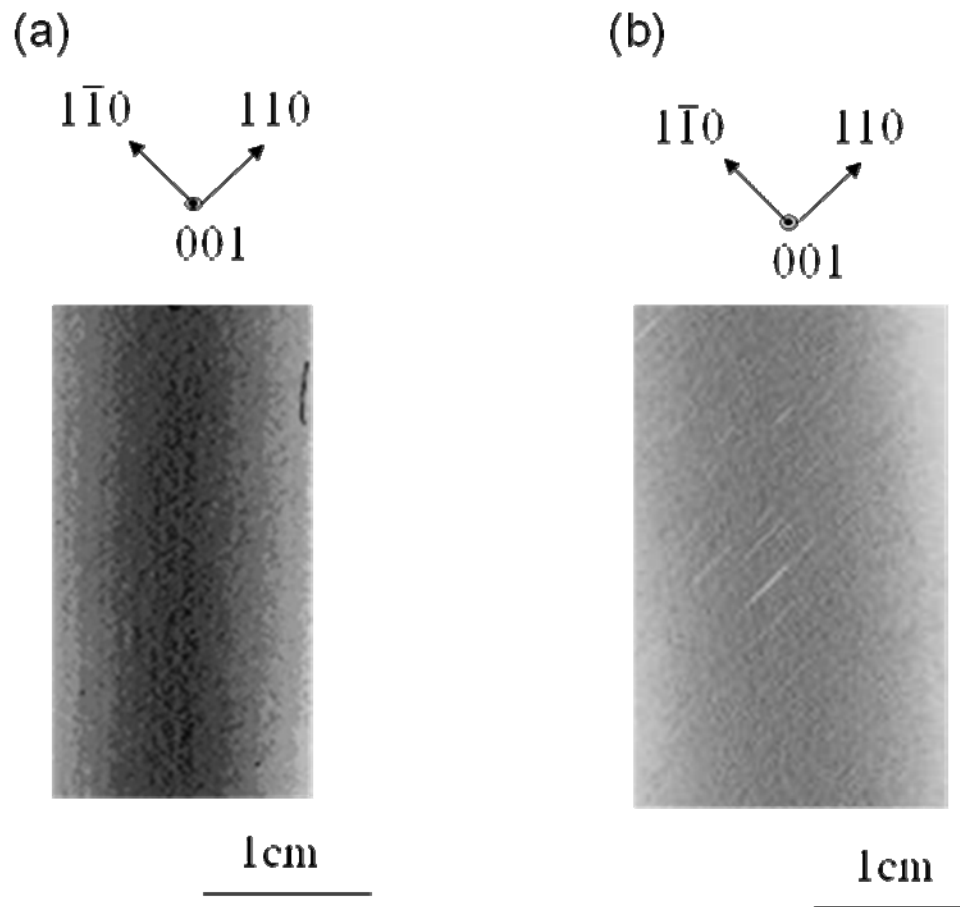


Figure 5-7 : (a) X-ray topograph of the CVD 3C-SiC and (b) shows X-ray topograph of the SBE 3C-SiC.

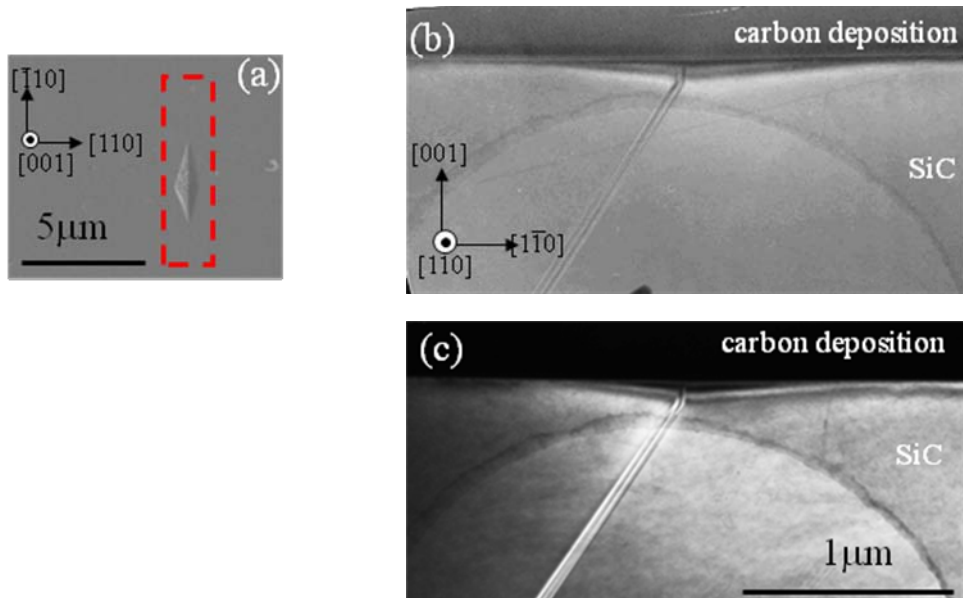


Figure 5-8: (a) SIM image of the surface of 3C-SiC after etching and (b) cross-sectional TEM image corresponding to the region indicated in (a).

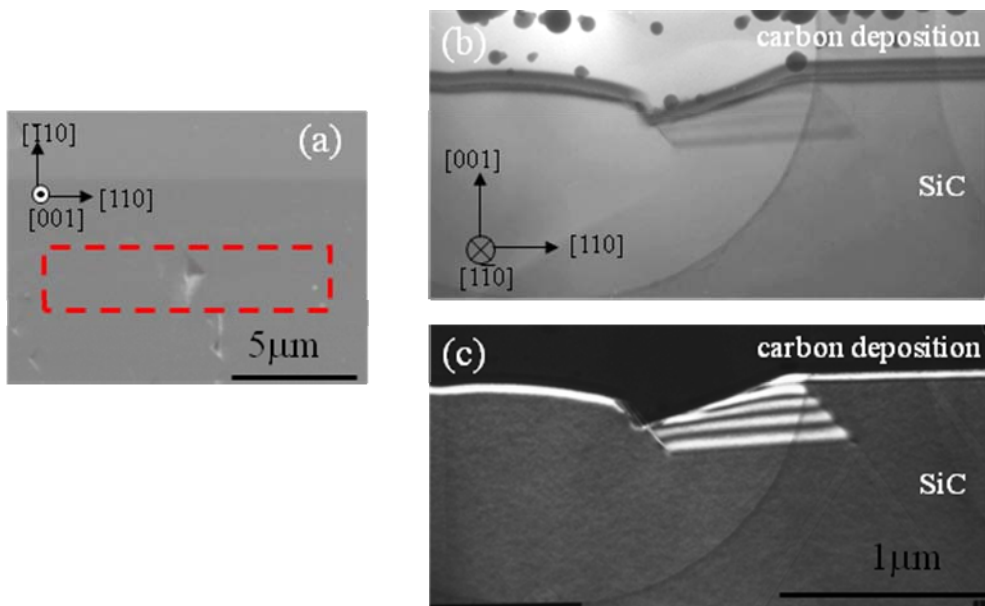


Figure 5-9: (a) SIM image of the surface of 3C-SiC after etching and (b) cross-sectional TEM image corresponding to the region indicated in (a).

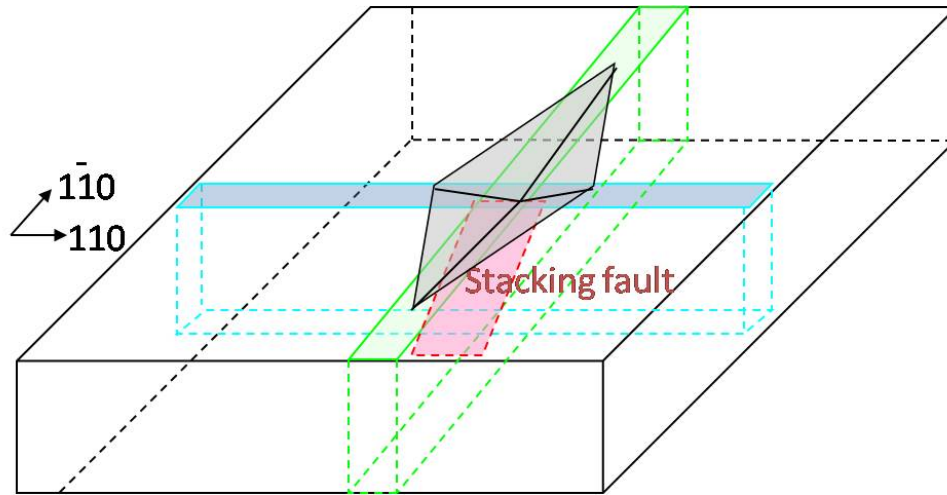


Figure 5-10: Relationship between the figure of the etch pitch and the alignment of the stacking fault.

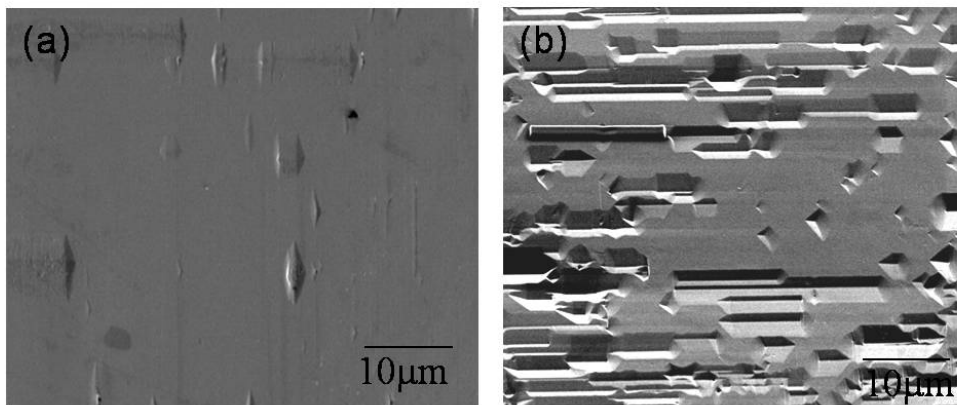


Figure 5-11: (a) SIM image of the surface of SBE with 14 micrometers epitaxial layer and (b) shows that with 28 micrometers of epitaxial layer.

From these images, it can be seen that, as the epitaxial layer thicken, the stacking faults were expanded along [110] direction. The density of stacking faults of the sample with 14 micrometer epitaxial layer was approximate $1.2 \times 10^4/\text{cm}^2$. On the other hand, the density of the sample with 28 micrometer epitaxial layer was approximate $1.7 \times 10^4/\text{cm}^2$. From these results, it can be stated that, not only the width of the stacking fault expanded, but as the epitaxial layer getting thicker, new stacking faults also formed.

A contrast experiment was conducted in order to characterize the displacement vector \mathbf{R} of the stacking fault in SBE 3C-SiC. Fig. 5-12 (a)-(e) show dark-field images of 3C-SiC using the $\mathbf{g} = 002$, $\bar{1}11$, $1\bar{1}1$, $\bar{2}0\bar{2}$, and $\bar{2}20$ respectively. The contrast of the stacking fault is invisible under the $\mathbf{g} = \bar{1}11$ and $\mathbf{g} = \bar{2}0\bar{2}$ conditions. Under these condition, $\mathbf{g} \cdot \mathbf{R} = 0$. Accordingly, the displacement vector of the observed stacking fault was identified to be $\mathbf{R} = 1/6[\bar{1}\bar{2}1]$ and \mathbf{R} lied in the $(\bar{1}\bar{1}\bar{1})$ plane. This result from contrast experiment agrees well with the result of the study on CVD 3C-SiC by Kodama^{6,7}. The stacking faults in both CVD and SBE 3C-SiC can be concluded to be the same type. Accordingly, it is believed that even though the switch back of the 3C-SiC in the middle of growing process reduced the concentration of defects, but it cannot completely eliminate all the defects that previously existed in the CVD 3C-SiC substrate.

5.4.3 Ion Implantation in SBE 3C-SiC

Figure 5-13 (a) shows the cross-sectional TEM image of switch-back epitaxy 3C-SiC after Al ion implantation. A thin band of stacking faults formed in the $\{111\}$ is also observed. In addition, dark contrast spots are observed. These spots are believed to be attributed to the strain field produced by defects induced in the 3C-SiC epitaxial layer by ion implantation. The defects are distributed up to a depth of approximately 500 nm from the surface of the specimen. The area with high density of defects is indicated by a broken-line square in Fig. 5-13 (a). Fig. 5-13 (b) shows the high resolution image of the strain field along the [110] zone axis of 3C-SiC. Displacements of the 3C-SiC lattice along $\langle 111 \rangle$ are observed in this region.

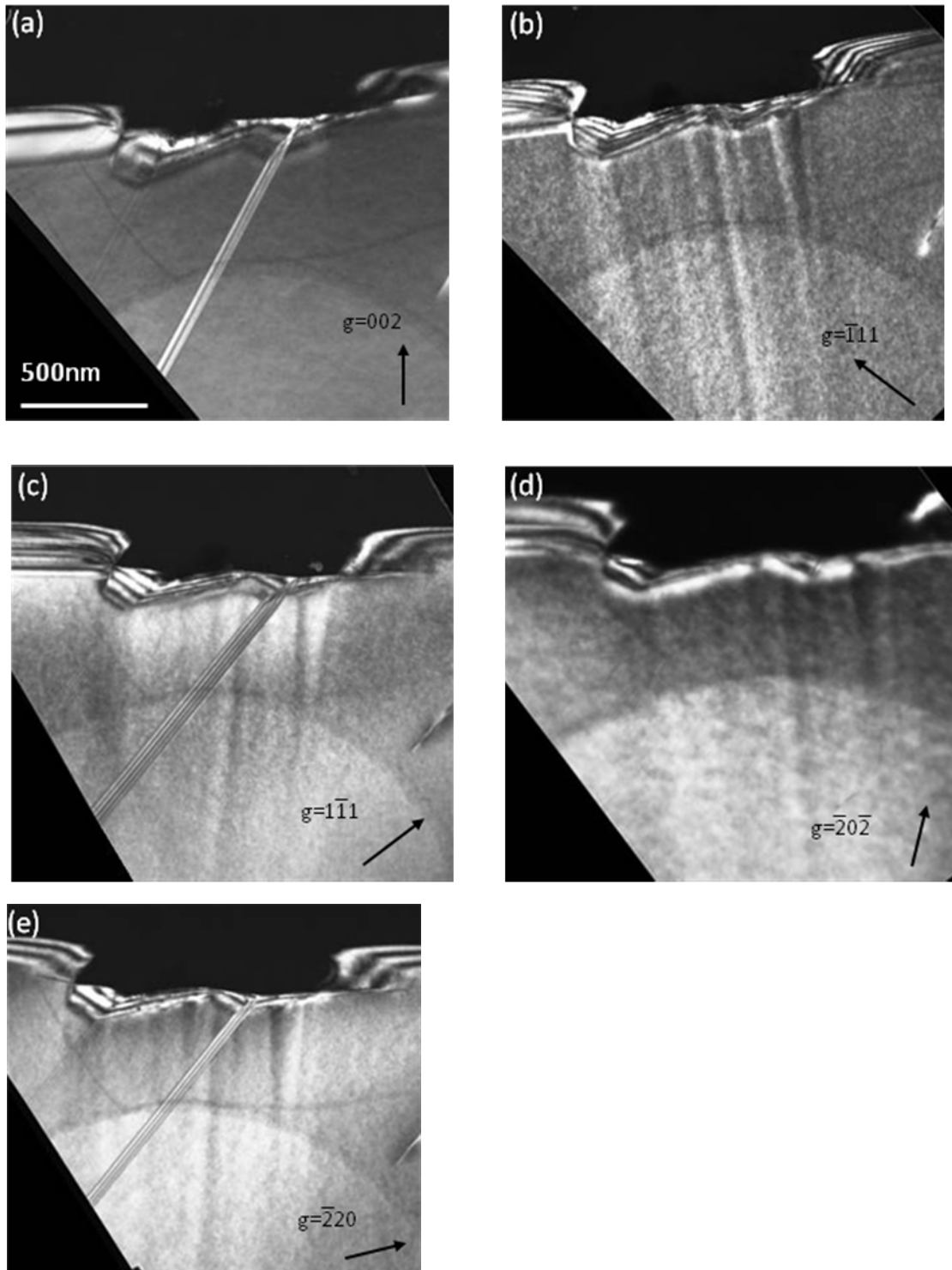


Figure 5-12: (a) – (e) Dark-field images of 3C-SiC taken under the $g=002$, $\bar{1}\bar{1}1$, $1\bar{1}1$, $\bar{2}\bar{0}\bar{2}$ and $\bar{2}\bar{2}0$, respectively.

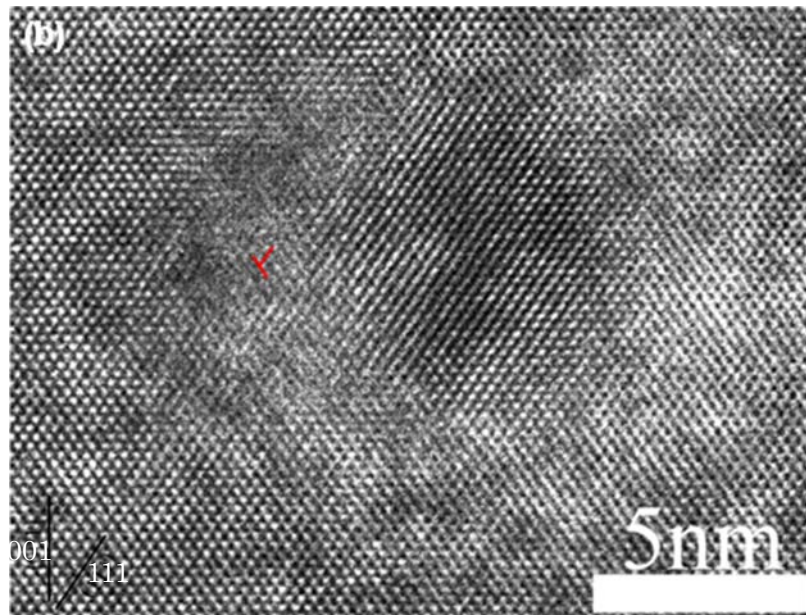
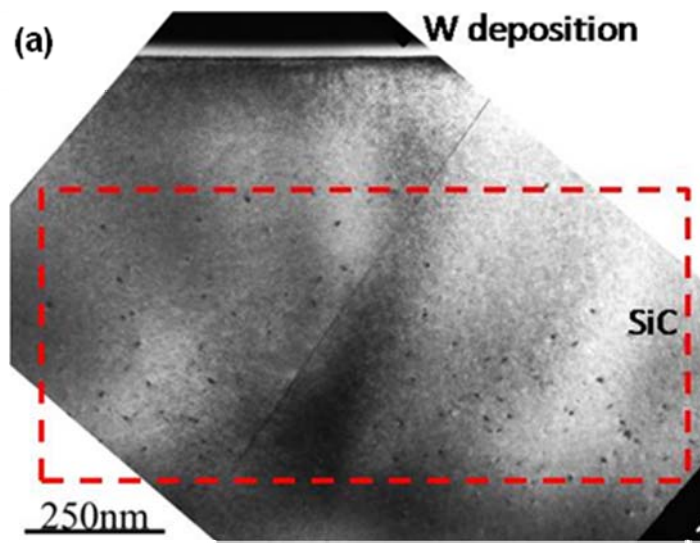


Figure 5-13: (a) Cross-sectional TEM image of 3C-SiC specimen after ion implantation and (b) high resolution TEM image of a dark spot region.

It is known that ion implantation causes amorphization of SiC, and high temperature annealing carried out after implantation recrystallizes the amorphous SiC^{12, 13}. However, in the present study, no amorphous phase or other polymorph of SiC was revealed by SADPs after the implantation and annealing processes. The observed defects possibly originated from the residual defects after recrystallization or from the localized concentration of the implanted Al ions.

5.5 Summary

Microstructures of CVD 3C-SiC were investigated by TEM. High density of defects was found near Si/SiC interface. Decrease of defects along the growth direction was observed. Comparison between the CVD 3C-SiC and the SBE 3C-SiC was made. Microstructures of SBE 3C-SiC were also investigated by TEM. Stacking faults aligned along the {111} were observed in SBE 3C-SiC. The displacement vector of the stacking faults was identified as $R = 1/6[\bar{1}\bar{2}1]$ by contrast experiment. It was found that while the SBE SiC have lower concentration of the defects, but the type of the defect is the same as the CVD SiC. Ion implantation was found to induce additional defects in 3C-SiC. The defects caused by ion implantation were distributed up to a depth of approximately 500 nm from the surface.

Reference

- ¹ G.L. Harris, Properties of Silicon Carbide, Institution of Electrical Engineers (1995).
- ² F. Ciobanu, G. Pensl, H. Nagasawa, A. Schoner, S. Dimitrijević, K-Y. Cheong, V.V. Afanas'ev and G. Wagner, Mater. Sci. Forum 433-436 (2003), 551-554.
- ³ W. R. L. Lambrecht and B. Segall, Phys. Rev. B, 41 (1990) 2948-2958.
- ⁴ S. Nichino, Y. Hazuki, H. Matsunami and T. Tanaka, J. Electrochem. Soc., 127 (1980) 2674.
- ⁵ H. Nagasawa and Y. Yamaguchi, Thin Solid Films, 225 (1993) 230-234.
- ⁶ H. Nagasawa, K. Yagi and T. Kawahara, J. Cryst. Growth, 237-239 (2002), 1244-1249.
- ⁷ Y. Kodama, Master Thesis, (2005).
- ⁸ Y. Miyasaki, Bachelor Thesis, (2005).
- ⁹ K. Yagi, T. Kawahara, N. Hatta and H. Nagasawa, Mater. Sci. Forum 527-539 (2006), 291.
- ¹⁰ H. Sasaki, T. Matsuda, T. Kato, T. Muroga, Y. Iijima, T. Saitoh, F. Iwase, Y. Yamada, T. Izumi, Y. Shiohara and T. Hirayama, J. Electron Microsc. 53 (2004), 497-500.
- ¹¹ T. Matsuda, Mater. Japan, 42 (2003), 916.
- ¹² S. Seshadri, G. W. Eldridge, and A. K. Agarwal, Appl. Phys. Lett., 72 (1998), 16
- ¹³ E. Valcheva, T. Paskovaa, I. G. Ivanov, R. Yakimova, Q. Wahab, S. Savage, N. Nordell, and C. I. Harris J. Vac. Sci. Technol. B 17(3) (1999), 1040-1044.

Chapter 6: Summary

Silicon carbide (SiC) has many excellent properties which make it adequate for using as structural material as well as functional material such as semiconductor device material. From various applications of SiC, there are many aspects of SiC that needed to be considered. In this study, oxidation reactions and defects in SiC bulk, two important topics on electrical device fabrication of SiC were studied using electron microscopy. For the study of oxidation of SiC, hexagonal SiC was chosen as experimental sample because of its high crystal quality compared to other polytypic of SiC. And for the study of defects, at present, the bulk growth methods and conditions of the cubic SiC are still under development and not optimized, accordingly the cubic SiC was chosen as the experimental sample.

At high temperature, in sufficient oxygen partial pressure environment, protective silica oxide scales are known to be formed on SiC. These oxide scales can be used as protective film in various processes. However, many aspects in oxidation of SiC still remain unclear, such as oxidation mechanisms, the microstructures of the oxide scales, or interfaces between oxide scales and SiC. Despite the numerous studies conducted on oxidation kinetics, the oxidation mechanisms still cannot be concluded. One of the main reasons for the indetermination was the wide variation of the data, the oxidation rates and the oxidation activation energies, reported. Possible origins for differences in oxidation rates reported, which then lead to different activation energies calculated, were the differences in samples used, experimental condition, experimental procedures conducted, or methods for oxidation rate evaluation.

Oxidation kinetics of SiC (Chapter 3)

In previous studies on oxidation kinetics of SiC by other investigators, the most frequently used methods for oxide scale thickness measurement were gravimetry or ellipsometry. These methods measured the thickness of the formed oxide scales from

unspecified and relatively wide region of the samples which may lead to errors in thickness measurements. The random distribution of these crystalline oxide scales, which is found in samples in this study regardless of oxidation time and temperature, will lead to an inaccuracy in thickness measurement. Accordingly, it is crucial to specify the regions in which the thickness of the oxide scales will be measured in order to get accurate thickness measurements of the formed oxide scales.

In this study, we measured oxidation rates of the Si-face and the C-face of the single crystal SiC by directly measured the thickness of the oxide scale specifically from the regions composed of only amorphous phase silica using electron microscopy to ensure the accurate thickness measurement. All the experimental settings were designed to minimize affects from other parameters such as contaminations. The oxidation rates of each crystal faces for 1273K – 1473K is reported. The oxidation kinetics was fitted using Deal-Grove model and the oxidation activation energies are estimated. The oxidation activation energy of the Si-face was estimated to be 358 kJ/mol and the activation energy of the C-face is 85 kJ/mol. The calculated oxidation activation energies are compared with other literatures. It was found that the activation energy of the Si-face agreed quite well with other literatures. However, the activation energy of the C-face is significantly lower than most of the literatures. The difference of the activation energy on the C-face may be due to the elimination of the effect of the crystalline oxide scales of this study.

Microstructure of the oxide scales (Chapter 4)

Many studies had reported the finding of crystalline oxide scale in case of the oxidation at relatively high temperature (above 1473 K) and sufficiently long oxidation time. As the oxidation advanced, fall-offs of these crystals were observed. This will lead to the exposure of new un-oxidized surfaces of SiC. Therefore, in the case where SiC is used in high temperature environment with repeated heating, annealing and cooling processes, the formation of the crystalline oxide scales must seriously be considered.

In this study, we use optical microscopy, scanning electron microscopy, together with

transmission electron microscopy (TEM) and X-ray energy dispersive spectroscopy (XEDS), to characterize the microstructures of the thermally formed crystalline oxide scale on single crystal SiC. The crystalline oxide scales were found to distribute randomly on the surface of the samples. The relationships between the sizes and density of the formed crystalline phase oxide scales and the oxidation time and temperatures are not found in this study. Characterization using selected area diffraction patterns identified some of the formed crystalline oxide scales as alpha or beta phase of cristobalite. XEDS showed existence of calcium contamination in some of the crystalline oxide scales, and it is believed that this contamination related to the nucleation of the crystalline oxide scales. Model for the growth process of the crystalline phase oxide scales is developed base on the cross-sectional TEM observations of crystalline oxide scales from various oxidation time and temperature. In this model, it is believed that the nucleation started in the region with high level of contamination, calcium in the case of this study, existed. And the crystalline grew into the previously formed amorphous oxide scale in round-shaped form with radius growth speed much faster than the bulk growth speed, resulting in disc-shaped crystalline oxide scales formation with residue amorphous oxide scales lay underneath. The roughening of the amorphous oxide scales observed at the vicinity of the crystalline scales may caused by the strains due to the crystallization.

In recent years, cubic SiC (3C-SiC) is getting attention for applications in electrical devices because of its superior electrical properties compared to hexagonal SiC. 3C-SiC is reported to have higher electron drift velocity and also has lower interface state density than hexagonal SiC. However, one of the major issues for 3C-SiC at the present is the growth of the 3C-SiC substrate. Accordingly, in order to fabricate electronic devices using 3C-SiC, it is crucial to understand the defect structures in 3C-SiC in order to reduce the density of defects.

Microstructures of Defects in 3C-SiC (Chapter 5)

In this study, defects in 3C-SiC were studied using TEM. The samples studied were 3C-SiC fabricated by chemical vapor deposition (CVD) method or switch-back epitaxy (SBE) method developed by HOYA Inc. in order to reduce defects in the epitaxial layers of the 3C-SiC. For CVD samples, as the SiC grows, the density of the stacking faults was found to be significantly decreasing. The density of the stacking faults of the SBE samples was found to be lower than that of the CVD samples. Stacking faults found in both CVD and SBE samples were identified using contrast experiments in TEM. Both the stacking faults in CVD and in SBE SiC samples were identified to have the same type of displacement vectors, that is $1/6[\bar{1}21]$ and lied in the $(\bar{1}\bar{1}\bar{1})$ plane. Moreover, in the fabrication of electrical devices, ion implantation is one of the processes necessary. In this study, the microstructure of the 3C-SiC after aluminum ion implantation was studied using TEM together with high-resolution electron microscopy. Small clusters of displacement of atoms in 3C-SiC structure along $\langle 111 \rangle$ was observed. These were believed to be caused by the aluminum implantation even after annealing at high temperature. These defects possibly originated from the residual defects after re-crystallization or from the localized concentration of the implanted Al ions.

In conclusion, the oxidation of hexagonal SiC and the microstructures of defects in cubic SiC were studied using TEM. The application of TEM in oxidation study is believed to improve the accuracy of the results of oxidation kinetics compared to previous studies. Moreover, the application of TEM together with the FIB microsampling method enabled detailed study of the crystalline phase oxide scales formed. And for the defects in cubic SiC, the TEM contrast experiment is an essential method for characterization of defects formed in materials.

Acknowledgements

I wish to express my grateful to many individuals and organizations for their support, advice and encouragement.

First of all, I am deeply grateful to my supervisor, Associate Professor Katsuhiro Sasaki for his guidance, valuable ideas, comments and kindness. I am also thankful to my former supervisor, Professor Kotaro Kuroda, for valued suggestions, precious comments, and discussions. And I also acknowledge Assistant Professor Tomoharu Tokunaga for helpful comments and discussions.

I would also like to thank Professor Michiko Kusonoki, Professor Toru Ujihara and Associate Professor Koichi Akimoto for their helpful suggestions, valuable discussion and reading the manuscript.

I really gratified Dr. Takeharu Kato of Japan Fine Ceramics Center (JFCC), who praiseworthy, kindly and patiently gave me invaluable advices and treasurable helps. I also would like to stress my gratitude to Dr. Tsukasa Hirayama, Dr. Yukichi Sasaki and staffs at JFCC, especially all staffs of Nanostructure Research Laboratory, for their precious suggestions, valued helps and encouragement. I also acknowledge JFCC for taking me as a student apprentice, giving me great supplemental learning opportunities.

And I would like to thank all members at Sasaki Laboratory, all Thai seniors, friends and juniors in Nagoya University and elsewhere for valuable friendship and encouragements. Most importantly, I would like to offer my warmest thank to my family for their love and care.

Lastly, I would like to express my obligation to the government of Thailand for the substantial financial assistance and the opportunity to study in Japan.

List of Publications

Refereed Papers

1. Transmission Electron Microscopy Studies of Oxidation of Single Crystal Silicon Carbide at High Temperature

B. Chayasombat, N. Tarumi, T. Kato, T. Hirayama, K. Sasaki and K. Kuroda
Materials Science Forum Vols. 561-565 (2007) pp 2135-2138.

2. Microstructural Characterization of Epitaxial Cubic Silicon Carbide Using Transmission Electron Microscopy

B. Chayasombat, Y. Kimata, T. Kato, T. Tokunaga, K. Sasaki and K. Kuroda
Materials Science Forum Vols. 645-648 (2010) pp 379-382.

3. Characterization of oxide scales thermally formed on single-crystal silicon carbide

B. Chayasombat; T. Kato; T. Hirayama; T. Tokunaga; K. Sasaki; K. Kuroda
Journal of Electron Microscopy 2010; doi: 10.1093/jmicro/dfq039.

4. A Study on Oxidation Kinetics of Single Crystal Silicon Carbide using Electron Microscopy

B. Chayasombat; T. Kato; T. Hirayama; T. Tokunaga; K. Sasaki; K. Kuroda
(Submitted)

5. Characterization of Microstructures of Thermal Oxide Scales on Silicon Carbide Using Transmission Electron Microscopy

B. Chayasombat; T. Kato; T. Hirayama; T. Tokunaga; K. Sasaki; K. Kuroda
(In preparation)

Proceedings

International Conference

1. Transmission Electron Microscopy Studies of Oxidation of Single Crystal Silicon Carbide at High Temperature

B. Chayasombat, N. Tarumi, T. Kato, T. Hirayama, K. Sasaki and K. Kuroda

The Sixth Pacific Rim International Conference on Advanced Materials and Processing (PRICM6), 2007.

2. Microstructural Characterization of Thermal Oxide Scales Formed on Hexagonal Silicon Carbide

B. Chayasombat, T. Kato, Y. Sasaki, T. Hirayama, K. Sasaki and K. Kuroda
AMTC Letters, Vol.1 (2008) pp 40-41.

3. Microstructure of Oxide Scales Thermally Formed on Single Crystal Silicon Carbide

B. Chayasombat, T. Kato, Y. Sasaki, T. Hirayama, K. Sasaki and K. Kuroda
The 9th Asia-Pacific Microscopy Conference (APMC9), 2008.

4. Characterization of Microstructures of Oxide Scales Thermally Formed on Single Crystal Silicon Carbide

B. Chayasombat, T. Kato, T. Hirayama, T. Tokunaga, K. Sasaki, K. Kuroda
The 12th Frontiers of Electron Microscopy in Materials Science, 2009.

5. Microstructural Characterization of Epitaxial Cubic Silicon Carbide Using Transmission Electron Microscopy

B. Chayasombat, Y. Kimata, T. Kato, T. Tokunaga, K. Sasaki, K. Kuroda
The 13th International Conference on Silicon Carbide and Related Materials, 2009.

6. Microstructural Characterization of Oxide Scales Thermally Formed on Single Crystal Silicon Carbide

B. Chayasombat, T. Kato, T. Hirayama, T. Tokunaga, K. Sasaki, K. Kuroda
AMTC Letters Vol.2 (2010) pp 236-237.

7. Microstructures of Thermal Oxide Scales on Silicon Carbide

B. Chayasombat, T. Kato, T. Hirayama, T. Tokunaga, K. Sasaki, and K. Kuroda
The 17th International Microscopy Congress (IMC17), 2010.

National Conference

1. 6H-SiCにおける高温酸化膜の透過型電子顕微鏡による観察

B. Chayasombat, T. Kato, K. Sasaki, and K. Kuroda
The 2007 Spring Meeting of The Japan Institute of Metals.

2. 透過型電子顕微鏡による 6H-SiC の高温酸化膜の微細構造解析
B. Chayasombat, T. Kato, T. Hirayama, K. Sasaki, and K. Kuroda
The 2007 Autumn Meeting of the Japan Institute of Metals.
3. 単結晶 6H-SiC の高温酸化膜の微細構造解析
B. Chayasombat, T. Kato, Y. Sasaki, T. Hirayama, K. Sasaki and K. Kuroda
The 64th Annual Meeting of the Japanese Society of Microscopy, 2008.
4. 単結晶 6H-SiC の高温で形成された酸化膜の結晶相の微細構造解析*
B. Chayasombat, T. Kato, Y. Sasaki, T. Hirayama, T. Tokunaga, K. Sasaki and K. Kuroda
The 2008 Autumn Meeting of the Japan Institute of Metals.
5. 透過型電子顕微鏡による 3C-SiC の欠陥構造の微細構造解析
B. Chayasombat, Y. Kimata, T. Kato, T. Tokunaga, K. Sasaki, K. Kuroda
The 65th Annual Meeting of the Japanese Society of Microscopy, 2009.
6. Thermal oxidation of hexagonal single crystal silicon carbide
B. Chayasombat, T. Kato, T. Hirayama, T. Tokunaga, K. Sasaki, K. Kuroda
The 66th Annual Meeting of the Japanese Society of Microscopy, 2010.